Dissertation

submitted to the

Combined Faculties for the Natural Sciences and for Mathematics

of the Ruperto-Carola University of Heidelberg, Germany

for the degree of

Doctor of Natural Sciences

Christian A. Dávid, M. Sc.

born in Essen

Oral examination: 17th December 2019

Motion Compensation for Free-Breathing Abdominal Diffusion-Weighted Imaging (MoCo DWI)

Christian A. Dávid

Referees: Prof. Dr. rer. nat. Peter Bachert
Prof. Dr. rer. biol. hum. Marc Kachelrieß

Christian A. Dávid, M. Sc.
Heidelberg

This study was performend at the German Cancer Research Center (DKFZ), Heidelberg and Siemens Healthineers, Erlangen.

Concordia cum veritate

Die diffusions-gewichtete Bildgebung (DWI) ist eine wichtige Methode in der medizinischen Diagnostik. In Thorax und Abdomen ist sie jedoch anfällig für Bewegungsartefakte, die durch Atembewegung verursacht werden. Um dies zu lösen, wurde eine neue Technik zur Bewegungskompensation (MoCo) entwickelt und getestet: MoCo DWI. Die Besonderheit an MoCo DWI ist, dass es sich um die erste voll-deformierende Bewegungskompensation bei DWI handelt.

Dies wird trotz des hohen Rauschens bei der DWI möglich, indem zwei Messungen verwendet werden: (1) eine Gradientenecho-Sequenz (GRE) mit optimaler Konfiguration für die Bewegungsschätzung und (2) eine DWI in klinisch relevanter Konfiguration. Die Messungen werden in 10 Bewegungsphasen eingeteilt. Jede der DWI Bewegungsphasen wird dann mittels der Bewegungsschätzung auf eine Zielphase transformiert.

Die Implementierung wurde an elf Probanden getestet. Die Ergebnisse zeigen, dass MoCo DWI Bewegungsunschärfe in Bildern von b-Werten reduzieren kann, insbesondere in der Leber. Bedeutendere Verbesserungen wurden in ADC-Karten erreicht. Hier war es möglich Artefakte zu reduzieren oder zu entfernen. Dies wurde durch homogenere ADC-Werte in der Leber bestätigt.

Diese Ergebnisse lassen weniger DWI Messungen mit eingeschränktem diagnostischen Wert erwarten — und das bei gleichem oder erhöhtem Patientenkomfort.

Diffusion-weighted imaging (DWI) is a common technique in medical diagnostics. One challenge of thoracic and abdominal DWI is respiratory motion which can result in motion artifacts. To eliminate these artifacts, a new kind of retrospective, respiratory motion compensation for DWI was developed and tested. This new technique — MoCo DWI — is the first in DWI which provides fully-deformable motion compensation.

To enable this, despite the low image quality of DWI, two free-breathing sequences were used: (1) a gradient echo sequence (GRE) with a configuration for optimal respiratory motion estimation and (2) a DWI in a configuration of clinical interest. The DWI acquisition was gated into 10 motion phases. Each motion phase was then co-aligned with the motion estimation.

The implementation was tested with eleven volunteers. The results showed that MoCo DWI can reduce motion blurring in single b-value images, especially at the liver-lung interface. The improvement of ADC-maps was even more prominent. Individual slices showed motion induced artifacts which could be reduced or even eliminated by MoCo DWI. This was also reflected by expected more homogeneous ADC values in the liver in all data sets.

These results promise to reduce measurements with limited diagnostic value while keeping or increasing patient comfort.

Contents

Acronyms

ADC apparent diffusion coefficient

BMI body mass index

DFT discrete fourier transform

DVF deformation vector field

dw diffusion-weighted

dw EPI diffusion-weighted echo-planar imaging

DWI diffusion-weighted imaging, also: DW-MRI

EPI echo-planar imaging

FFT fast fourier transform

FoV field of view

GRAPPA generalized autocalibrating partially parallel acquisition

GRE gradient echo sequence

HDTV high dimensional total variation

IQR interquartile range

MoCo motion compensation

MoCo DWI motion-compensated diffusion-weighted imaging

MR magnetic resonance

MRI magnetic resonance imaging

PET positron emission tomography

PMU patient monitoring unit

ROI region of interest

SNR signal-to-noise ratio

TE echo time

TR repetition time

T_1 spin-lattice relaxation time

T_2 spin-spin relaxation time

TV total variation

UF undersampling factor

1. Introduction

The foundation for magnetic resonance imaging (MRI) was settled by Bloch (1946) and Purcell, Torrey, and Pound (1946). Shortly later Damadian (1971) and Lauterbur (1973) further developed this fundament to an imaging tool applicable to human subjects. Since then, magnetic resonance imaging became a standard tool in clinical diagnosis with an increasing number of examinations. In the United States over 110 magnetic resonance imaging (MRI) exams per 1000 inhabitants were performed in 2017, in Germany the number of exams exceeds 136 per 1000 inhabitants (2015, source: OECD 2019).

One key benefit of MRI scans is the high soft-tissue contrast which is important for diagnosis in the brain, (abdominal) organs but also injuries and diseases which affect ligaments, the spinal cord or other structures of the skeleton. An additional distinguishing feature of MRI compared to computed tomography (CT) or positron emission tomography (PET) is the absence of ionizing radiation. Instead, the signal is generated by using a strong magnetic field in combination with switching magnetic fields (the gradients) and radio-frequency electromagnetic pulses.

This technique also offers versatile modes of scanning and thus wide range of different, *in vivo* contrasts for medical diagnosis. Among other things it is possible to create contrasts based on the content of oxygen, phosphorus (Korzowski and Bachert 2018) or sodium (Platt et al. 2018), chemical exchange between molecules (Wolff and Balaban 1990) or functional MRI to detect brain activity. Early on the effect of natural diffusion of molecules on MRI was observed (Hahn 1950) and used to gain a new source of image contrast (Carr and Purcell 1954). This technique utilizes the Brownian motion of molecules in tissue by reducing the signal from molecules with high motion. The diffusion in tissue depends on its natural structure. Damages due to diseases or metastases can change this structure and thus lead to a measurable contrast differences. With DWI not only changes in the speed of diffusion can be detected but also the direction of diffusion. Diffusion-weighted tensor imaging can visualize the connections of fibers in the brain. Recent developments even create a contrast depending on the shape of pores (Demberg et al. 2018; Kuder and F. B. Laun 2015).

Common clinical applications of DWI are neurological imaging — especially stroke detection (Hankey 2017) — or oncology imaging. DWI in the abdomen falls into the category of oncology imaging where several fields of application are possible. Sensitivity for detection of lesions in the liver using contrast-enhanced MRI can be improved by DWI, especially if the lesions are small (Koh et al. 2008; Mannelli et al. 2013). Also, a characterization, e.g. solid and cystic lesions, can benefit from DWI. Currently T_1-weighted MRI with gadolinium contrast agent outperforms DWI here. However, administering this contrast agent is not possible for all patients and for this reason DWI is a reasonable alternative in these cases (Chandarana and Taouli 2010; Kanematsu et al. 2013; Mannelli et al. 2013). After radiation therapy in the abdomen DWI can be used as an assessment for treatment response (Chandarana and Taouli 2010). Recent advancements show potential in diagnosis of chronic diffuse liver disease. Abdominal DWI is also used for tumor characterization in the pancreas and kidneys.

A challenge of DWI is its low signal-to-noise ratio (SNR). To compensate for that prolonging the acquisition duration is beneficial. Additionally, it is required to repeat the acquisition with different weighting of the diffusion effect (b-values) to distinguish between signal changes caused by diffusion and other effects. This leads to typical acquisition duration of several minutes. However, this introduces a new challenge; during these long *in vivo* measurements motion can deteriorate the diagnostic use of the resulting images. The main source of motion is respiration of the subjects (Chandarana and Taouli 2010). Also mentioned should be cardiac motion causing arterial pulsations. In the lower abdomen moving of the intestine is another important source of involuntary motion.

Recently it was shown that respiratory motion is an important contributor for poor reproducibility in a multi-center DWI study (Pathak et al. 2017). For estimation of apparent diffusion coefficients (ADCs) it is even identified as the main source of error (Ragheb et al. 2015). To overcome artifacts caused by respiratory motion, several methods are in clinical use and further ones were suggested. In clinical use are breath-hold scans and prospective triggering. Under development are retrospective correction methods in which the acquisition is done in free-breathing. The motion is then handled during the reconstruction of the images; here especially motion compensation (MoCo) techniques are promising.

From a technical point-of-view breath-hold is potentially the easiest method to accomplish. However, it comes with the drawback that the measurement duration is severely limited by the patients' capability to hold his/her breath. Typically, breath-hold acquisitions are in the range of 20 s to 30 s (Schmid-Tannwald et al. 2013). For this reason the field-of-view, resolution, number of b-values as well as number of averages to reduce SNR are limited in favor of a short measurement time. Potentially multiple breath-holds are possible but this approach is unfavorable for routine use. Also asking patients to hold their breath is not always feasible, especially in pediatric MRI (Gottumukkala et al. 2019; Jaimes and Gee 2016) or patients with asthma or dementia.

Alternatively prospective triggering can be used (Kandpal et al. 2009; Nguyen et al. 2014; Shenoy-Bhangle et al. 2017; Taouli et al. 2009). Here the DWI measurement is only done if a specific phase of the respiratory cycle is reached, typically the end-exhale phase. In the other motion phases the DWI measurement is paused, eventually the time is used to detect the next desired motion phase. Kandpal et al. (2009) reported that triggered DWI has increased SNR and contrast-to-noise ratio (CNR) compared to breath-hold sequences. However, prospective triggering prolongs the measurement time by a factor of 2.5 to 3 (Taouli et al. 2009) or even more (Shenoy-Bhangle et al. 2017). The variation depends on the breathing pattern of the subjects. This prevents well predictable duration of measurements which are favored for instance in level-wise scanning for whole-body measurements.

New development uses free-breathing DWI measurements and handle the motion after the measurement. One option are retrospectively gated DWI measurements (Y. Liu et al. 2017; van de Lindt et al. 2018). They use that each b-value (if used also direction of the gradient field) is acquired independent of each other. Then a respiratory surrogate signal is used to assign each acquired subset (single slices or 3D volumes) into a bin. The advantage over prospective triggering is the use of the full measurement time which allows for 4D DWI. While this targets artifacts caused by respiratory motion the SNR is reduced compared to images without motion handling.

For this reason more advanced techniques use motion compensation to utilize the whole measured information (Guyader et al. 2015; Mazaheri et al. 2012; Ragheb et al. 2015). They are typically based on retrospective gating as described above to generate 4D DWI. Then a registration method is used to estimate the motion between the motion phases. The estimation is then used to co-align the gated phases of the 4D DWI. Afterwards the co-aligned phases are recombined to a single volume. Due to this procedure the full measurement is used in the final image. For this reason the SNR is not reduced which outperforms retrospective gating.

All these MoCo methods depend on image registration which itself requires high quality input images for a good motion estimation. However, this is not the case for DWI, especially for high b-values. In consequence Mazaheri et al. (2012) only used rigid registration between slices in axial orientation. Guyader et al. (2015) and Ragheb et al. (2015) used b-spline image registration with only three control points in the main motion direction (superior-inferior).

A similar issue exists in positron emission tomography (PET) imaging. Here the resolution and SNR of single time frames, which could resolve respiratory motion, is relatively low. Therefore, multiple studies successfully used combined PET/MR imaging to estimate the motion on MR sequences which are optimized for this purpose and then apply this on PET imaging (Grimm et al. 2015; Rank, Heußer, Wetscherek, et al. 2016; Würslin et al. 2013). The motion is estimated solely on a T_1-weighted 3D volume with high temporal resolution and

CNR (K. T. Block et al. 2014). In the study presented here, this idea is transferred to DWI for the first time. Thus, the motion estimation is not impacted by the suboptimal image-contrast of DWI.

The combination with PET/MR is of even higher interest because DWI measurements are recommended for PET/MR studies (Ishii et al. 2016). Thus, the motion estimation is part of the study anyway and hence no additional measurement time is added.

In the presented work a prototype for this kind of motion compensation, MoCo DWI, is developed, tested with volunteers and evaluated. In the following, a brief introduction to the extensive physical background which makes this study possible is given (Chapter 2). MoCo DWI is described in detail in Chapter 3. Thus, this chapter includes all information which is required to reproduce this study. Additionally, related work is presented there. Chapter 4 shows the results achieved using these methods. Especially the images and ADC-maps, but also the quantitative measurements. The results are discussed in Chapter 5. Also, several properties of MoCo DWI are critically examined and MoCo DWI is compared with alternative methods. The study concludes with a summary (Chapter 6). A reader who is interested in the highlights only, may refer to Figure 4.14 first.

2. Theory

2.1. Overview

Many physical theories and effects are utilized in this work or influence it (Figure 2.1). In this chapter this prior knowledge is briefly touched. In favour of the following chapters the descriptions are kept short. For a more in depth discussion further reading is suggested in the corresponding sections.

2.2. Physical Background of Magnetic Resonance Imaging

2.2.1. Nuclear Spin

The Stern-Gerlach Experiment proofed two discrete angular momenta of (uncharged) silver atoms (Gerlach and Stern 1922). This significant observation was the first to show experimentally a quantum mechanical property in an object of full atomic scale. For this achievement Otto Stern and Walter Gerlach were awarded with the Nobel Prize in Physics 1943.

This observation is now described with the nuclear spin I, a quantum mechanical property. In the presence of a magnetic field $\mathbf{B}$ the Zeemann effect appears which causes a split into $2I + 1$ energy levels (Figure 2.2). The different levels are distinguished by the magnetic quantum numbers $m_I = -I, -I + 1, \dots, I$. These energy levels are characteristic for the nucleus and are given by

$$E_{\text{mag}} = -\hbar \gamma m_I B \, . \tag{2.1}$$

Here γ is the gyromagnetic ratio of the nucleus of interest and $\hbar$ the reduced Planck constant.

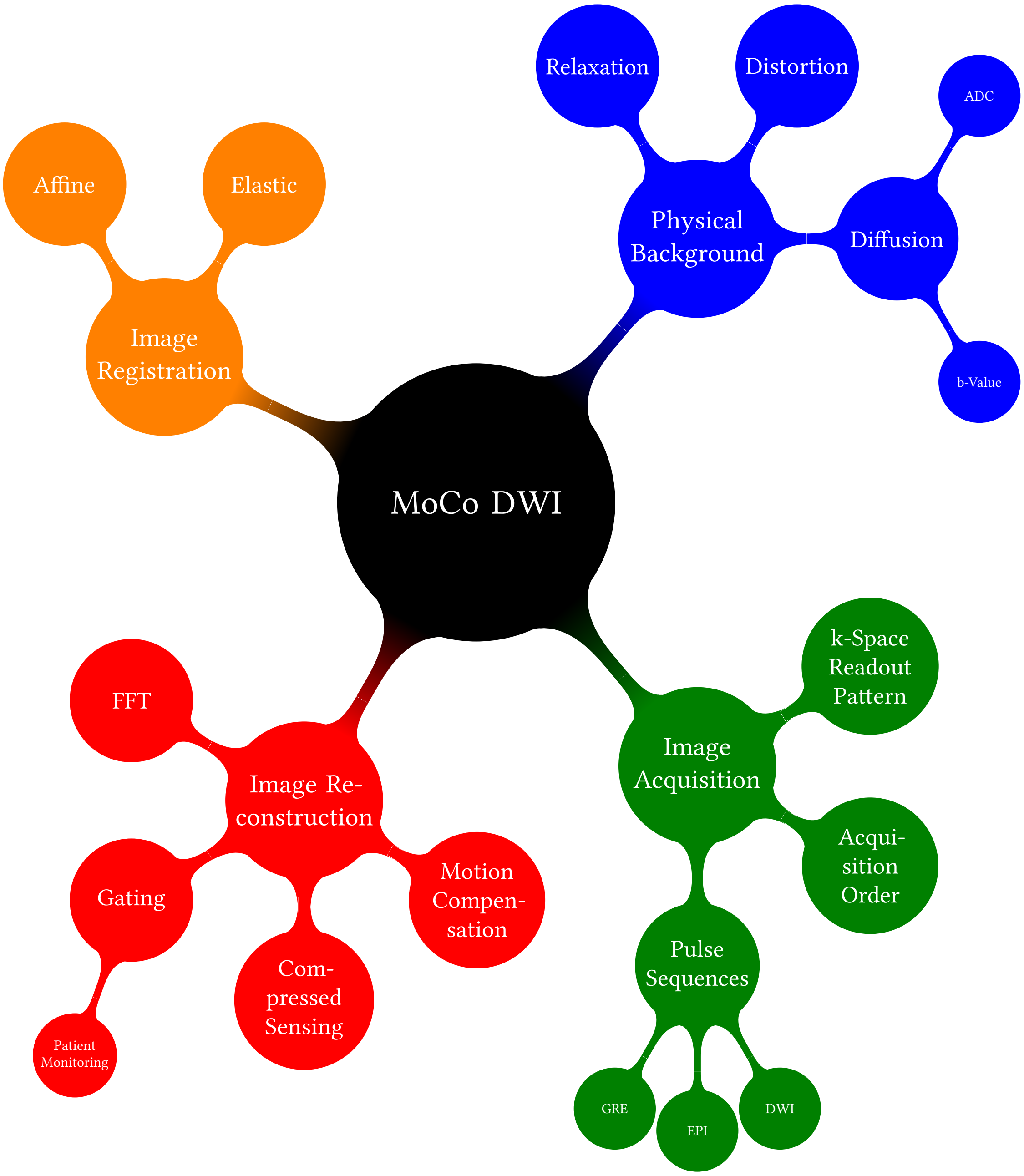

Figure 2.1.: MoCo DWI is based on many physical effects and techniques. This mind map shows important topics.

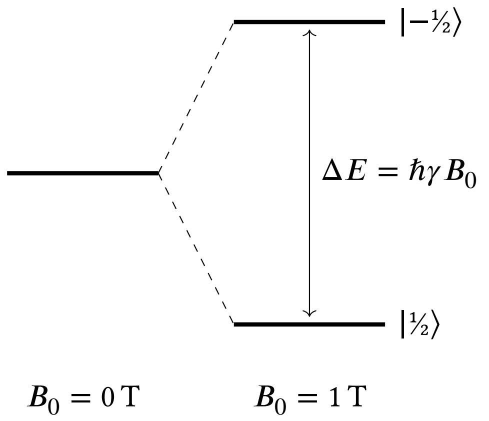

Figure 2.2.: Zeemann energy levels for a one-half spin system, as given for protons – the most important nucleus for MRI. Because $\gamma > 0$ holds for protons, the spin down ($|-\frac{1}{2}\rangle$) is the state of higher energy. The energy difference between both states is $\hbar\gamma B_0$.

Consequently, the energy difference between two neighbouring states is

$$\Delta E = \hbar\gamma B_0 = \hbar\omega_\mathrm{L} \text{ with} \tag{2.2}$$

$$\omega_\mathrm{L} = \gamma B_0 \,. \tag{2.3}$$

The frequency ω_L is named Larmor frequency — an essential physical quantity in MRI.

For medical MRI the protons (^1H, $I = ½$) in the water molecules are of major interest. Their gyromagnetic ratio is $\gamma_{^1H}/2\pi \approx 42.58\,\mathrm{MHz/T}$ (*CODATA* 2018). Current medical scanners are in the range of $B_0 = 1.5\,\mathrm{T}$ to $7\,\mathrm{T}$, so the Larmor frequency is in the range of radio frequency with $\omega_\mathrm{L} = 60\,\mathrm{MHz}$ to $300\,\mathrm{MHz}$.

2.2.2. Macroscopic Description

In clinical resonance imaging spin ensembles of many spins are investigated rather than single spins. For this reason the quantum mechanical description is often not required and a macroscopic description can be used. Here only packets of spin are considered, which can be considered as one dipole per volume element (voxel) of the full imaged volume. Thus, they can be described by their total, macroscopic magnetisation $\mathbf{M}(t)$.

This magnetisation is the sum over the dipole moments of the individual spins, in this classical view (R. W. Brown et al. 2014b)

$$\mathbf{M} = \frac{1}{V} \sum_{i=\text{protons in } V} \boldsymbol{\mu}_i \,. \tag{2.4}$$

The equation for changes of the macroscopic magnetization $\mathbf{M}$ is described by the Bloch equation (R. W. Brown et al. 2014b);

$$\frac{\mathrm{d}\mathbf{M}(t)}{\mathrm{d}t} = \mathbf{M}(t) \times \gamma\mathbf{B} + \frac{1}{T_1}\big(M_0 - M_z(t)\big)\mathbf{e}_z - \frac{1}{T_2}\mathbf{M}_\perp(t)\,. \tag{2.5}$$

If only the static magnetic field of the MR scanner is present $\mathbf{B} = \mathbf{B}_0 = (0, 0, B_0)^\mathrm{T}$ is the static magnetic field (e.g. of the scanner). M_0 denotes the equilibrium magnetization, which is parallel to $\mathbf{B}_0$, and $\mathbf{M}_\perp = (M_\mathrm{x}, M_\mathrm{y}, 0)^\mathrm{T}$ denotes the transveral magnetisation. T_1 is the the spin-lattice relaxation time and T_2 the spin-spin relaxation time. Both are of high importance for MRI because they are tissue dependent and can thus be used for various kinds of contrasts.

The solution of the Bloch equation for the three components is (R. W. Brown et al. 2014b)

$$M_\mathrm{x}(t) = \big(M_\mathrm{x}(0)\cos(\omega_\mathrm{L} t) + M_\mathrm{y}(0)\sin(\omega_\mathrm{L} t)\big)\,\mathrm{e}^{-t/T_2}\,, \tag{2.6}$$

$$M_\mathrm{y}(t) = \big(M_\mathrm{y}(0)\cos(\omega_\mathrm{L} t) + M_\mathrm{x}(0)\sin(\omega_\mathrm{L} t)\big)\,\mathrm{e}^{-t/T_2}\,, \tag{2.7}$$

$$M_\mathrm{z}(t) = M_\mathrm{z}(0)\,\mathrm{e}^{-t/T_1} + M_0(1 - e^{-1/T_1})\,. \tag{2.8}$$

From these equations, several observations can be derived. The previously quantum mechanical introduced Larmor frequency ω_L appears again, this time as the classical rotation frequency of the transversal magnetisation $\mathbf{M}_\perp$. The relaxation time T_1 defines M_z's speed of returning into the steady-state ($t \to \infty$). However, changes of $|\mathbf{M}|$ are not related to T_1. Contrary to this, T_2, is accompanied by a reduction of $|\mathbf{M}|$ by reducing $\mathbf{M}_\perp$ until $\mathbf{M}_\perp(t \to \infty) = 0$ but without changing M_z (R. W. Brown et al. 2014b).

To deflect the magnetization from its steady state, RF pulses with the frequency ω_L are be used. Here the length and amplitude define how much the direction of $\mathbf{M}$ changes, quantified as flipangle (FA or $\alpha = \measuredangle(\mathbf{M}_\mathrm{before}, \mathbf{M}_\mathrm{after})$).

2.3. Magnetic Resonance Imaging Pulse Sequences

For medical diagnosis it is important to measure a image, or preferable a three dimensional image; a volume. To achieve this MRI uses well timed manipulations of the magnetisation with RF excitation and additional, short-lived magnetic fields. For changes of the magnetic field, gradients $\mathbf{G}$ are used. They add a spatial component to the static magnetic field $\mathbf{B}(x, y, z) = B_0\mathbf{e}_z + (0, 0, G_\mathrm{x}x + G_\mathrm{y}y + G_\mathrm{z}z)^\mathrm{T}$. The purpose of these gradients is to change the Larmor frequency $\boldsymbol{\omega}_\mathrm{L} = \gamma\mathbf{B}$ in dependence of location for data acquisition. For this reason, the data is not directly measured in spatial domain but in frequency domain (k-space).

The k-space is the multi-dimensional space which assigns each wave vector **k** the corresponding measured data. The measured k-space coordinate is hereby given by the gradient fields as (cf. R. W. Brown et al. 2014d)

$$\mathbf{k}(t) = \gamma \int_0^t \mathbf{G}(t') \, \mathrm{d}t' \; . \tag{2.9}$$

Since the measured frequencies are generally affected by an phase, the values of the k-space are complex ($\mathbb{C}$). In Section 2.5 multiple ways are described how this information is used to calculate the volume in image space.

A combination of RF pulses, gradients and their timing is refereed to as sequence. As described before, more advanced sequences can visualize or even measure several physical properties by advanced combination of (multiple) RF pulses and gradients (e.g. diffusion, Section 2.4). Two important imaging sequences, the gradient echo sequence (GRE) and echo-planar imaging (EPI), are used and presented in this work. An extension to the EPI sequence for imaging of diffusion, the diffusion-weighted echo-planar imaging (dw EPI), is described in Section 3.1.2.

2.3.1. Gradient Echo Sequence (GRE)

The GRE sequence (also gradient recalled echo sequence) is a flexible magnetic resonance (MR) sequence which is commonly used in medical imaging. It starts with an RF pulse which flips the magnetisation into the transversal plane. Then a gradient is turned on which causes a rapid dephasing and thus a reduction of receivable signal. A second gradient in opposite direction is used to rephase the signal which is then measured (after one echo time TE, Figure 2.3).

This procedure is repeated to acquire enough data to fill the k-space. The time required for one of these repetitions is named TR. TR and TE are important properties of the sequence. In this work they are selected as short as possible for fast acquisition, leading to a T1-weighted signal.

An advantage of the GRE sequence is its increased quality of the magnitude image compared to measurements without the echo. Compared to RF pulse induced echos (cf. Section 2.3.2) it is faster, which justifies reduced rephasing efficiency (Markl and Leupold 2012).

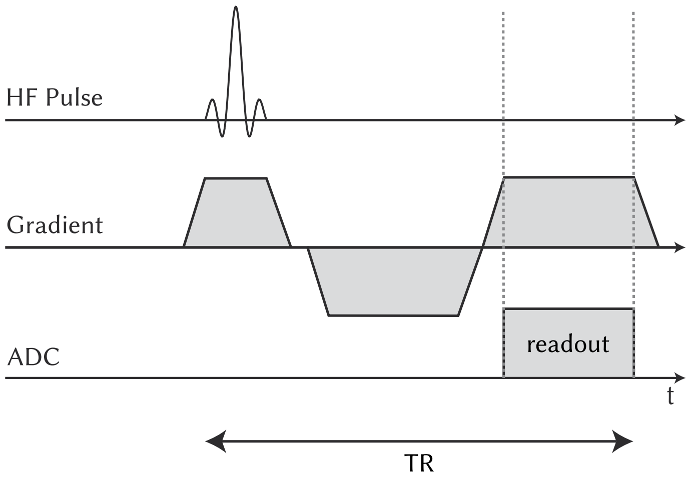

Figure 2.3.: Gradient echo pulse sequence (GRE) diagram. The magnetisation is flipped into the transversal plane with a RF pulse. For slice selection a gradient is used simultaneously. The second gradient is then used to dephase the spins which is reversed by the following gradient of the same shape but inverse direction (cf. Markl and Leupold 2012).

2.3.2. Echo-Planar Imaging Sequence (EPI)

The EPI sequence is a very fast imaging sequence (Weishaupt, Köchli, and Marincek 2014). The acceleration is achieved by reducing the number of required flip-pulses. It uses a single 90° RF pulse to flip the magnetisation into the transversal plane — just like the GRE sequence. However, for rephasing a 180° RF pulse is used. This rephasing is quickly repeated without further 90° RF pulses (Figure 2.4).

In contrast to the gradient-induced decay in the GRE sequence, the decay after the RF pulses is slower (T_2^* decay). However, the RF refocusing is more effective because it also reverses dephasing caused by local field inhomogeneities. Thus, the envelope which defines the signal loss, decays with T_2 only which allows huge numbers of repetitions but with decreasing SNR.

2.3.3. Distortion

The static magnetic field B_0 as well as the field created by the gradient coils (**Gr**), is not homogeneous. In addition to general imperfections, these fields drop (B_0) or deviate from their linear slope (**Gr**) with increasing distance from the scanner's iso-center. Also regions with strong susceptibility variations in the measured subject cause field deviations. These deviations causes non-isometric voxel sizes leading to a distorted image. Especially EPI sequences are prone to this kind of error (Figure 2.5). Due to the long k-space trajectories

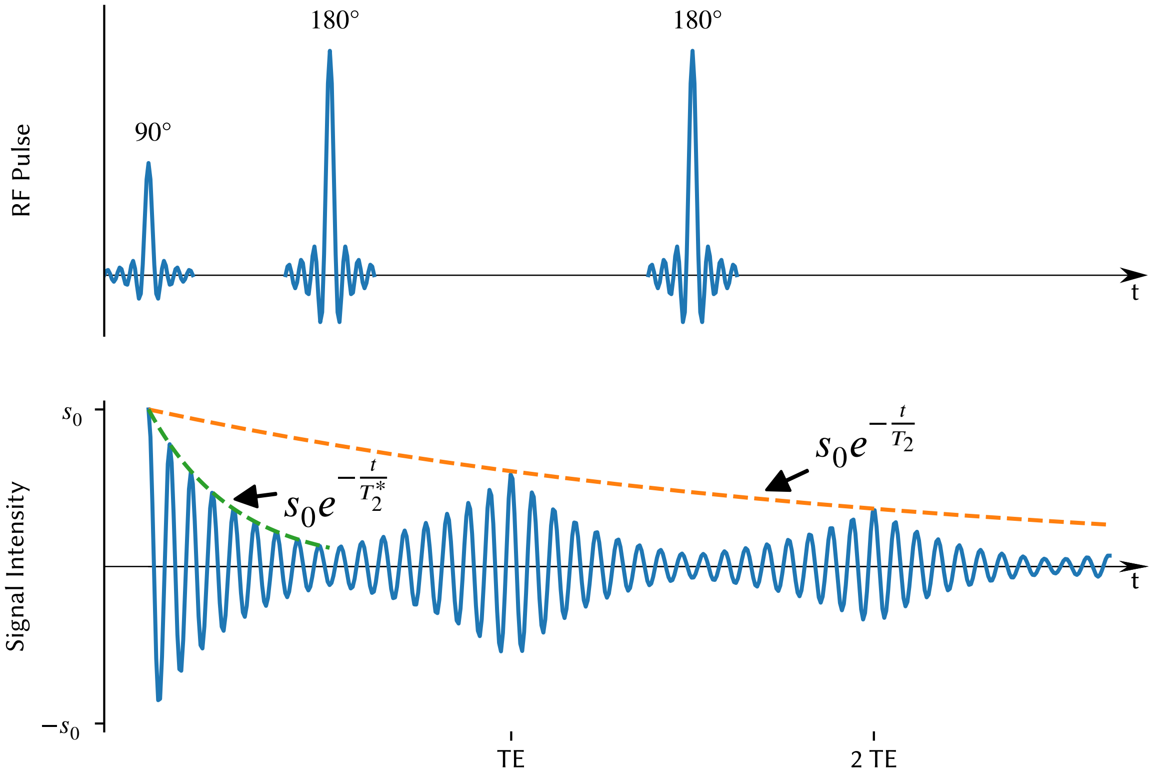

Figure 2.4.: Schematic signal decay of echo-planar imaging (EPI) sequences (cf. R. W. Brown et al. 2014a). The upper plot shows the RF pulses which are executed. Lower plot; The signal (blue) decays with T_2^* until a 180°-pulse rephases the signal. The refocusing pulse at TE/2 leads to realigned phases at TE and thus increased signal. During the whole time the signal decreases with the relaxation time T_2. This dephasing and refocusing is repeated several times.

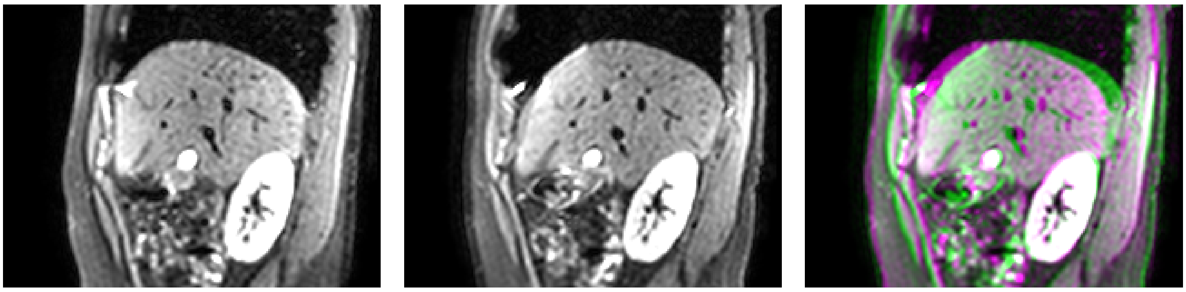

(a) Phase Encoding Direction Posterior to Anterior (⟵)

(b) Phase Encoding Direction Anterior to Posterior (⟶)

(c) Falsecolor Overlay

Figure 2.5.: EPI sequences have inherently high distortion in phase encoding direction. (a & b) This example shows a diffusion-weighted EPI (similar as used in this work: $b = 50\,\mathrm{s/mm^2}$, but in breath-hold, 1 average and echo train length of 51 ms) with opposite phase encoding directions (posterior ↔ anterior). The true position is expected to be between both extrema. (c) The falsecolor overlay visualizes the difference of both images. Regions with strong changes of Susceptibility, e.g. at the liver-lung interface, cause increased distortion. In all images the vendor provided distortion reduction is already applied.

these errors can sum up. For this reason a reduction of the echo-train-length is beneficial to reduce distortion. This also implies that distortion differs between sequences, and in deed, this is also observable between the EPI and GRE sequences (Figure 2.6).

To compensate for distortion in general, the field inhomogeneity is estimated. With this information the images are warped in the opposite direction during post-processing. However, the estimation of the field inhomogeneity in the required precision is not possible in tolerable time. For this reason simplifications are used which lead to the issue that the distortion is not fully compensated but reduced only.

2.4. Diffusion-Weighted Imaging

2.4.1. Diffusion

Diffusion is the physical process of the distribution of particles by random walk, in this work Brownian motion (R. Brown 1828). Since this is a statistical process only expectation values can be used.

Free diffusion can be described by its standard deviation (F. Laun et al. 2011)

$$\sigma(t) = \sqrt{\langle x^2 \rangle} = \sqrt{2Dt} \tag{2.10}$$

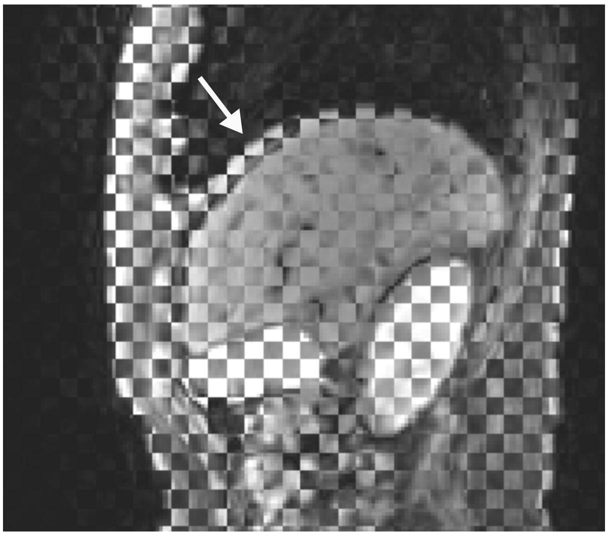

Figure 2.6.: Representative example for distortion in MR images of different sequences. Here GRE and EPI sequences (with diffusion weighting of $b = 50\,\mathrm{s/mm^2}$) are combined using a checkerboard combination. The different distortion in both imaging sequences is most prominent at the liver-lung interface (arrow). The distortion in the EPI sequence is higher than in the GRE sequence.

with x as the expected motion distance of a single molecule (in one dimension) during the investigated time span t. D is the (free) diffusion coefficient, the unit is $[D] = \mathrm{mm^2/s}$. The motion distance, observed for a huge number of particles and an adequately long observation time, follows a Gaussian distribution.

2.4.2. Diffusion-Weighted Magnetic Resonance Imaging

Diffusion-weighted imaging (DWI, also DW-MRI) is used to detect microscopic motion of water molecules. A change of this property can be an indicator for various diseases or damages, including stroke, multiple sclerosis, wallerian degeneration or hepatocellular carcinoma (Ayuso et al. 2018; Bammer 2003; Bonekamp et al. 2014). In radiation therapy it can be used for therapy evaluation (Chandarana and Taouli 2010).

DWIs are acquired by adding diffusion-weighting gradients to pure imaging sequences. Thus, DWI can be combined with a wide range of MR imaging sequences. However, due to the additional time for the gradients and the used repetitions, fast imaging sequences are preferred. One example is the diffusion-weighted single-shot echo-planar (dw EPI) sequence which is also used in this work.

To achieve diffusion-weighting two strong gradients are applied before the readout phase. They have opposite directions and the integral over time has to be zero. During these gradients a position-depended phase is accumulated. If no motion is present the phase accumulated during the first gradient is fully reversed by the second gradient. However, this cancellation does not happen if motion is present. Then phases are accumulated which lead to decreased signals. For this reason voxels with high motion appear dark in the final image (areas with low motion have increased signal).

The attenuation can be expressed by (Bammer 2003)

$$M_{\mathrm{SE}}(b, \mathrm{TE}) = M_0 \exp\left(-\frac{\mathrm{TE}}{T_2}\right) \exp(-bD) \tag{2.11}$$

for spin echo sequences. Here M_{SE} is the magnetization during readout, M_0 the steady-state magnetization, TE the echo time, b the diffusion-sensitizing factor ("b-value"), and D the diffusion coefficient. Similar descriptions exist for other sequences (cf. Bammer 2003).

TE and b can be directly set by the operator of the measurement. Hereby the scanner automatically calculates the gradient shape, amplitude, and pause between them by the given b-value in accordance with the system limits. Typical values for liver imaging are $0\,\mathrm{s/mm^2}$ to $1000\,\mathrm{s/mm^2}$ (Chandarana and Taouli 2010).

A major implication of DWI can be concluded from Eq. (2.11); with increased b-value, the signal is reduced. On the other hand, the noise is not. For this reason the SNR of DWI decreases with increasing b. To limit the loss of SNR, the measurement is repeated and averaged. For improved time efficiency, the number of repetitions is higher for higher b-values.

Another source of artifacts is macroscopic motion during the dw-gradients. This motion causes an additional phase to the magnetization (diffusion reduces the total magnetization but does not add phase). However, there are correction techniques available to mitigate these artifacts which are also known as motion correction (e.g. Anderson and Gore 2005; Porter and Heidemann 2009).

More details about DWI are presented in Bammer (2003), Chandarana and Taouli (2010), and F. Laun et al. (2011). Section 3.1.2 describes the sequence which is used in this work and its configuration.

2.4.3. Apparent Diffusion Coefficient

As can be seen in Eq. (2.11) the dw-signal is also T_2 dependent (measured signal $s \propto M$). So bright areas may indicate low diffusion coefficients or long T_2 (T_2 shine through). For this reason acquisitions with a single b-value are not sufficient. For this reason the apparent diffusion coefficient (ADC) is determined.

By repeating the measurement with different b-values (but constant TE), the signal decays (in first approximation) according to

$$s(b) = s_0 \exp(-D \cdot b)\,. \tag{2.12}$$

Thus, the diffusivity can be approximated by

$$\mathrm{ADC} = \frac{\ln(s_0/s)}{b} \tag{2.13}$$

with $s \propto M$ describing the measured signal intensity. The result is presented as apparent diffusion coefficient maps (ADC maps). There the result of Eq. (2.13) for each voxel is presented (Figure 2.7).

Equation (2.12) and thus Eq. (2.13) are only valid for free diffusion with Gaussian propagation — a condition which is often not fulfilled in human tissue. For this reason, the word "apparent" is part of the name. Further important effects to influence DWI are intravoxel incoherent motion (IVIM) for low b-values ($b < 50\,\mathrm{s/mm^2}$, Le Bihan 2019) or deviation from the Gaussian diffusion for high b-values (kurtosis, $b \geq 1000\,\mathrm{s/mm^2}$, Rosenkrantz et al. 2015).

2.5. Image Reconstruction

2.5.1. Fourier Transform

The current, clinical, state-of-the art image reconstruction method is the Fourier transformation (named after Fourier 1822). This algorithm makes use of the fact that the raw data $p(\mathbf{k})$ is acquired in the complex-valued k-space. This means that p is a function of wave vectors and the spatial information of the image $f(\mathbf{r})$ is encoded as frequencies and phases. The Fourier transform converts the k-space back into position space. In signal processing the Fourier transform and its inverse are often defined as (cf. R. W. Brown et al. 2014c)

$$f(\mathbf{r}) = \mathscr{F} p(\mathbf{k}) = \int_{\mathbb{R}^n} p(\mathbf{k})\, \mathrm{e}^{2\pi i \mathbf{k}\cdot\mathbf{r}}\ \mathrm{d}^n\mathbf{k}\,, \text{ and} \tag{2.14}$$

$$p(\mathbf{k}) = \int_{\mathbb{R}^n} f(\mathbf{r})\, \mathrm{e}^{-2\pi i \mathbf{r}\cdot\mathbf{k}}\ \mathrm{d}^n\mathbf{r}\,. \tag{2.15}$$

Since the measured data have to be digitalized, discrete fourier transforms (DFTs) are used (Deufelhard and Hohmann 2008). Typically, fast fourier transforms are preferred because they have the superior processing complexity of $\mathcal{O}(n \log n)$ over $\mathcal{O}(n^2)$ of other DFTs. However, fast fourier transforms require the input length to be a power of two ($2^n, n \in \mathbb{N}$) — which is

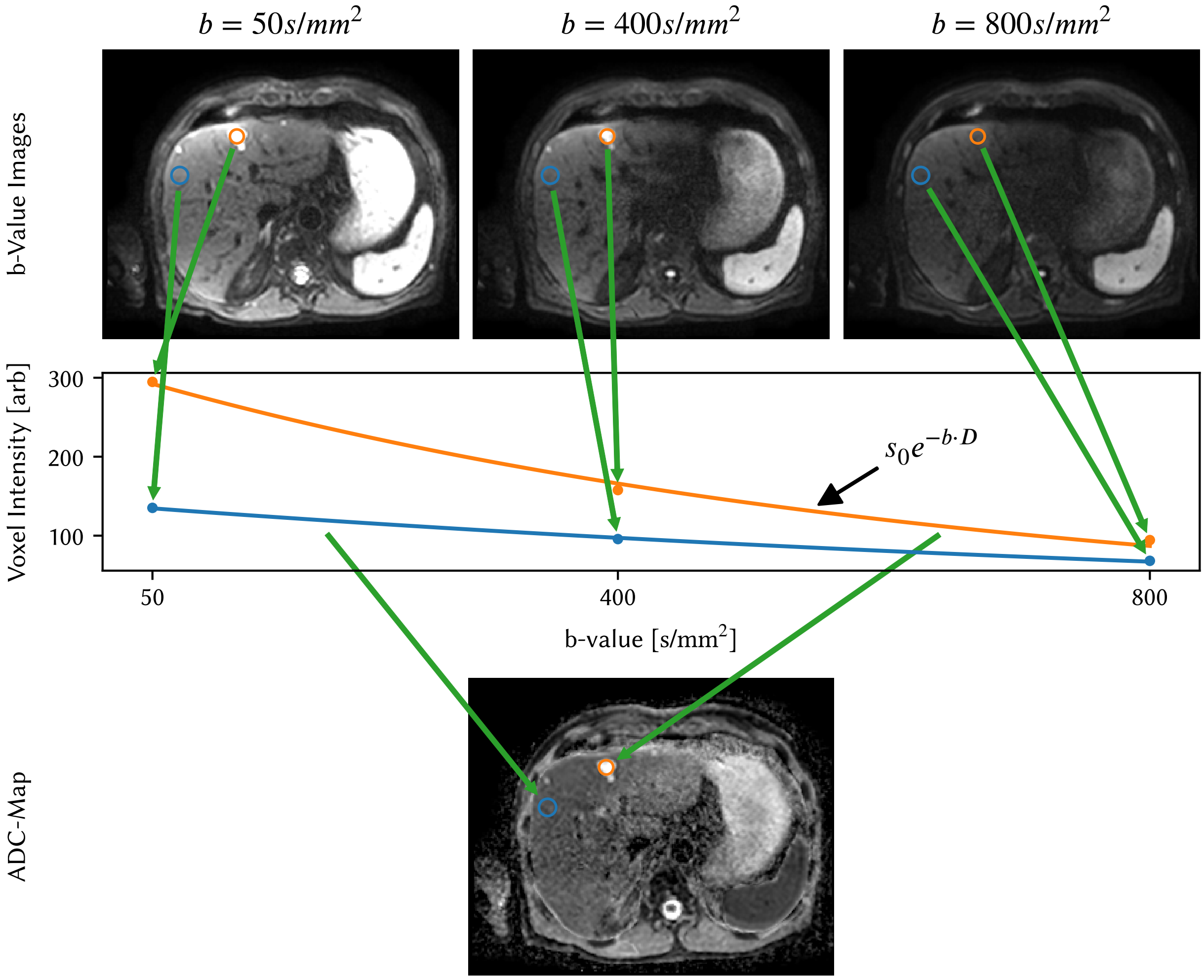

Figure 2.7.: Example for ADC calculation. DWI of the liver with different b-values $b = 50\,\mathrm{s/mm^2}$, $400\,\mathrm{s/mm^2}$ and $800\,\mathrm{s/mm^2}$ are used (top row). Note the exponential decay of signal intensity over the b-values and the concomitant decrease of SNR. This decay depends on diffusion in the tissue (red and blue ROI). The ADC-map shows the fit parameter D in a new, derived volume (bottom).

often achievable in MRI without drawbacks.

The DFT can suffer from alias artifacts if the Nyquist–Shannon sampling theorem (Nyquist 1924) is not fulfilled. This theorem requires all frequencies in the original signal to be lower than the Nyquist frequency

$$f_{\mathrm{Nyquist}} = \tfrac{1}{2} f_{\mathrm{s}} \,. \tag{2.16}$$

Here f_{s} is the sampling frequency of the measurement. Frequencies which are higher than f_{Nyquist} are erroneously spread over lower frequencies in a non-linear fashion. In (multi-dimensional) images this artifact often manifest itself as streaks (e.g. Figure 2.8b) — but depending on the undersampling pattern other manifestations are possible.

If the k-space is acquired in a non-cartesian fashion, e.g. in the form of stars as in this work (Section 3.1.1), the reconstruction is not directly possible by using DFTs. Instead, the irregular scan of the k-space is first resampled to a Cartesian grid. This method is called “gridding” and also used in this work. During the resampling the different distances between neighboring data-points are considered by applying an weight, which is inverse to the distance to the next neighbors (typically referred to as “density compensation”).

In this work many measurements intentionally do not fulfill the Nyquist-Shannon theorem. To prevent artifacts resulting from these “undersampled” data sets advanced reconstruction methods are used (see Section 2.5.4).

2.5.2. MRI Self-Gating Signal

The purpose of the self-gating signal is to generate a 1D curve which represents a motion, e.g. respiration or cardiac motion, over time. Additionally this signal is directly derived from the MR measurement without additional devices. Usages for this signal can be gating which filters data measured during a specific motion state (cf. J. Liu et al. 2010).

For self-gating a special property of the Fourier transform is used. If only the k-space center is considered, Eq. (2.15) becomes

$$p(\mathbf{k} = 0) = \int_{\mathbb{R}^n} f(\mathbf{r}) \, \mathrm{d}^n \mathbf{r} \,. \tag{2.17}$$

This shows that the k-space’s center is a sum over all intensities of the image (the image is a discretization). If an organ (e.g. the liver) is moving in and out of the image, this signal is proportional to that movement.

At this point, a further technique of MRI scans has to be described. For several reasons,

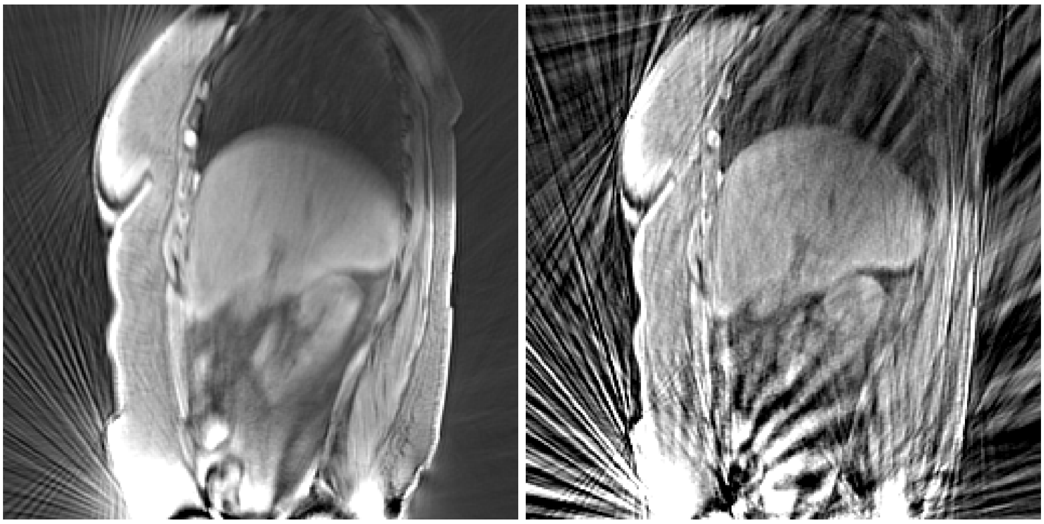

(a) Oversampled image (UF = 0.3)

(b) Undersampled image (UF = 3.1, end-exhale)

Figure 2.8.: Examples of fully sampled/oversampled and undersampled GRE images. (a) The image which fulfills the Nyquist-Shannon sampling theorem shows motion blurring due to the respiration during the (long) image acquisition. (b) The motion blurring can be reduced by using only parts of the acquired data. However, this leads to undersampling which causes streak artifacts. The radial distribution of the streaks is caused by the special k-space sampling as it is used in this study. Both images are based on a 3D image acquisition of about 5 min. (b) was generated by retrospective gating using only 10 % of the original data.

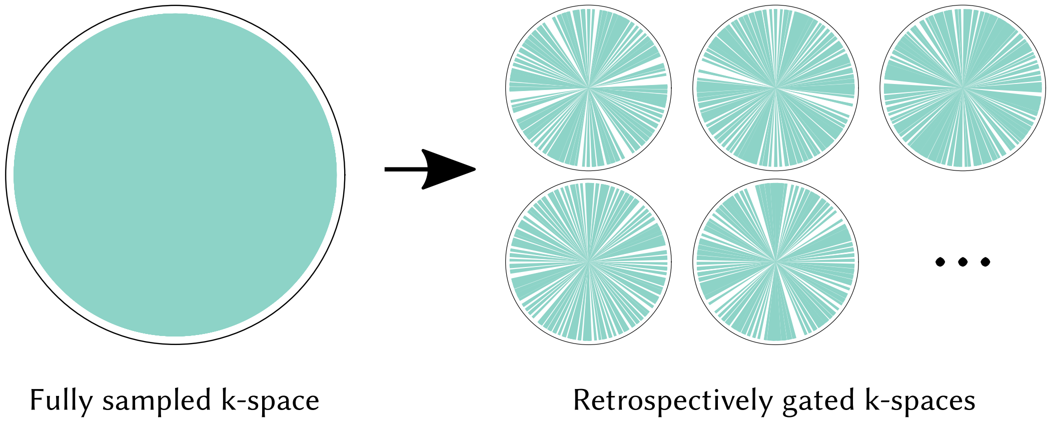

Figure 2.9.: Gating of the golden-angle stack-of-stars sequence (Section 3.1.1) in k-space. The gating splits the fully acquired k-space (left) into one k-space per motion phase (right). Since each phase only contains 10 % of the original spokes, gaps appear. The Nyquist-Shannon sampling theorem is not fulfilled anymore and the k-space is called undersampled. These gaps are the reason for the streak artifacts observable in Figure 2.8b.

the MR signal of the subject is measured by several, currently up to 128, coils. These coils are designed to have a limited field of view (coil sensitivity). Thus, there is (under non-artificial circumstances) always a coil which shows a structure which is moving beyond the borders of that's coil field of view. This coil can then be used to extract a signal as described above.

For increased robustness a more advanced technique is used (Paul et al. 2014; cf. Freedman et al. 2017). It extracts 5 data points around the k-space center (instead of 1) and the signal is extract using a principal component analysis (PCA) over all coils (instead of using a single coil). From the PCA the highest component in the frequency range of interest is used (0.1 Hz to 0.5 Hz for respiration).

2.5.3. Gating

Gating (rarely refereed to as "binning") is an easy and viable method to reduce artifacts caused by repetitive motion, e.g. respiratory motion. This is achieved by using only measurement data which is acquired in a specific motion phase. This phase can be determined by different sources, e.g. the self-gating signal (Section 2.5.2), a patient monitoring unit (PMU, Section 3.1.3), electrocardiogram (ECG, cf. Earls et al. 2002) or special imaging sequences (cf. Section 3.2.5).

Gating can be categorized into prospective and retrospective gating. The prospective gating is applied during the acquisition in a way that data is only acquired while the subject is in the desired motion phase. During the other time no measurement or auxiliary measurements are done. A common sequence for DWI uses the auxiliary measurement to determine when the subject reaches the next target motion phase.

In retrospective gating the measurement is performed without handling motion. Only afterwards, during the image reconstruction, one (or multiple) of the mentioned methods to determine the motion phase is used. With this information the measured data is filtered and data acquired during undesired motion phases is removed (Figure 2.9). The advantage of retrospective gating over prospective gating is that the whole measurement time can be utilized to create additional images of high quality but with motion induced artifacts. In this work the gated Fourier transform is described with the operator $X_{\text{PC}}(p)$ (PC: phase correlated, p represents the raw data).

However, gating of any type prolongs the measurement severely, increases by a factor of 3 and more were reported for respiratory gating in DWI compared to no motion handling (Shenoy-Bhangle et al. 2017; Taouli et al. 2009). For this reason pure gating is unfavorable in clinical use. In this study it is used as part of the joint-MoCo-HDTV (Section 3.2.2) and MoCo DWI (Section 3.2.3) algorithms.

2.5.4. Iterative Reconstruction

Modified Gradient Decent Reconstruction

In this work, gating often leads to undersampled data. To overcome the limitations imposed by this violation of the Nyquist-Shannon-Theorem (Equation (2.16)), additional information can be used (Lustig et al. 2008). Here the sparsity (existence of redundant information) of MRI-scans is utilized and incorporated into a high-dimensional optimization problem. In this way the artifacts caused by undersampling are iteratively removed.

The optimization problem to solve is (Ritschl et al. 2012)

$$\arg\min_{\mathbf{f}} c(\mathbf{f}) \text{ under the condition } \|X\mathbf{f} - \mathbf{p}\|_2^2 < \varepsilon\ . \tag{2.18}$$

Here $\mathbf{f}$ is the image (or volume) to reconstruct. The sparsity of the measured data is considered by the regularization function $c(\mathbf{f})$ with an $\varepsilon > 0$. This ε should be small enough to enforce the condition appropriately. X the system-matrix which projects the image $\mathbf{f}$ from position space into k-space. The measured data in k-space are denoted $\mathbf{p}$. This, second part is also called data consistency term.

The choice of the regularization function is crucial for the quality of the result. Common functions are the wavelet transform (Lustig et al. 2008) and the total variation (Candes, Romberg, and Tao 2006). In this work a special version of the total variation is used; the high dimensional total variation (HDTV, Rank 2016; Ritschl et al. 2012).

For optimization a modified gradient decent is used (cf. Ritschl et al. 2011). To find the optimum for Eq. (2.18) three steps are repeatedly performed; (1) direction search, (2) step-size search, and (3) ensuring the regularization condition.

The direction is the derivative of the error between the current estimate and the raw data with according forward and back projections between the image and k-space:

$$\mathbf{u} = \nabla E = X^{-1}(X\mathbf{f} - \mathbf{p})\,. \tag{2.19}$$

As before X is the system-matrix, X^{-1} is the respective inverse. The (n+1)'th estimation of the volume $\mathbf{f}^{(n+1)}$ is calculated by

$$\mathbf{f}^{(n+1)} = \mathbf{f}^{(n)} + \alpha\mathbf{u}^{(n+1)}\,. \tag{2.20}$$

In this formula α is the step size. It is determined with a backtracking line search (Boyd et al. 2011). The regularization is enforced by smoothing $\mathbf{f}$ after each update.

High Dimensional Total Variation Regularization (HDTV)

As described before the selection of the regularization term is crucial. While common and often used total variations only ensure spatial consistency, high dimensional total variation also uses temporal consistency which is made possible by the multiple motion phases (Rank, Heußer, Buzan, et al. 2016). At the same time, detected motion is used to prevent the temporal consistency term from removing motion or the introduction of motion blurring. To achieve this, the HDTV is defined as (cf. Ritschl et al. 2012; Rank 2016, p. 33)

$$\begin{aligned}
\mathrm{HDTV}\mathbf{f} &= \|\nabla_{x,y,z,t}\mathbf{f}\|_2 \\
&= \sum_{x,y,z,t}\Bigg(\frac{1}{\Delta d_x}(\mathbf{f}_{x,y,z,t} - \mathbf{f}_{x-1,y,z,t})^2 \\
&\qquad + \frac{1}{\Delta d_y}(\mathbf{f}_{x,y,z,t} - \mathbf{f}_{x,y-1,z,t})^2 \\
&\qquad + \frac{1}{\Delta d_z}(\mathbf{f}_{x,y,z,t} - \mathbf{f}_{x,y,z-1,t})^2 \\
&\qquad + \frac{\gamma_t^2}{\bar{v}_{x,y,z}^2}(\mathbf{f}_{x,y,z,t} - T_{t-1}^{t}\mathbf{f}_{x,y,z,t-1})^2 \Bigg)^{\frac{1}{2}}\,.
\end{aligned} \tag{2.21}$$

This sums all voxels in all four dimensions. $\Delta d_{\{x,y,z\}}$ are the distances between the voxels. γ_t is the (velocity-independent) weighting factor of the temporal part of the equation. T_i^j is the warping for motion compensation (see Section 2.6) and $\bar{v}_{x,y,z}$ the velocity of the specific voxel as given by T_i^j.

Please note that this makes the optimization problem Eq. (2.18) more complicated. So now not only a single image/volume but a 4D volume $\mathbf{f} = (\mathbf{f}_1, \mathbf{f}_2, \ldots, \mathbf{f}_{N_t})^\mathrm{T}$ is reconstructed. Thus the system matrix is replaced by the phase correlated transform X_{PC}. Also the previously described multiple coil channels and their sensitivity have to be considered. All details are published in Rank (2016).

2.5.5. Further Processing for Medical Image Reconstruction

The reconstruction of magnetic resonance images contain multiple, additional algorithms to handle further artifacts which were not described before. These handle intensity variations and alias artifacts among other things. Here these techniques are only described briefly because they are common knowledge but have potential influence on the results of MoCo DWI.

Normalization The sensitivity of the coils to detect the MR signal falls with the distance. For this reason the measured signal from inner parts of the patient to scan seems to be lower than at the surface. At the beginning of each measurement this effect is estimated and the signal is normalized in this regard. However, this method is error prone and may not compensate the error completely, especially due to imperfect estimation of the coils sensitivity (observable e.g. in Figure 2.5a).

Alias Artifacts Also known as wrap-around artifact, causes parts of the field of view (FoV) or surrounding areas to fold into the image. This is caused if the measured FoV is smaller than the object to measure. Oversampling prevents this kind of artifact but prolongs the acquisition duration, especially phase or partition[1] oversampling. To prevent both generalized autocalibrating partially parallel acquisition (GRAPPA) can be used. In this study this is especially utilized for the dw EPI sequence. The drawback of GRAPPA is a reduced SNR accompanied by increased acceleration.

---

[1] Partitions are a property of 3D sequences, see Section 3.1.1.

2.6. Image Registration and Motion Compensation

Image registration is the process which transforms data, e.g. an image or volume, from multiple coordinate systems into a common one. The coordinate systems can be caused by different imaging modalities (e.g. MRI and PET) but also changes in time, e.g. due to motion. Typically the transformation T is unknown and has to be calculated or approximated.

Registration algorithms consist of three components: the motion model, the objective function, and an optimization method (Sotiras, Davatzikos, and Paragios 2013). The motion models are roughly categorized into one of the three categories; rigid, affine or elastic (Figure 2.10). The categories have different complexity (in general rigid is the simplest) which results in different demands on the objective function and optimization methods. Naturally, more complex motion models allow to handle a higher variety of motion.

Rigid registration models can account for translation and rotation only. With affine models additionally shearing is possible. There are many common elastic models, most notably b-spline and "fully-deformable" models. B-spline models use a fixed number of control points. The displacement of the control points define the transformation at their positions, respectively. However, the number of control points is (usually) significantly lower than the number of voxels in the whole volume. Thus, the displacement of the voxels between these control points is interpolated by b-splines.

Even more degrees of freedom are offered if each voxel can be moved individually ("full-deformable"). The Demons algorithm (Thirion 1998) uses such a model and is thus used for MoCo DWI. The Demons algorithm generates a transformation which assigns each voxel of the destination image $\mathbf{f}_d$ its original position in the source image $\mathbf{f}_s$. In this work the transformation to coaling image $\mathbf{f}_s$ with $\mathbf{f}_d$ is denoted T_s^d, thus $\mathbf{f}_d \approx T_s^d \mathbf{f}_s$.

The objective function is sum of differences of intensity values. As each voxel is moved individually, this requires higher image quality compared to rigid or affine transformations. To reduce this dependence on single voxels and to utilize prior knowledge, smooth deformations

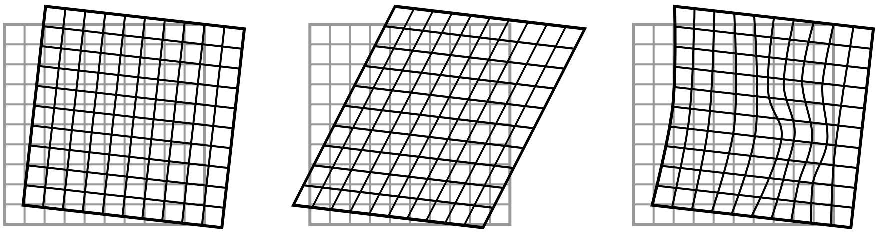

(a) Rigid registration (b) Affine registration (c) Elastic registration

Figure 2.10.: Three categories of the motion model of registration algorithms.

are enforced.

It was shown that image registration robustness is improved by a multi-resolution approach (Kostelec, Weaver, and Healy 1998). This is also used in the registration algorithms of this work. Rank (2016) further developed this principal to the joint-MoCo-HDTV algorithm (cf. Section 3.2.2).

2.7. Positron Emission Tomography in Combination with Magnetic Resonance Imaging (PET/MR)

Motion-compensated diffusion-weighted imaging (MoCo DWI) is developed for devices which combine positron emission tomography (PET) with magnetic resonance imaging (MRI). The reason for this are motion compensation techniques for PET images which are similar to MoCo DWI (cf. Catana 2018; Rank, Heußer, Wetscherek, et al. 2016). Thus, the MR sequence used to estimate the respiratory motion can be used for MoCo DWI as well as MoCo PET.

Integrated PET/MR scanners use a sandwich design to combine the coils required for MRI and the detector for PET (Figure 2.11). They are positioned in concentric rings around the bore (position of the object or subject to scan). As in wide-spread PET/CT devices, a radioligand is applied intravenously to the patient. The radioligand is chemically constructed in a way to accumulate in an area of interest, e.g. a tumor. For detection by the PET, the radioligand contains a radioactive tracer which decays by positron emission followed by positron-electron annihilation. In this way another contrast in addition to CT or MRI is possible. The most common radioligand uses fluorodeoxyglucose (FDG). This is a glucose analog where a hydroxyl group is replaced with the positron-emitting Fluorine-18 (^{18}F, Som et al. 1980).

The measurement time for PET per bed position is typically 2 min to 4 min (Martinez-Möller et al. 2012). Thus, respiratory motion is of concern. Several methods were proposed which detect the respiratory motion using golden-angle stack-of-stars MR sequences similarly to the one used in this study (cf. Section 3.1.1). The detected motion is then used to compensate respiratory motion in the PET images (e.g. Fürst et al. 2015; Grimm et al. 2015; Rank, Heußer, Wetscherek, et al. 2016).

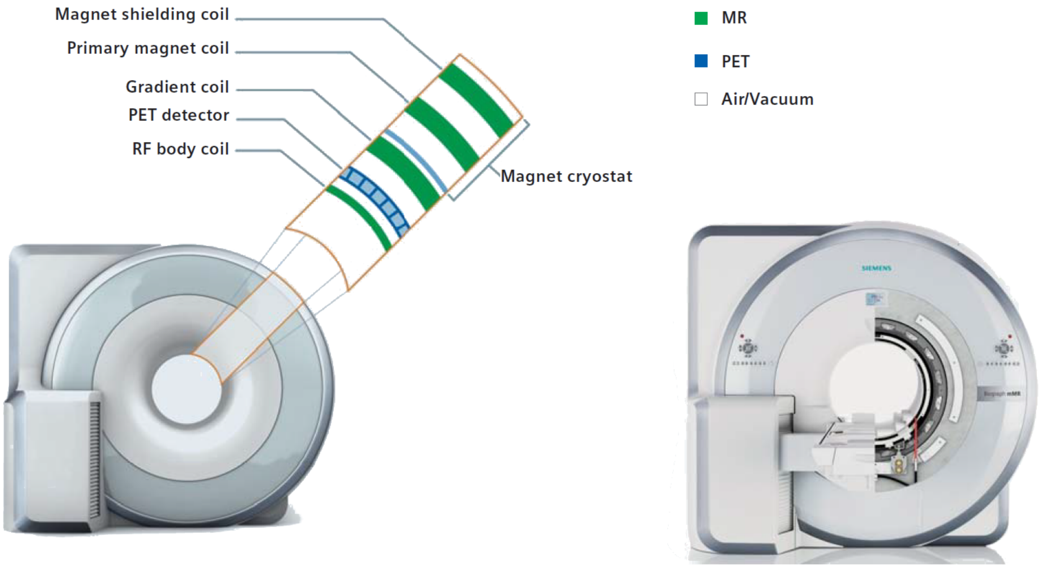

Figure 2.11.: Sandwich structure of the integrated PET/MR scanner Biograph mMR (Siemens Healthcare, Erlangen, Germany). Image source: Quick, Ladebeck, and Georgi (2011, fig. 2, modified).

3. Methods

3.1. Imaging Sequences and Data Acquisition

3.1.1. Golden Angle Gradient Echo Sequence

A golden angle, stack-of-stars gradient echo sequence (Winkelmann et al. 2007) is used as basis for the estimation of the motion model. However, here a special k-space acquisition pattern is used to allow efficient retrospective gating. In contrast to the common Cartesian pattern (Figure 3.1a) this 3D sequence acquires the k-space as a stack of stars (Figure 3.1b).

This means, the k-space lines are acquired in the form of spokes. Each spoke starts at the outside of the k-space, crosses the center of the stars' planes and ends at the opposite side ("outside-out"). Afterwards, the same angle but at the next k_z position is acquired. Therefore, the k_z direction in the k-space is also known as the partition direction. After acquiring this spoke along the partition direction, the next spoke is acquired in the same way but rotated by the golden angle of $\sim 111.25°$ (Kohler 2004; Winkelmann et al. 2007). Note that this pulse sequence acquires the images in a three-dimensional k-space. Often MRI pulse sequences use a 2D k-space only, while the third dimension is defined using slice selection (slice selection is also used in the stack-of-stars sequence but the selection contains the whole volume).

This acquisition pattern ensures that the k-space center is acquired regularly and with high temporal resolution. That allows to generate a self-gating signal which is based on the motion of the organs and not only patient's outside (Section 2.5.2). In addition, this radial trajectory has higher robustness against motion than Cartesian trajectories (W. Block and Wieben 2012).

For outside-out acquisitions the golden angle is about 111.25°. This way each additional spoke is placed in the largest gap of the star (Winkelmann et al. 2007). It is calculated using the golden ratio

$$\gamma = \frac{\sqrt{5}+1}{2} \tag{3.1}$$

and the angle which is required for one full turn in the outside-out pattern (180°). The angle

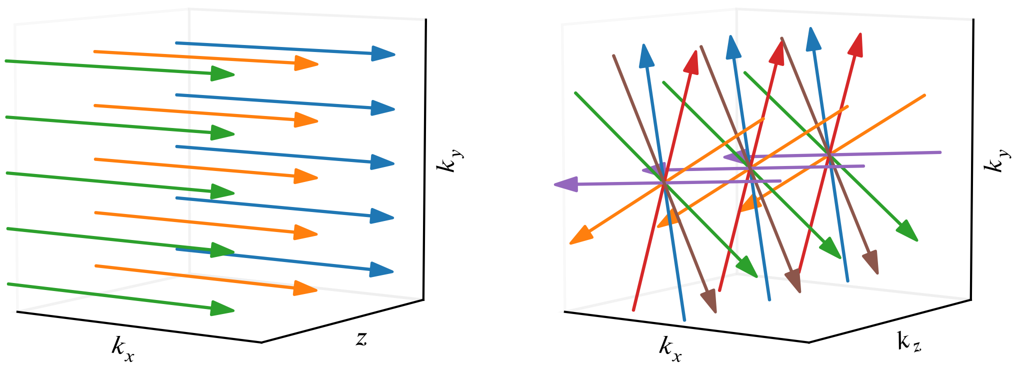

(a) Cartesian Trajectory (b) Golden-Angle Stack-of-Stars Trajectory

Figure 3.1.: The k-space can be acquired in different trajectories. In this figure k-space lines of the same color are acquired consecutively. (a) Cartesian trajectories are commonly used in medical imaging: here each slice is acquired separately in the spatial domain and the lines follow a grid pattern. (b) The golden-angle stack-of-stars sequence uses a radial trajectory with the golden angle (111.25°) between consecutive lines. The "stars" only differ in their k_z position.

is then $\Phi_{\text{golden}} = 180°/\gamma$.

The benefits of this acquisition pattern is that any connected subset of spokes has optimal (in-plane) distribution. Often it is mistaken that the optimal distribution is also fulfilled for non-connected subsets, which are caused e.g. by the gating process used in this study. However, the distribution is still highly spread which made this angle a favorable selection for many comparable studies (K. T. Block et al. 2014; Feng et al. 2016; Grimm et al. 2015; Johansson, Balter, and Cao 2018; Mickevicius and Paulson 2017; Rank, Heußer, Buzan, et al. 2016).

However, the sampling efficiency is decreased because the spokes are not equally distributed in the circle. This is also the reason why the Cartesian acquisition pattern is preferred for the diffusion-weighted echo-planar imaging (EPI).

In practical configurations, the plane of the individual stars has the highest resolution, in k-space and image space. Each of these planes is also refereed to as "partition".

The configuration of the sequence (Table 3.1) aims towards studies for motion compensation in PET/MRI. The sagittal plane orientation ensures high resolution in the main motion directions (Grimm et al. 2015; Hu et al. 2017). Short repetition times of TR = 3.5 ms allow fast imaging and lead to T1-weighted images. The acquisition duration of 4:47 min was chosen

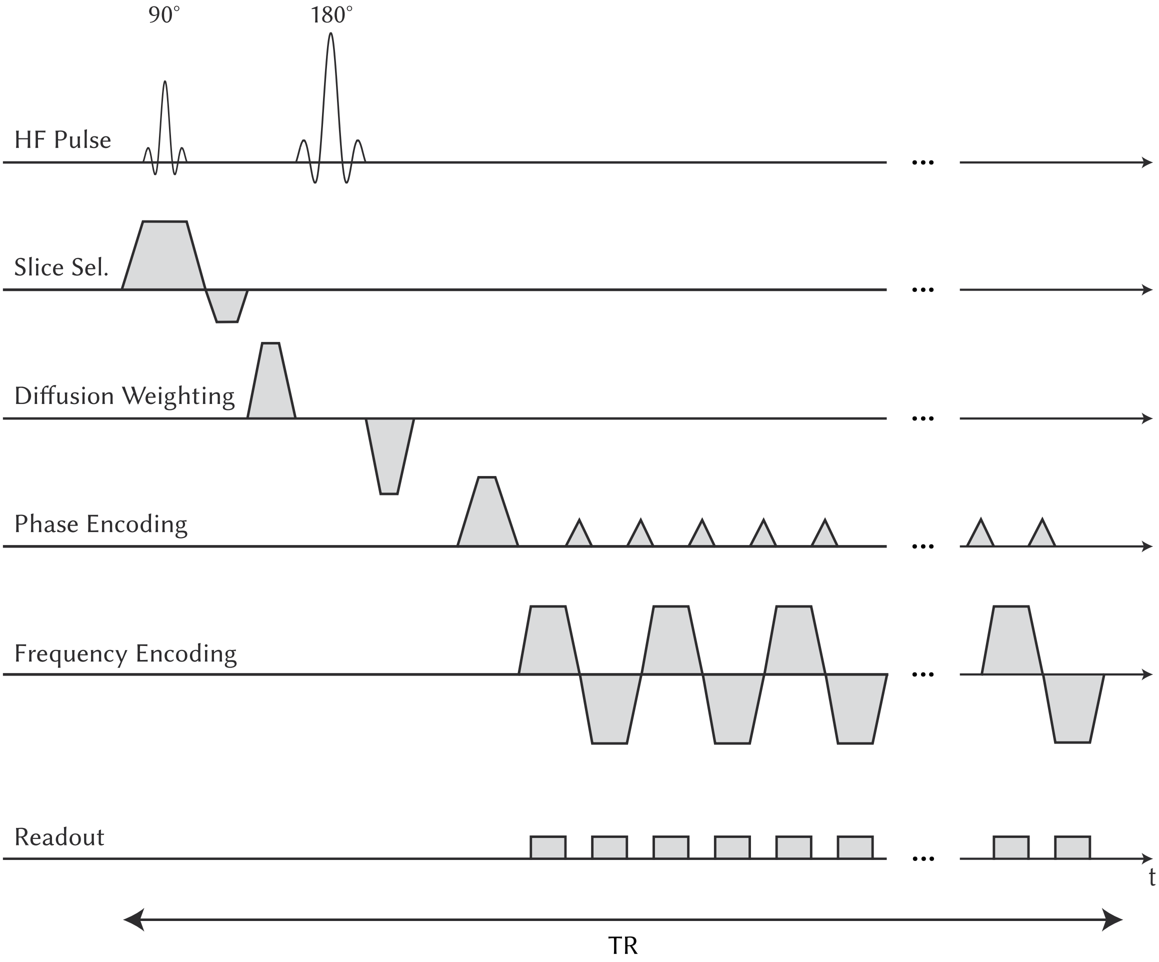

Figure 3.2.: Pulse sequence diagram of the single-shot, diffusion-weighted echo-planar imaging sequence. Axes are not to scale.

similar to the product of a major vendor of PET/MRI (Siemens Healthineers' BodyCOMPASS) because the motion model should be applicable for motion compensation of PET images, too. However, Rank, Heußer, Buzan, et al. (2016) showed that acquisition times of about 40 s are also feasible.

3.1.2. Diffusion-Weighted Echo Planar Imaging

For the DWI acquisition, a prototype diffusion-weighted echo-planar imaging (dw EPI) sequence is used. The sequences uses diffusion-weighting gradients before the acquisition of each 2D slice (Figure 3.2). The image acquisition itself is a EPI sequence to allow very fast readout (Section 2.3.2). By repeated acquisition of 2D slices a full 3D volume is assembled. To prevent cross-talk artifacts, first all even numbered slices of the stack are acquired and then the odd numbered slices (both in ascending order, Figure 3.3a).

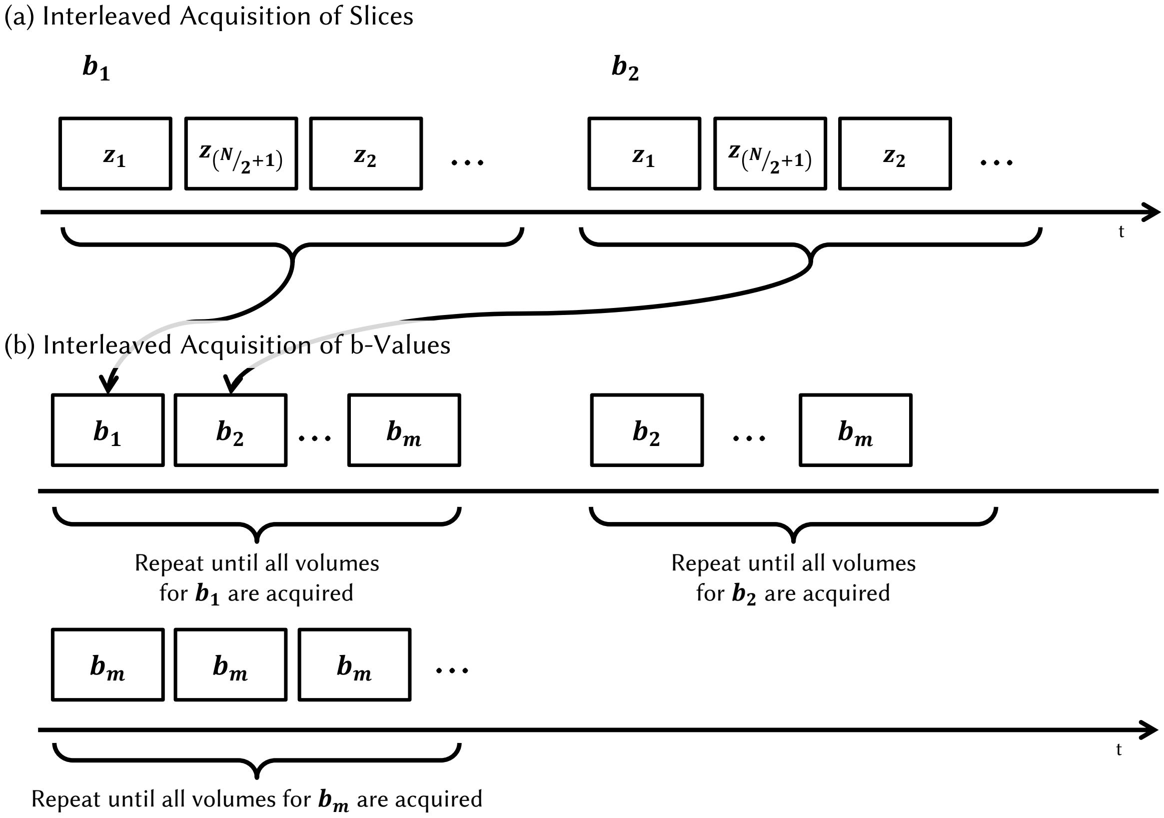

Figure 3.3.: Acquisition order of the interleaved dw EPI with N slices and the b-values $b_1, b_2, \ldots, b_\mathrm{m}$. (a) To prevent cross-talk artifacts first all odd slices are acquired followed by the even slices. (b) After the acquisition of a volume, the following volume is acquired with the next b-value. When the highest b-value was acquired this pattern is repeated until the desired number of averages for each b-value are reached. Since the number of averages typically increases with b-value, in the end (potentially) only one b-value is acquired repeatedly.

As described before, DWI typically use several averages (also named repetitions) to increase SNR – including the sequence used in this study. To consider the decreasing SNR with b-value, for higher b-values more averages are used. The b-values are acquired in interleaved mode (similar as the slices described before). One b-value is acquired after the other in ascending order. When all b-values are measured this is repeated until all averages for each b-value are measured (Figure 3.3b). Note that always a full 3D volume is acquired before any other parameter is changed (b-value or their repetition).

The configuration follows the recommendation of Taouli et al. 2016 for a typical DWI diagnosis of the liver, especially in the context of PET/MR. Only two adoptions are used. The number of averages for the lowest b-value ($b_1 = 50\,\mathrm{s/mm^2}$) were increased from 4 to 8 averages to reduce the holes in the retrospectively gated DWI (Section 3.2.3). Also the PAT factor was increased to PAT3 to allow shorter echo-train lengths of the EPI-part of the sequence. In this way the distortion is decreased (common vendor provided, software-based distortion reduction is used, too). Additionally, this also reduces the total acquisition time. The full configuration is shown in Table 3.1 and Table 3.2.

It is to mention, that the exact selection of the b-values is not of importance for MoCo DWI and its validation. The reason for this is, that MoCo DWI does not rely on the image (quality) of the DWI for the motion compensation algorithm. Thus any other b-values are also well suited for MoCo DWI.

Parameter	Model Estimation	Diffusion-Weighted Imaging (DWI)
Scanner	MAGNETOM Aera, Siemens Healthcare, Erlangen, Germany	
Field strength	1.5 T ($\omega_L \approx 63.7$ MHz)	
Sequence type	spoiled gradient echo sequence (GRE)	single-shot, diffusion-weighted echo-planar imaging (EPI)
k-space acquisition	golden-angle, stack-of-stars (3D)	Cartesian (2D, multiple slices)
Slice orientation	sagittal	sagittal / axial
Slice thickness	5 mm	5 mm
Repetition time (TR)	3.5 ms	7400 ms
Echo time (TE)	1.69 ms	47 ms
Bandwidth	490 Hz/px	2440 Hz/px
Flipangle	12°	90°
Spokes per partition (radial views)	1300	./.
Field of view	385 × 385 × 400 mm^3	308 × 380 × 210 mm^3
Acquisition matrix size	256 × 256 × 50 px	104 × 128 × 35 px
Image matrix size	256 × 256 × 80 px	208 × 256 × 35 px
Image voxel size	1.5 × 1.5 × 5 mm^3	1.48 × 1.48 × 5 mm^3
Slice distance	./.	1 mm
Acquisition duration	4:47 min	4:16 min
Undersampling per motion phase	3.1	./.

Table 3.1.: Overview of sequence configuration for the volunteer measurements. Further parameters for the dw EPI are listed in Table 3.2

Parameter	Value
Sequence type	single-shot, diffusion-weighted echo-planar imaging (EPI)
b-values	$(50, 400, 800)$ s/mm^2
diffusion-weighting direction	3D diagonal mode
averages	8, 8, 16
acquisition scheme	interleaved
GRAPPA acceleration	PAT3

Table 3.2.: Overview of parameters for the diffusion weighted sequence.

3.1.3. Respiratory Cushion / Patient Monitoring Unit

In this work two methods are used to track the respiratory motion: the self-gating signal (Section 2.5.2) and a vendor-provided cushion. The cushion is especially used for the DWI sequence because there a self-gating signal cannot be acquired (with common dw EPI sequences). For the cushion a belt is wrapped around the ribcage or upper abdomen of the patient. The foam-filled cushion is then located between the volunteer and belt (Figure 3.4a), the coil is put on top of both. During respiration the cushion is compressed and decompressed and thus is the air within. This airflow is detected by a connected ADC and sent wirelessly for storage. Since air pressure is measured this device is also referred to as pneumatic patient monitoring unit (PMU). It should be mentioned that the PMU measures the motion of the ribcage. Hence, the motion phase provided by the PMU can differ from the motion pattern of organs inside the abdomen.

For the volunteer measurements each volunteer was observed for several seconds to determine a suitable cushion position. Afterwards the signal received and shown by the MRI scanner was visually inspected, especially for under- or overflows of the signal range. If required, the cushion was repositioned. This procedure prevented unusable signals in most volunteer measurements, but could take up to several minutes. Also — while not observed during this study — the cushion could move during the measurement and may require repositioning. This makes the use of the respiratory cushion unfavorable for clinical use. However, the good availability and compatibility with nearly all MRI sequences is the reason for its use in many studies (e.g. Caldiroli and Minati 2007; Fontana et al. 2016; Y. Liu et al. 2017). Potential, alternative methods are discussed in Section 5.5.

Several preprocessing steps have to be applied before the PMU signal can be used as a gating signal. These steps are (1) smoothing of the raw signal, (2) shifting of the PMU signal to maximize absolute correlation with the self-gating signal (in the time range where both signals are available, Figure 3.5), (3) differentiating between in- and exhale phases by using a

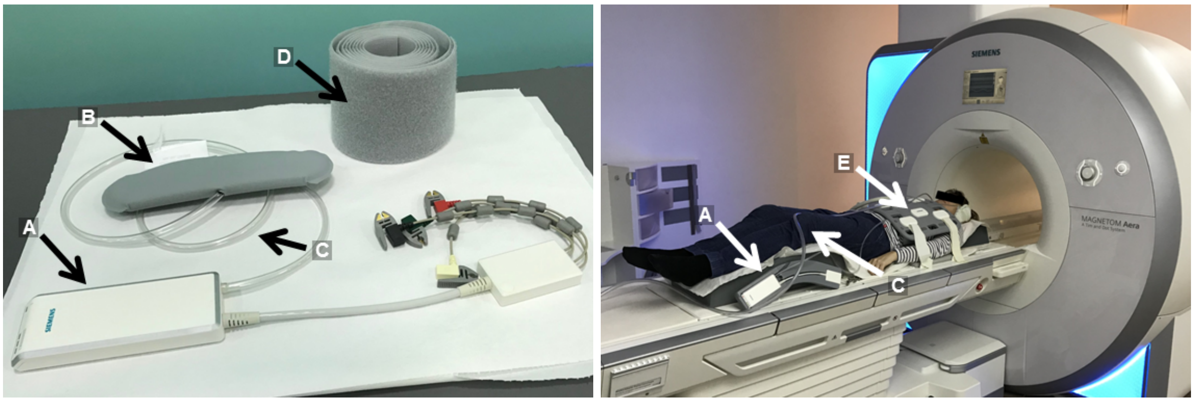

(a) Patient monitoring unit (PMU) for detection of respiratory motion.

(b) Positioning of volunteers.

Figure 3.4.: Volunteers are positioned head first, supine. The respiratory signal is acquired using a vendor-provided analog digital converter (A) which sends the signal wirelessly for further processing. The respiratory cushion (B) itself is fixed with a belt (D) and connected via a pneumatic tube (C) to the analog digital converter. On top of the cushion/belt is the upper receive coil (E).

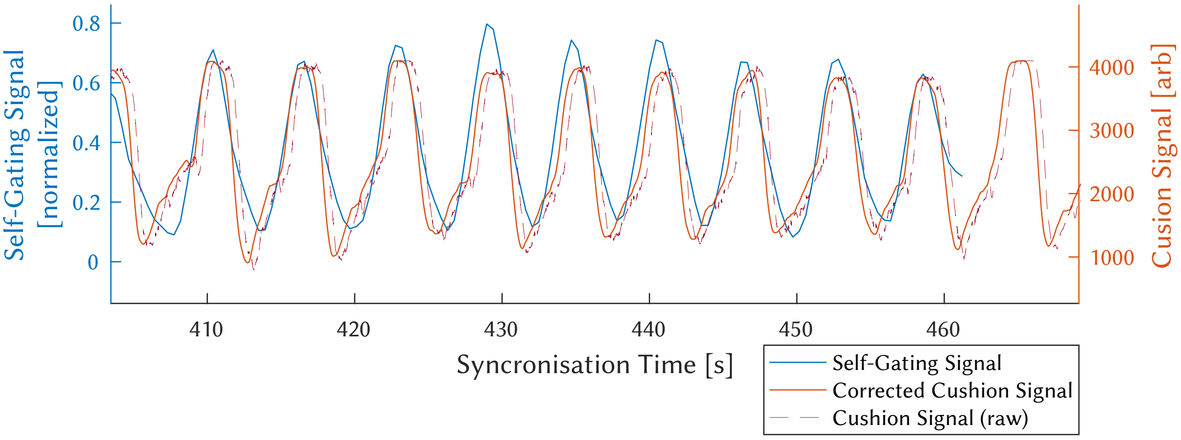

Figure 3.5.: Examples for the respiratory surrogate signals. Shown is a short window of the self-gating signal (blue) and the cushion signal (red). The cushion signal is smoothed first and then shifted in time by increase the correlation to fix potential, technical shifts (here by $222.5\,\mathrm{ms} = 2 \cdot T$(“resolution of self-gating”)). The self-gating signal is in general the more accurate source for retrospective (respiratory) gating. However, it is not available during the DWI sequence. For this reason there the cushion signal is used. Under- or overflows of the cushion signal were not always avoidable.

peak detection and (4) normalization to a fixed value range.

Note that the offset found in step (2) can account for a simple delay caused by physiological delays between the motion of organs (detected by the self-gating signal) and the ribcage. Additionally, another offset in the signal was observed, which was probably caused by technical reasons. (4) For normalization 95 % of the data were handled and the remaining data points are seen as outliers and assigned to the closest value in the desired rage.

3.2. Image Reconstruction and Post-Processing

3.2.1. Overview

The reconstruction and post-processing of the acquired MRI raw data can be separated into three main steps (Figure 3.6b):

1. estimation of motion based on the GRE sequence (Section 3.2.2),
2. gating of the DWI before averaging (Section 3.2.3), and
3. applying the estimated motion to DWI and combination of these (Section 3.2.4).

Additional steps like calculation of ADC-maps are described in Section 2.4.3. An extension to PET/MR with motion compensated PET imaging is sketched in Figure A.3.

3.2.2. Joint-MoCo-HDTV

In this study an adapted version of the joint-MoCo-HDTV algorithm (Rank 2016) is used to estimate the respiratory motion. The estimation is based on the acquisition with a golden-angle, stack-of-stars pulse sequence (Section 3.1.1). Characteristic for the joint-MoCo-HDTV algorithm are its five resolution levels to alternate between iterative reconstruction and motion estimation. The result is a 4D volume (three spatial dimensions per motion phase) of the imaged object or subject, and the deformation vector fields (DVFs) which describe the motion between the motion phases.

First, the acquired k-space data are retrospectively gated. Based on the self-gating signal $N_t = 10$ bins are identified using an adaptive amplitude gating (Section 2.5.2). The amplitude range for each bin is adapted. This prevents bins with too few k-space lines and thus images which are too dominated by streak artifacts for the image registration.

Starting with the lowest resolution level each bin is iteratively reconstructed with a high dimensional total variation (HDTV) constraint (Ritschl et al. 2012, cf. Section 2.5.4). Then the

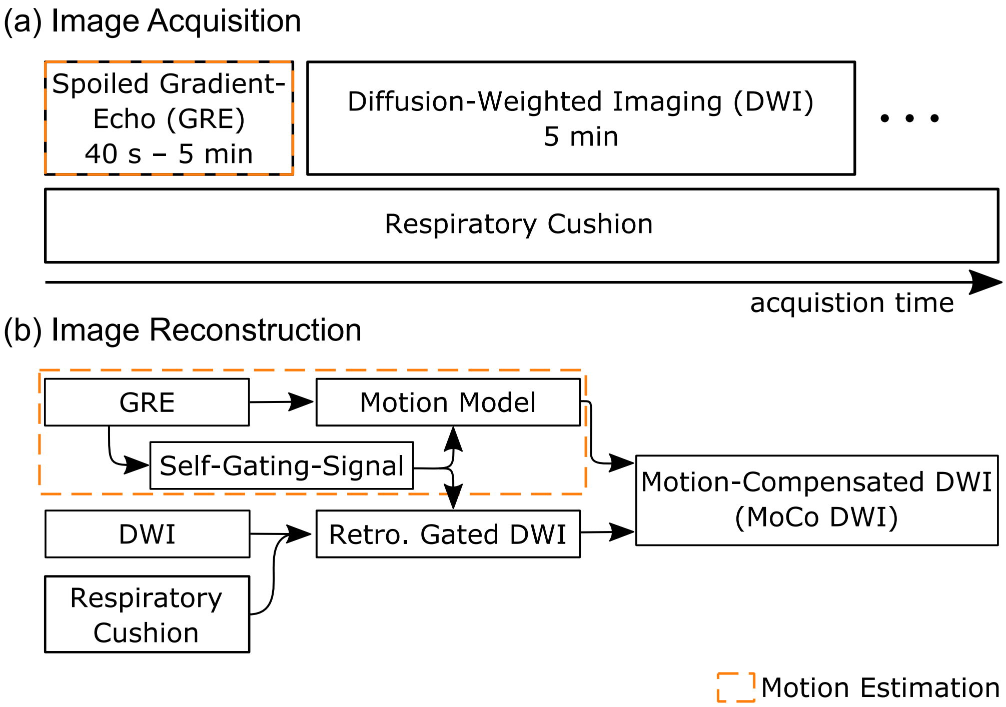

Figure 3.6.: (a) Image acquisition where the GRE for the motion estimation and the DWI pulse sequences are used. During the whole acquisition, the respiratory motion is assessed with a vendor-provided respiratory cushion. (b) The MoCo approach starts with the GRE sequence which uses self-gating to generate the motion model. The DWI sequence is first retrospectively gated using the respiratory cushion. The cushion and self-gating signals are aligned and then the motion model applied to the gated DWI leading to the final MoCo DWI.

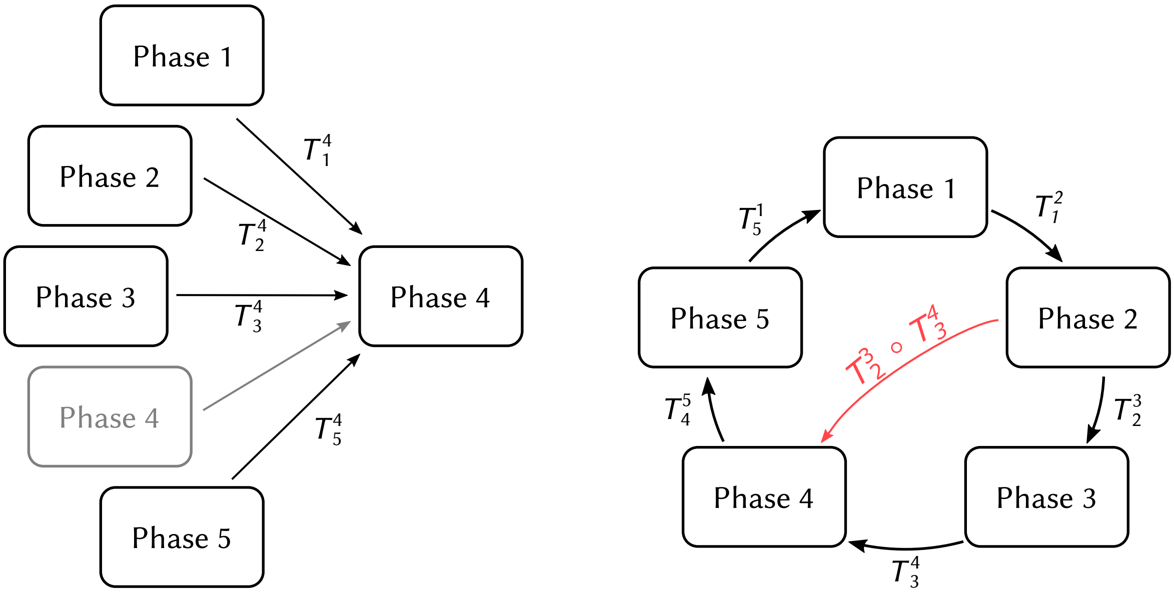

(a) Pairwise Registration (b) Cyclic Registration

Figure 3.7.: Different ways of image registration for exemplary five phases with target phase four. (a) Pairwise registration; Each phase is individually registered with the target phase. (b) In cyclic registration adjacent phases are registered (Brehm et al. 2012). For the transformation of non-adjacent phases the transformations T_i^{i+1} are concatenated (e.g. T_2^4 in red) — this is the method used in this study.

motion between adjacent phases is estimated using a multi-resolution Demons algorithm (Thirion 1998; Vercauteren et al. 2009), leading to the DVFs T_i^{i+1} ($i \in \{1, \ldots, N_t\}$, with cyclic behavior $T_{N_t}^{N_t+1} \equiv T_{N_t}^{1}$, Figure 3.7b). In the next resolution level $n+1$ the iterative part of the reconstruction is initialized with

$$\mathbf{f}_i^{(n+1)} = (1-\beta_n)\mathbf{f}_{\mathrm{HDTV},i}^{(n)} + \beta_n \sum_j^{N_t} T_j^i \mathbf{f}_{\mathrm{HDTV},j}^{(n)} \,. \tag{3.2}$$

All images $\mathbf{f}$ and DVFs T_j^i are upscaled to the resolution level $n+1$ before usage. The — also characteristic for this algorithm — weighting factor β_n increases with the resolution levels n from $\beta_0 = 0$ to $\beta_5 = 0.65$. In the last resolution level the reconstruction is repeated without the HDTV constraint but the DVF only. For further processing in MoCo DWI only the DVFs are used. The DVFs for not-adjacent phases are generated by concatenating adjacent vectors:

$$T_j^i = \prod_{k=j}^{i-1} T_k^{k+1} = T_j^{j+1} \circ \ldots \circ T_{i-1}^{i} \quad \text{for } j+1 \neq i \tag{3.3}$$

Again, the cyclic behavior of the DVFs is used here. The motion vectors are estimated between adjacent phases only to utilize the expected small variations between these phases. Therefore, the registration is expected to be more accurate than a registration between motion phases with high variations.

Additionally, a cyclic constraint is applied, which makes use of the prior knowledge that after a full respiratory cycle the starting point has to be reached again (Brehm et al. 2012). Thus, the constraint

$$T_1^2 \circ \ldots \circ T_{N_t-1}^{N_t} \circ T_{N_t}^{1} = \mathbb{1} \tag{3.4}$$

is enforced by calculating the error $\mathbb{1} - (T_1^2 \circ \ldots \circ T_{N_t-1}^{N_t} \circ T_{N_t}^{1}) = \mathbf{E}$ and then changing each DVF to $T'^{j}_{i} = \frac{\mathbf{E}}{N_t} T_i^j$ (voxel wise calculation).

Since this can lead to a underestimation of the motion, Rank (2016) developed another (undocumented) correction method. It introduces a compensation factor c_i which is calculated independently for every motion phase i. It is selected to minimize the sum-of-squares error

$$\underset{c_i}{\arg\min} \sum_{x,y,z} \Big(f_i(x,y,z) - \big((c_i \mathring{T}_i^i)\, f_i\big)(x,y,z) \Big)^2 \,. \tag{3.5}$$

Here explicitly the concatenation of all transformations $\mathring{T}_i^i = T_i^{i+1} \circ \ldots \circ T_{i-1}^{i}$ is used.

Publication	Topic of Research
Rank, Heußer, Buzan, et al. (2016)	MRI motion compensation in the lung and abdomen
Kolb et al. (2016)	Lung ventilation analysis
Rank, Heußer, Wetscherek, et al. (2016)	PET motion compensation for simultaneous PET/MR
Freedman et al. (2017)	Radiotherapy treatment planning for lung cancer
Menten et al. (2018)	Radiotherapy treatment planning for lung cancer in magnetic fields (MR-liniac)
Dolde et al. (2018)[a]	Pencil beam dose coverage in radiotherapy treatment planning
Dolde, Dávid, et al. (2019)[a]; Dolde, Schneider, et al. (2019)	Effect of immobilization devices for pencil beam radiotherapy planning
Dolde, Zhang, et al. (2019)[a]	Interplay effect due to respiratory motion for pencil beam radiotherapy treatment
Dolde, Naumann, Dávid, Kachelrieß, et al. (2019)[a]	Gating approaches to mitigate the interplay effect in pencil beam radiotherapy

Table 3.3.: List of previous studies which used the joint-MoCo-HDTV algorithm. In these publications the used versions of the algorithm differ in several details. ([a] The author of the present study co-authored these studies.)

In conclusion the joint-MoCo-HDTV is a multi-resolution image registration and reconstruction algorithm for (radial) MRI. It was used in ten peer-reviewed publications already (Table 3.3) and is thus a reasonable basis for the here presented MoCo DWI.

However, many technical improvements had to be made to allow the use of the DVFs for MoCo DWI. The most important change compared to the published version (Rank, Heußer, Buzan, et al. 2016) is a significant acceleration which reduces the reconstruction time by about 70 %. The average reconstruction time of the non-optimized joint-MoCo-HDTV in this study was 1:23 h (ranging from 0:51 h to 1:45 h) on a powerful desktop computer (Table 3.5).

3.2.3. Retrospective Gating for DWI

An integral part of MoCo DWI is the retrospective gating of the acquired DWIs. The goal of this step is to create diffusion-weighted images which are free from motion blurring, especially in-plane. The resulting images/volumes are in general not usable for diagnostics due to their low SNR and their proneness to artifacts (see Section 5.2 for details). In addition, these volumes can contain gaps which occur if for a given motion phase no slice at the gap's position was acquired.

For the gating each acquired slice of the DWI measurement is assigned to one of N_t bins. This is done comparable to the gating used in the joint-MoCo-HDTV but it is based on the signal of the respiratory cushion. Then the slices are recombined to volumes for each motion phase and b-value, which leads to $N_t \cdot \#b$ volumes. Since the image acquisition is done with fixed timing, the volumes are typically not complete but contain gaps (exceptions are possible).

For further processing these gaps, which contain no information, are handled in the way that the 4D volume (for each b-value) are interpreted as functions of the subset Ω:

$$\mathbf{f}^{\dagger}(\mathbf{r}, p)\colon \Omega \to \mathbb{U}^3 \times [1, \ldots, N_t] \tag{3.6}$$

$$\Omega \subseteq \mathbb{G}^3 \times [1, \ldots, N_t] \quad . \tag{3.7}$$

The subset Ω contains the voxels and phases where information is available. So Ω is typically a subset of the volume's grid $\mathbb{G}^3$ and motion phases. The implementation defined image domain is denoted $\mathbb{U}$.

3.2.4. Motion-Compensated Diffusion-Weighted Imaging (MoCo DWI)

The final step of the MoCo DWI algorithm is the deformation of retrospectively gated DWI and their recombinations into a single volume per b-value. Due to the gaps in the input volumes, default implementations for image warping cannot be used. It is important to mention that the motion vector fields T_i^j typically describe subvoxel motion. If not handled correctly, e.g. by setting the gaps to 0, this can lead to artifacts which are perceived as intensity variations. This would also alter the absolute intensity which would cause errors in derived images as the ADC-map.

To prevent artifacts from the gaps the warping is done twice. First on a volume in the full grid $\mathbb{G}^3$ which contains weighting factors and a second time on the actual, sparse volume. This is repeated for each motion phase and b-value independently.

The weighting factors are defined as

$$\begin{aligned} \mathbf{w}(\mathbf{r}, p)&: \mathbb{G}^3 \times [1, \dots, N_t] \to [0, 1] \\ \mathbf{w}(\mathbf{r}, p) &= \begin{cases} 0 & \text{if } (\mathbf{r}, p) \notin \Omega \\ 1 & \text{else} \end{cases} \end{aligned} \tag{3.8}$$

Ω contains all voxels which contain data, see Eq. (3.6), and $\mathbb{G}^3$ is again the full volume grid.

This way the final MoCo DWI volume can be calculated. For simplification the voxel position $\mathbf{r}$ is now omitted in the equations, the operations are performed voxel-wise. Also the regridding of the DVFs from the image grid of the GRE measurement to the final grid $\mathbb{G}^3$ is implied.

$$f_p = \begin{cases} \frac{1}{\sum_i^{N_t} T_i^p \mathbf{w}_i} \sum_i^{N_t} (T_i^p \mathbf{w}_i) \cdot (T_i^p \mathbf{f}_i^\dagger) & \text{if } \sum_i^{N_t} T_i^p \mathbf{w}_i \neq 0 \\ \emptyset & \text{else} \end{cases}, \tag{3.9}$$

with p being the reference or destination motion phase. The missing data ($\emptyset$) can be represented as floating-point `NaN`s (“not a number”) or filled with zeroes. While filling with zeroes results in more appealing images, it can potentially be mistaken for “low signal” where in fact no information is available. In this work the missing data are indicated red when the distinction is sensible. The missing data in f_p are not distributed slice-wise but may occur in any voxel regardless of its (in-plane) neighbors.

To account for subvoxel motion in T_i^p the volumes to deform are interpolated. So in the deformation

$$(T_i^p f_i)(\mathbf{r}) = f_i(\mathbf{r} + T_i^p(\mathbf{r})) \tag{3.10}$$

$\mathbf{r} + T_i^p(\mathbf{r})$ may not fall on the sparse image grid Ω. In these cases $f_i(\mathbf{r} + T_i^p(\mathbf{r}))$ is a linear interpolation of the eight neighboring voxels. Here also the inhomogeneous voxel distances are respected — whether caused by the inhomogeneous acquisition grid or the sparse volumes $\mathbf{f}^\dagger$. The interpolation is also the reason that the weights in $\mathbf{w}$ are not applied as step function but are smooth.

Note that the sum inside Equation (3.9) is not the same as using $\sum T_i^p w_i f_i^\dagger$ (first applying the weight factors followed by the warping operation) due to the required interpolation. For this reason the two, separate warp-operations are required.

For the acquisitions with axial plane orientation the images’ resolution is increased by a factor of 4 between slices. This is required, because the original resolution in that direction is about 6 mm and thus multiple times higher than the average motion between adjacent motion phases. Without this interpolation the warping $T_i^p \mathbf{f}_i^\dagger$ in Eq. (3.9) causes severe interpolation artifacts.

Extension to Other DWI Configurations

In this study only one gradient direction $\mathbf{G}$ for the diffusion-weighting is used. In the equations and descriptions above, this allows the simplification to distinct different diffusion-weighting configurations by the b-value only. However, the presented algorithm can also be used with multiple gradient directions. Then the distinction of the diffusion-weighting configurations is done by the tuple of b-value and gradient direction $(b, \mathbf{G})$ instead of the b-value alone. With this simple change all presented procedures can be used equivalently.

3.2.5. Alternative Methods

Several alternative methods to reduce respiratory-motion-induced artifacts in the abdomen are in clinical use or were proposed (Table 3.4). In this chapter a short review of these methods is presented to contextualize MoCo DWI. In general, respiratory motion handling for DWI can be grouped into prospective and retrospective methods. Prospective methods may or may not require support by the subject to measure. The retrospective methods can be sub-categorized into methods which use motion compensation. A comparison and classification compared to MoCo DWI is presented in Section 5.4.

Prospective Methods

Breath-hold From a technical point of view, the fastest accomplishable method is breath-hold. Before the measurement starts, the subject is told to hold the breath, often inhaled. Typically, this offers a time frame of 20 s to 30 s (Schmid-Tannwald et al. 2013) in which the respiratory motion is suppressed. To reduce the measurement time of DWI to this period of time, a trade-off between field-of-view, resolution, number of b-values and number of averages has to be made. For this reason, this is typically used only if few slices have to be measured. Multiple breath holds are possible but not favored in clinical use. Also, this adds the issue that reproducibility of the motion phases decreases while the patient fatigues. However, not all patients are able to hold their breath, e.g. patients with asthma, dementia or children (Gottumukkala et al. 2019; Jaimes and Gee 2016).

Publication	Sketch of Method
Common, cf. Chandarana and Taouli (2010)	Motion average (no motion handling, No MoCo)
Gottumukkala et al. (2019) and Shenoy-Bhangle et al. (2017) among others	Breath-hold
Kandpal et al. (2009), Nguyen et al. (2014), and Taouli et al. (2009) among others	Prospective triggering
Y. Liu et al. (2017)	Extension of measurement time to allow for loss-free retrospective gating
van de Lindt et al. (2018)	Retrospective gating with interpolation of missing data
Mazaheri et al. (2012) and Ragheb et al. (2015)	Affine registration
Guyader et al. (2015)	b-spline registration, groupwise intra-volume, pairwise between b-values
Sanz-Estébanez et al. (2018)	Combined ADC calculation with groupwise b-spline registration with total-variation constraint on ADC

Table 3.4.: Overview of work addressing respiratory motion during DWI.

Triggered Methods Also in clinical use are triggered methods. Here the measurement is started as soon as a specific motion phase is detected, typically the end-exhale phase. This detection can be done by several methods, e.g. by the cushion which is also used for MoCo DWI. More advanced techniques constantly perform a 1D GRE sequence to track the liver position. As soon as the liver reaches the desired position, the actual DWI measurement is started for a predefined amount of time. This procedure is repeated until all data are acquired. The result is a single 3D volume per b-value (averaging is possible).

This technique provides free-breathing image acquisitions. The acquisition can be supported by the patient by slower and shallow breathing to spend more time in the desired motion phase. Even with this support, the measurement time is prolonged by a factor of 2.5 to 3 (Taouli et al. 2009) or even more (Shenoy-Bhangle et al. 2017) compared to continues (motion ignoring) measurements. Another drawback is that (potentially large) parts of the measurement time are not used to improve the data acquisition but waiting.

Y. Liu et al. (2017) A variation of the triggered acquisition was proposed by Y. Liu et al. (2017). They performed constant measurements while using the previously described cushion for the detection of motion phases. The cushion signal is then used to determine when enough data for all motion phases are acquired. Only then the measurement is terminated[1]. However, the measurement is not adapted to the respiration in any other way. Afterwards, a retrospective gating (based on the cushion signal) is used to gain 4D DWI (Section 3.2.3). The measurement time was reported to be 5 min to 10 min (4 combinations of b-value and gradient-direction, no averaging, unstated number of slices).

Retrospective Methods

Recently more advanced methods to acquire free-breathing DWI were proposed without prolonging the measurement time.

Van de Lindt et al. (2018) suggested a similar technique to Y. Liu et al. (2017). But instead of prolonging the measurement time to prevent gaps, the inevitable gaps are closed by interpolation. This interpolation uses spacial as well as temporal neighbors. Furthermore, van de Lindt et al. (2018) used a self-gating signal (“self-sorting signal (SsS)”) based on correlation of the individually acquired slices to identify the motion phases.

---

[1] The publication was not precise on how the termination was performed. It is possible that the measurement time, required to fulfill the abortion criterion, was estimated before the measurement.

Retrospective Methods with Motion Compensation

Closest to MoCo DWI are algorithms which use motion compensation. Here four studies are sketched. Thereof one uses rigid, one semi-regid and the other two b-spline registrations in different ways. An important difference of these methods compared to MoCo DWI is that the motion is solely estimated on DWI.

Mazaheri et al. (2012) introduced a technique to compensate motion using affine registration. They use a similar DWI sequence as in MoCo DWI, where each acquired slice is treated independently of each other. The registration which uses mutual information as similarity measure, compensates rigid motion (translation and rotation) as well as shearing (each in all three dimensions). Thus, 12 parameters had to be estimated per slice.

Nevertheless, it was not possible to do so for higher b-values due to low SNR (they used 9 b-values in the range from 0 s/mm^2 to 800 s/mm^2). Thus, the registration was only performed on low b-values (the threshold for "low b-value" was determined empirically). These estimated parameters were then transferred to adjacent (high) b-values by interpolation.

To prevent long temporal distances, for each slice the b-values were acquired right after each other in an interleaved order (different from the sequence used for MoCo DWI where first the full volume for a fixed b-values was acquired). The registration was done pairwise with a single target volume. But is was not described in which way the target volume was selected. Accordingly, the results are 3D volumes in a presumable random respiratory motion state.

Ragheb et al. (2015) The "Local-Rigid Alignment (LRA)" uses a rigid registration algorithm with the option to drop slices. For the measurement a similar sequence to MoCo DWI is used. However, three b-values with three gradient directions each are measured. Furthermore, four averages for each volume are used, so in total 36 (non-averaged) volumes are acquired. The measurement time is 16:32 min.

The image registration is performed using a brute-force search to align body contours in the upper right quadrant of the abdomen (including parts of the liver). From the registered slices the 4 best-matching slices are used and averaged, the others are dropped. This is repeated for each combination of b-value and gradient direction. Afterwards, the three gradient directions are combined to single volumes per b-value. Since each slice is handled seperatly, including the ones in a single 3D volume, the image registration is not strictly rigid (semi-rigid).

As outstanding property of this method, Ragheb et al. (2015) highlight the quick reconstruction time compared to methods like Guyader et al. (2015).

Guyader et al. (2015) This proposed method uses three registration and motion compensation steps. The order of acquired slices and b-values is the same as for MoCo DWI (Section 3.1.2). Therefore, a groupwise image registration between the odd and even slices (each are acquired consecutively) is used ("intra-image registration"). Then a second groupwise registration co-alignes the volumes within each b-value. The final volumes are then gathered by a pairwise registration between b-values ("inter-image registration").

The b-spline registration (Klein et al. 2010) is performed with 64 mm distance between control points. Thus, there are three control points in the main motion direction.

Sanz-Estébanez et al. (2018) A different approach to image registration was proposed by Sanz-Estébanez et al. (2018). In this trail an iterative reconstruction was performed which integrated a spatial total variation (TV) constraint on the ADC-map with a groupwise, b-spline registration. In this way the image registration was consecutively updated to better fit the mono-exponential model. Further constrains foster smooth deformations. The advantage of this method is that all available b-values are utilized for image registration and not only two (source and target) as other methods described before.

3.2.6. Reconstruction Hardware

All reconstructions were done on a commercially available computer with 56 (logical) cores and 192 GB of RAM (Table 3.5).

Component	Configuration
System Model	Fujitsu CELSIUS R940power
Processors	2 × Intel Xeon CPU E5-2697 v8 (x64)
Cores	28 cores, 56 logical cores
Main Memory	192 GB (physically but not completely usable due to limitations of the operating system: 256 GB)
Operating System	Microsoft Windows 7 Professional (SP 1)
Compiler	Microsoft Visual Studio Community 2015, Version 4.0.25431.01 Update 1

Table 3.5.: Configuration of the reconstruction computer.

3.3. Evaluation

The evaluation of MoCo images for medicine is an ongoing issue (McClelland et al. 2013). The problem is that ground truths are typically not available or it is impracticable to create realistic ground truths for *in vivo* experiments. For this reason several quantitative measures — which are necessary for improved image quality — are evaluated in this study: the width of edges (edge response) and noise. Besides these, qualitative changes are presented.

3.3.1. Edge Response

The edge response (Smith 1997) is used to quantify the width of an edge. It targets to mimic human perception and results in low values (≥ 0 mm) for sharp edges. For a given line profile the edge response is defined as distance between 10 % to 90 % of the signal (Figure 3.9). This technique was also used in Dávid, Vahle, Grimm, Bachert, et al. (2019a).

The line profiles are positioned at three reproducible positions (Figure 3.8):

(a) The liver-lung interface at its most cranial position,

(b) the edge between gall bladder and liver, at the most cranial position of the gall bladder, as well as

(c) the edge of the right kidney in extension of its major axis.

Deviations of some pixels are possible if other structures would corrupt the edge response. This is especially the case if blood vessels are present. In volunteer 4 the gall bladder is only evaluated for $b = 50\,\text{s/mm}^2$ and $400\,\text{s/mm}^2$ because in the $b = 800\,\text{s/mm}^2$ volume the edge is not detectable due to low SNR. The same issue holds for volunteer 8 where the profile was replaced to cover the lower edge of the gall bladder.

3.3.2. Noise Evaluation

A comparison of signal-to-noise ratio (SNR) between the images without and with motion compensation is done, similarly to Guyader et al. (2015). Therefor, the upper five slices of the liver are segmented based on the motion average (No MoCo) volumes (Figure 3.10) with $b = 50\,\text{s/mm}^2$ and $800\,\text{s/mm}^2$. If the most cranial slice shows mainly the lung, the slice is ignored. This is to prevent significant influence of partial volume effects. The upper five slices are selected because they are more homogeneous than the lower parts since they typically do not contain large vessels. If vessels with a diameter of several pixels occurred anyway, they

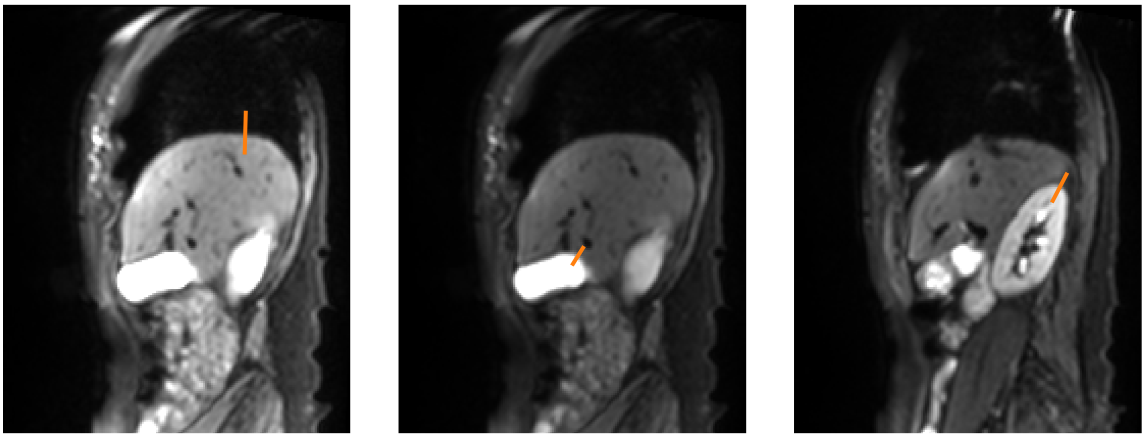

(a) Liver-Lung Interface (b) Gall bladder-Liver Interface (c) Kidney Tip

Figure 3.8.: Positioning of line profiles ($b = 50\,\mathrm{s/mm^2}$, windowing differs between all images)

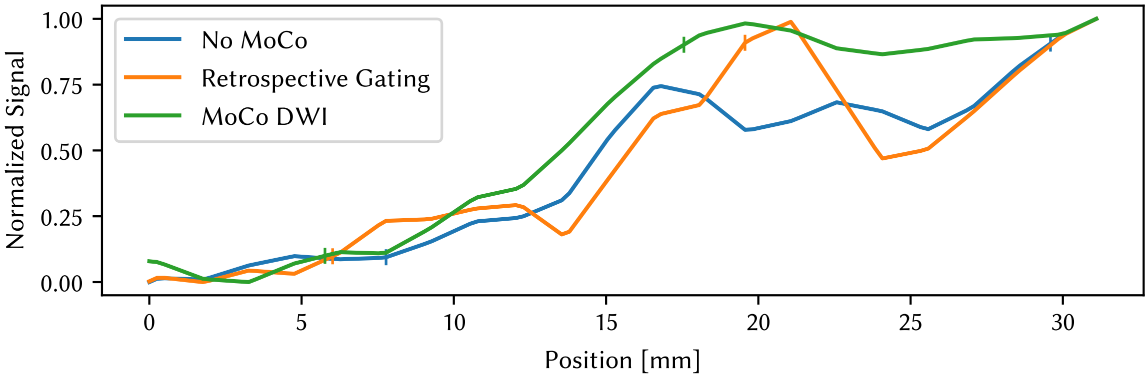

Figure 3.9.: Determination of sharpness via the edge response. The line profiles are extracted at the same position from the images (in this work only in-plane line profiles are used for highest resolution). The physical distance on the x-axis between 10 % and 90 % (marker) of the individually normalized lines' height are used as sharpness. Shown is a typical result for the liver-lung interface for $b = 800\,\mathrm{s/mm^2}$.

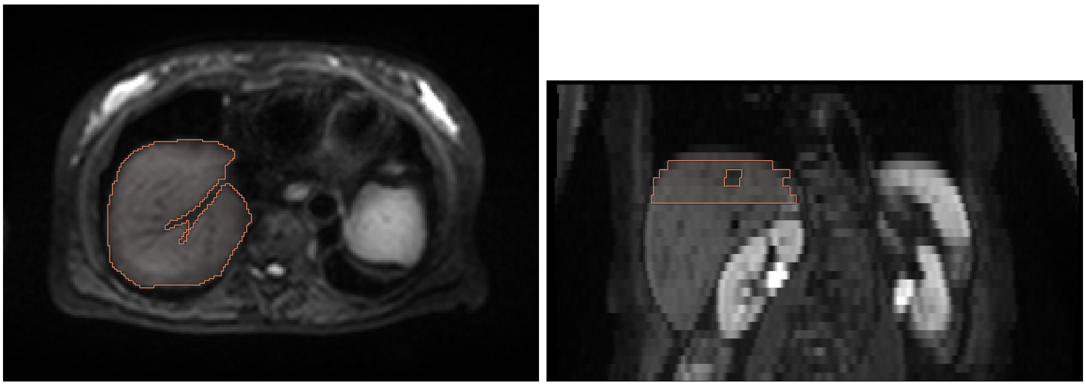

(a) Axial (in-plane) view

(b) Coronal view showing the five slices

Figure 3.10.: Positioning of ROIs for the evaluation of noise. The upper five axial slices of the liver are manually segmented, sparing larger vessels if necessary (as in this example).

are not part of the segmentation. To prevent errors caused by over-sized region of interests (ROIs), the segmentation is eroded by 5 pixels in-plane.

For evaluation of the noise the interquartile range (IQR) and 1.5 × IQR is used. The interquartile range (IQR) is defined as the width of the interval which contains the central 50 % samples. These quantities can be used for a wide range of noise distributions. This is important because MoCo DWI changes the noise distribution by averaging multiple images (Equation (3.9)). The noise distribution is typically not of interest for diagnosis, for this reason the type of distribution is ignored henceforth.

3.3.3. Apparent Diffusion Coefficient (ADC)

The effect of MoCo DWI on the apparent diffusion coefficient (ADC, Section 2.4.3) is evaluated qualitatively and quantitatively. The ADC-maps are calculated with a voxel-wise, mono-exponential fit (Equation (2.12)) using Python and Scipy. Since the lowest b-value in this study is $b = 50\ \mathrm{s/mm^2}$ the mono-exponential fit is adequate (no intravoxel incoherent motion effects expected). For the quantitative analysis the same ROIs as before is used (Section 3.3.2).

3.3.4. Gaussian Blurring ADC

This method was taken from Guyader et al. (2015) to ensure that the improvement of the ADC is caused by the motion compensation and not by the concomitant blurring of the volume. Also Ragheb et al. (2015) used a modified version of this technique. The method itself is not relevant for clinical use.

To test if blurring is dominant in causing the changes, this method blurs the volume of each b-value first. These blurred volumes are then used to calculate the ADC. The Gaussian blurring with $\sigma = 1$ pixel is applied in all three dimensions. Originally Guyader et al. (2015) selected this value to efficiently remove their most conspicuous respiratory motion induced artifact: the displacement of neighboring slices caused by the interleaved slice acquisition pattern (as in Figure 4.3b).

Differently from Guyader et al. (2015) the present study uses multiple averages as this is common in clinical use. So this artifact is not as prominent as in the previous study. The original configuration is used for best comparability, nonetheless. Also, the motion errors are the same, even if the consequences are not as prominently visible as in the original study.

4. Results

4.1. Volunteer Population

The measurements were done with healthy, professional volunteers who have experienced dozens or more MRI measurements before. All volunteers gave their informed and written consent before each measurement. They also had the opportunity to ask questions.

Eleven volunteers in the age from 33 years to 71 years (median 53 years) were measured. The body mass index (BMI) ranged from 19 kg/m^2 to 34 kg/m^2 (median 26 kg/m^2). The ratio of female volunteers was 45 % (full list of volunteers in Table 4.1). The body mass index is calculated as $\frac{w}{l^2}$ with w being the weight and l the body size (WHO 2004).

4.2. Joint-MoCo-HDTV

The reconstructions of the joint-MoCo-HDTV algorithm — which generated the motion vector fields for the following motion-compensated diffusion-weighted imaging — did not show unnatural motion in any but one volunteer (Volunteer 10, Figure 4.13). Deviations from this observation are possible at the edge of the FoV or the bowels – parts which do not affect the regions handled in this study.

Joint-MoCo-HDTV has detected motion mainly at edges/contrast changes, as expected. In most volunteers the detected motion amplitude (magnitude of the motion vector field), was higher at the upper and lower edge of the liver than in between (Figure 4.1).

Comparing the individual motion phases after warping to the final motion phase, and prior to recombination to the final joint-MoCo-HDTV volume, showed that motion is not compensated completely in all individuals (Figure 4.2).

4.3. Retrospective Gating for DWI

The respiratory gated volumes are an intermediate step of the MoCo DWI processing. In the representative examples shown (Figure 4.3), the reduction of motion blurring can be

Volunteer	Gender	Age [Years]	BMI [kg/m^2]
V1	F	49	28
V2	M	71	19
V3	F	55	34
V4	M	66	24
V5	F	46	25
V6	M	79	28
V7	M	67	27
V8	F	51	29
V9	M	63	27
V10	M	47	20
V11	F	33	26

Table 4.1.: Overview of volunteer population.

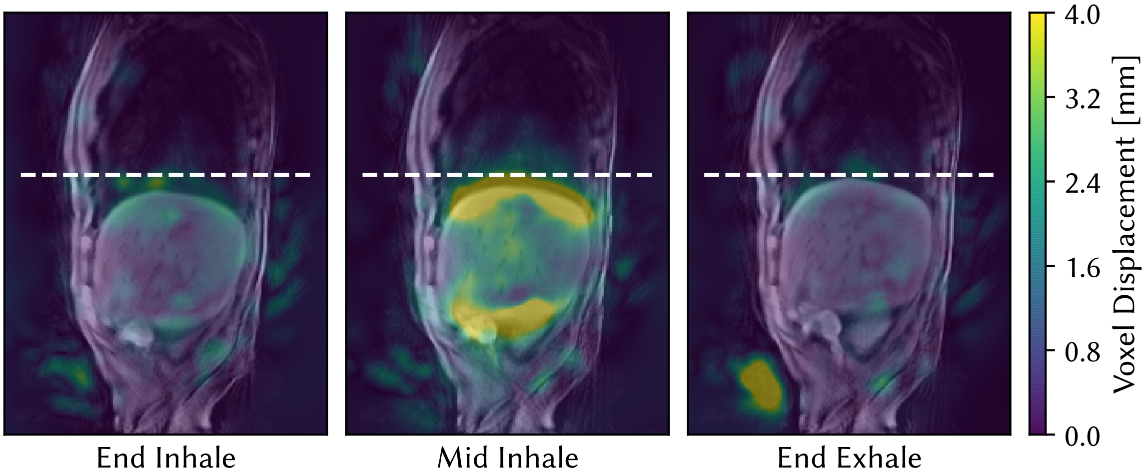

Figure 4.1.: Amplitude of motion vector fields determined by the joint-MoCo-HDTV between adjacent phases (three representative phases out of ten). For end-inhale and end-exhale the velocity is small. Most motion occurs in mid inhale and was thus detected there. At locations with contrast changes, especially edges, higher displacement was detected while in the inner part of the liver joint-MoCo-HDTV detected only small motion.

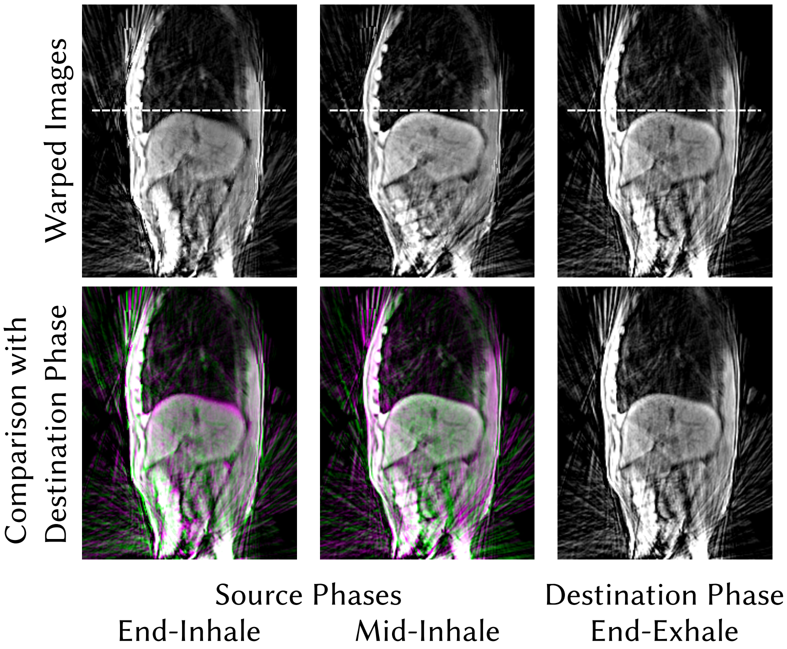

Figure 4.2.: Warped volumes from the joint-MoCo-HDTV algorithm before they were combined to the final volume. The color overlays of the warped images (left and center) and the destination phase (right) show that the respiratory motion is not fully compensated. Especially the end-inhale phase does not reach the desired positions in the liver and kidney.

Phase	Number of Gaps [slices] 8 avgs	16 avgs
All	17.0 ± 8.5	10.5 ± 7.9
End-Inhale	18.6 ± 6.2	10.4 ± 6.2
End-Exhale	15.6 ± 8.1	6.3 ± 5.7

Table 4.2.: Average number of gaps caused by retrospective gating of a volume with 35 slices into 10 bins.

observed. However, the gated images showed poor SNR and were prone to signal voids. Both adverse effects, low SNR and signal voids, increased with increasing b-values.

Additionally, the retrospectively gated volumes could contain gaps. These gaps occurred because each slice was assigned to a single bin after acquisition. On average 17.0 ± 8.5 of 35 slices were missing for the volumes with 8 averages and 10.5 ± 7.9 slices were missing if 16 averages were used. In the end-exhale phase only 15.6 ± 8.1 and 6.3 ± 5.7 missing slices were counted, respectively (Table 4.2). The given errors are the standard deviation.

The images without motion handling (No MoCo) can contain artifacts between slices which were caused by the interleaved acquisition scheme (e.g. in Figure 4.3b). They appeared as undulating edges between neighboring slices while the edges of every other slice were aligned. However, they were not visible in all data sets (e.g. Figure 4.3a). Similarly, motion blurring could not be observed or distinguished from other effects, in many slices of the No MoCo images, especially in the axial measurement protocol.

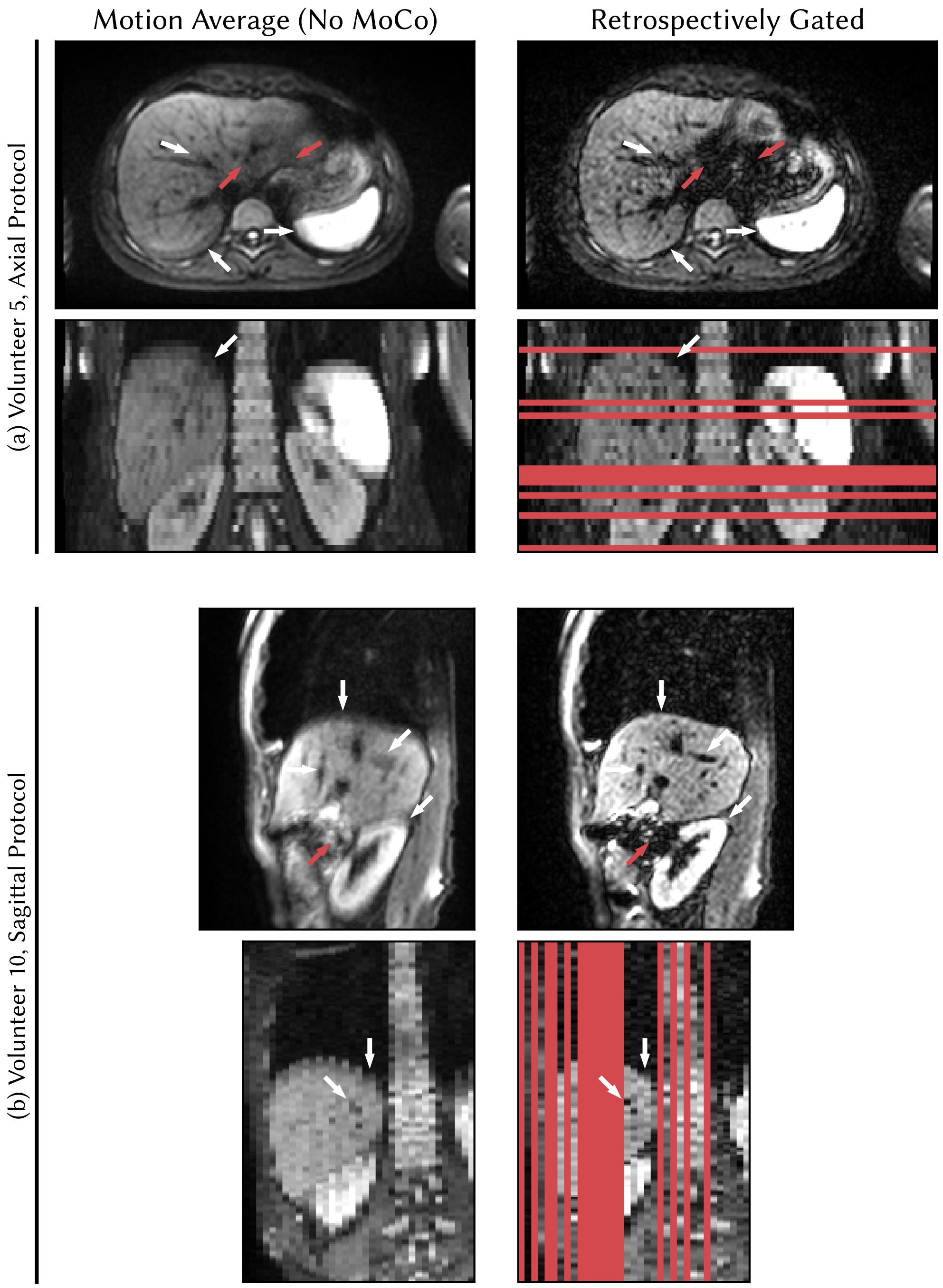

Figure 4.3.: Comparison of volumes ($b = 400\ \mathrm{s/mm^2}$, 8 averages) without motion handling (left) and retrospectively gated images (right). The No MoCo volumes show high SNR but suffer from motion blurring, especially at the edges of liver and kidney (white arrows). In the coronal view of (b) the motion artifacts stand out as undulating edges (white arrows). The motion artifacts are removed in the retrospectively gated images (right, here end-exhale phases). However, due to gating the image consists of few averages only which leads to low SNR and signal voids (red arrows). Also due to the gating, some of the 35 slices in the 3D volume are missing (red).

4.4. Motion-Compensated Diffusion-Weighted Imaging (MoCo DWI)

4.4.1. Qualitative Evaluation

The sagittal protocol offers the highest resolution in the main direction of motion. Thus, it is expected to be optimal for quality control since potential errors of the post-processing are not easily hidden by partial volume effects or insufficient resolution. Representative examples of two volunteers which differ in gender and physique (body mass index of 19 kg/m^2 and 29 kg/m^2) are presented (Figures 4.4 and 4.5). Without motion handling, especially the liver suffered from motion blurring (Magnifications A), but also smaller structures like blood vessels were blurred (Magnifications B). With MoCo DWI the motion blurring was clearly reduced (Figures 4.4 and 4.5).

The motion blurring was most prominent at the liver-lung interface and, to lower extent, at the upper part of the kidney (the sagittal protocol covered only the right kidney). Within organs the motion blurring was often not observable or not perceived as such. Also the validation based on these images only was challenging because the available ground truth — the retrospectively gated images — suffered from low SNR, and thus details were potentially unrecognizable due to noise. In the presented images this validation was possible. Also, many slices did not show (perceivable) motion blurring in the motion average images and thus an improvement or change was not expected. This happened especially in acquisitions with axial plane orientation which had low resolution in the main motion direction (Figure 4.6). Through-plane views (Figure 4.7) showed improved alignment of neighboring slices achieved by MoCo DWI (this artifact was not observable in all data sets).

Gaps in the volume which were observed in the retrospective gating were closed in the inner of the volumes. Typically, several voxels near the border of the FoV were not reconstructible. The end-exhale phase often showed better improvement than the end-inhale phases (e.g. Figure 4.6).

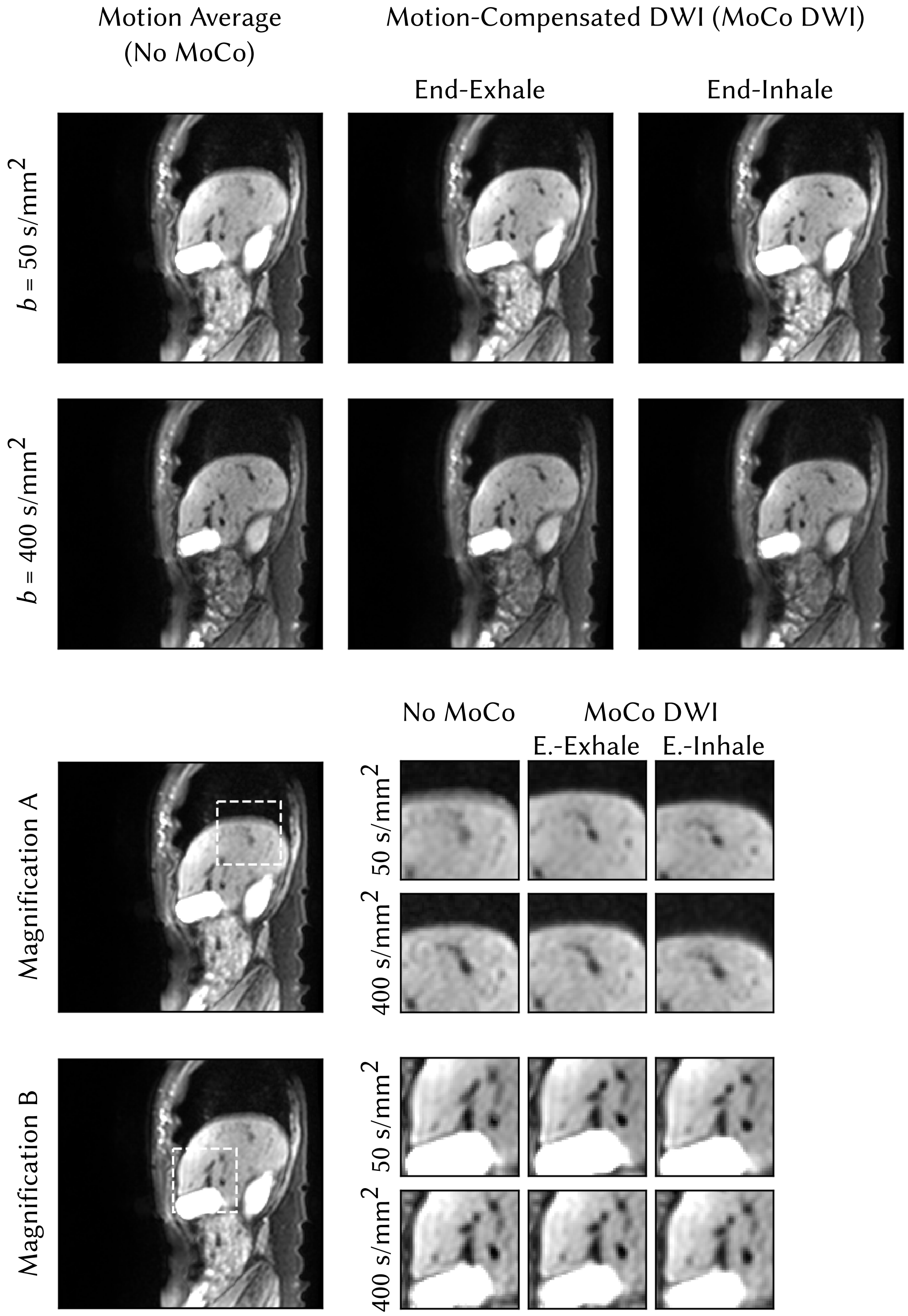

Figure 4.4.: Volunteer V2 (male, 71 yr, 50 s/mm^2 and 400 s/mm^2), in-plane view with comparison of motion average (No MoCo) volumes and motion-compensated diffusion-weighted imaging in end-exhale and end-inhale phases. (Magnification A) The improvement is most clearly observable at the interface of liver and lung. (Magnification B) Also vessels within the liver profit from the motion compensation. Another orientation of this volunteer is presented in Figure 4.7.

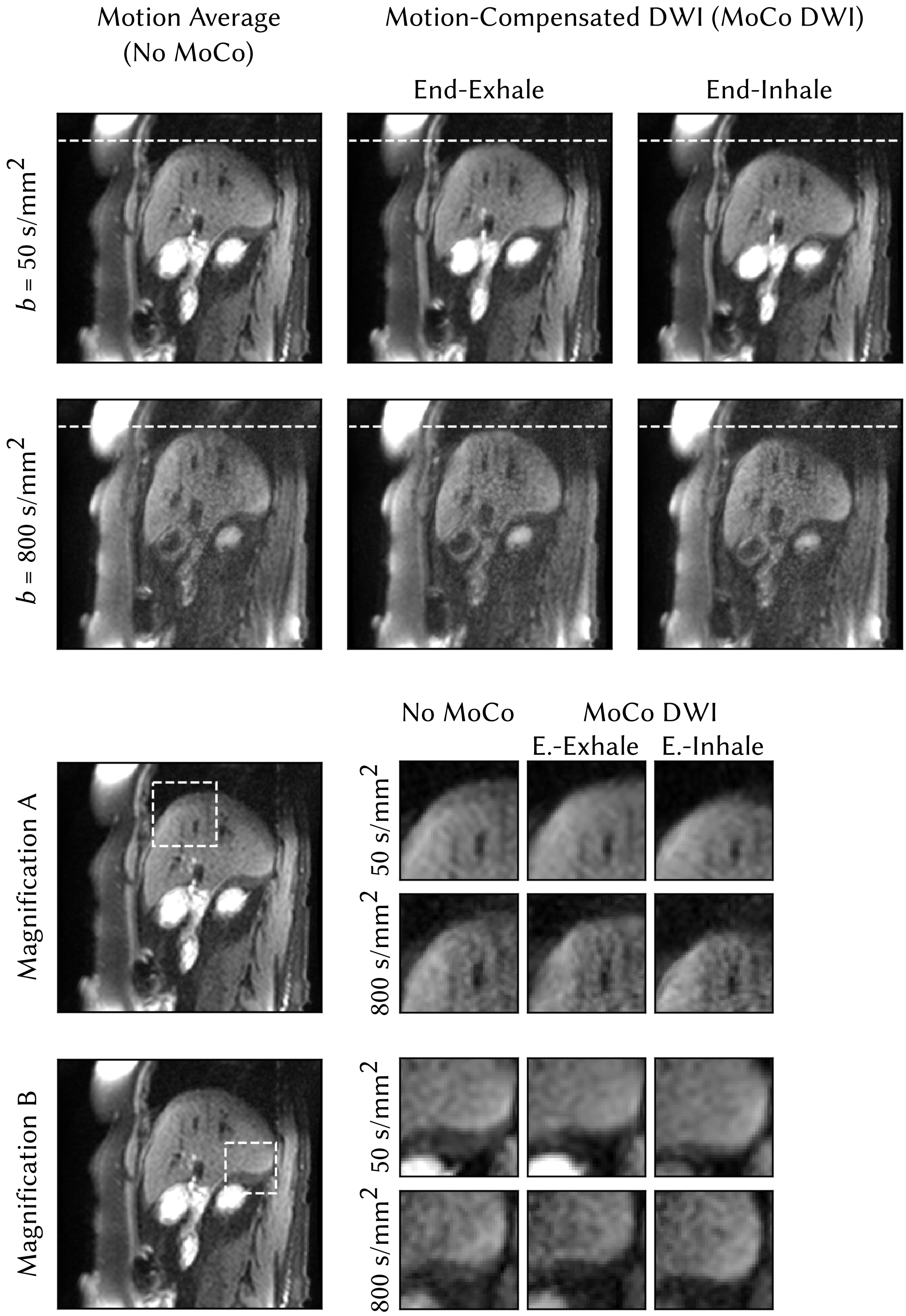

Figure 4.5.: Volunteer V8 (female, 51 yr, 50 s/mm^2 and 800 s/mm^2), in-plane view as in Figure 4.4. Motion blurring is clearly visible at the liver-lung interface (Magnification A) and close to the kidney (Magnification B).

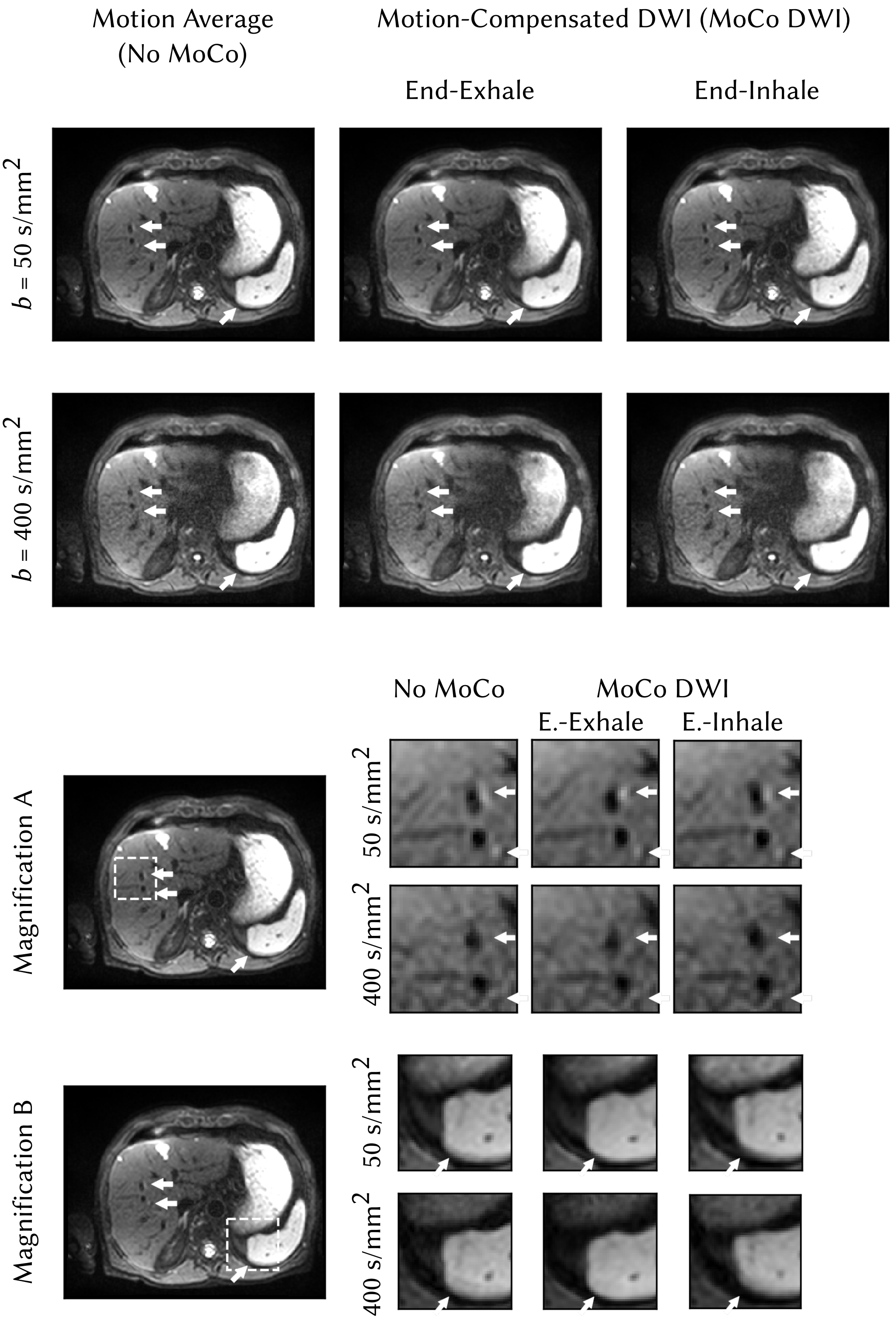

Figure 4.6.: Volunteer V4 (male, 66 yr, 50 s/mm^2 and 400 s/mm^2). Windowing adopted to the shown area and b-value. (Magnification A) Due to motion blurring fine structures were extended in motion average images and (Magnification B) the edge of the spleen was blurred. MoCo DWI does not show these artifacts.

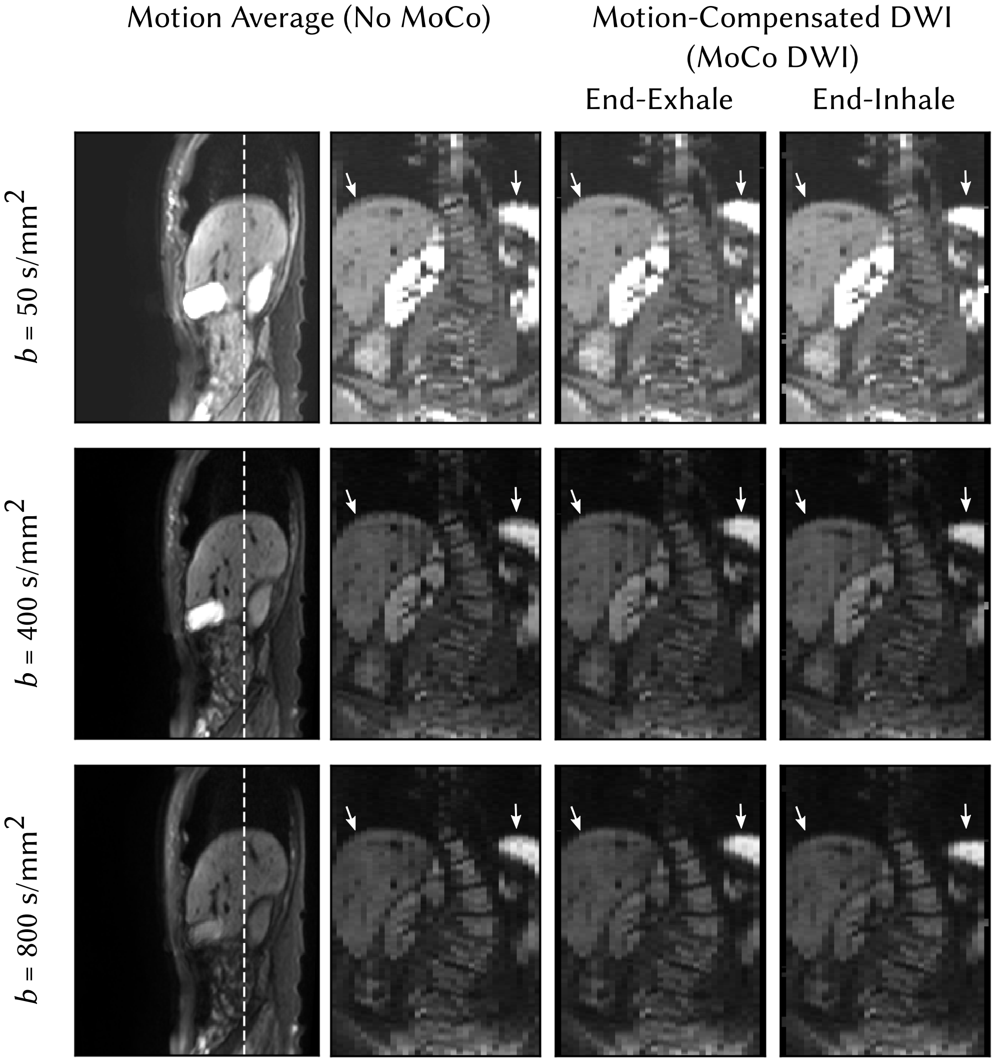

Figure 4.7.: Motion-compensated diffusion-weighted imaging (MoCo DWI) results for volunteer V2. The motion averaged images show motion blurring, and undulating edges between neighboring slices (arrows). Both could be solved with MoCo DWI.

4.4.2. Edge Response

For quantitative evaluation the spread of edges in several organs was evaluated (method described in Section 3.3.1). In all following evaluations the end-exhale phase in retrospectively gated DWI and MoCo DWI is used. The line profiles were examined at the interface of lung to liver (Figure 4.8), the right kidney's tip (Figure A.5) and the interface of the gall bladder to the liver (Figure A.4)

The liver-lung interface in MoCo DWI was at least as sharp as in imaging without motion handling in 9 of 11 volunteers (Figure 4.9a). In this regard, changes of about 1.5 mm were in the range of the resolution and thus considered unchanged (V3, V7, V5). Only in V1 and V6 a decrease of sharpness by MoCo DWI was observed.

The other line profiles were (potentially) positioned diagonally. So the resolution was reduced up to 2.5 mm (pixel diagonal). Taking this into consideration MoCo DWI was often similar (8 cases) or superior (3 cases) to No MoCo at the gall bladder-liver interfaces. The sharpness of the right kidney's tip showed mixed changes.

The measurement was evaluated using the Wilcoxon-Signed Rank test. It indicated an improvement of sharpness of line profiles by MoCo DWI. However, the number of volunteers measured was not large enough to statistically confirm the hypothesis that MoCo DWI shows an improvement for clinical application (p-values > 0.05, Table 4.3).

4.4.3. Noise Evaluation

Noise is a major concern in MRI and especially in DWI. To test for changes of noise caused by MoCo DWI an ROI (Section 3.3.2) in the liver was evaluated at parts where homogeneity is expected (Figure 4.10). The ROIs contained at least 11 766 voxels, except for the retrospectively gated volumes where the ROIs could contain less voxels due to gaps. However, the lowest valid ROI contained 2298 voxels and in two volunteers (V2 $b = 50\,\mathrm{s/mm^2}$ and V6 $b = 400\,\mathrm{s/mm^2}$) no data at all were available because no slice of retrospective gating in the end-exhale phase was in the ROI. On average the ROIs contained $(20\,449 \pm 5047)$ voxels

Position	Number of Profiles	Wilcoxon Signed-Rank	p-Value
Liver dome	33	192	< 0.06
Gall bladder	30	181	< 0.15
Kidney Right	33	249	< 0.29

Table 4.3.: One sided Wilcoxon signed-rank test for sharpness improvements of selected edges.

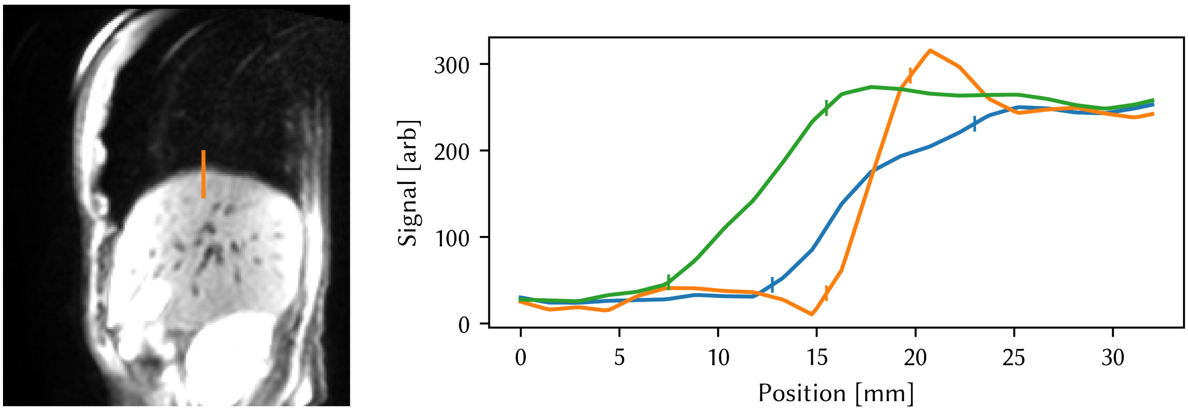

(a) $b = 50\,\mathrm{s/mm^2}$

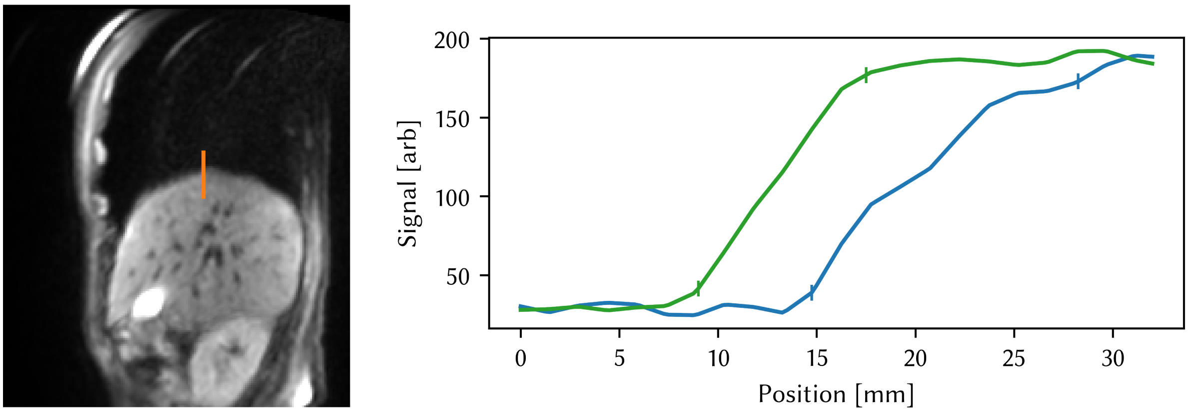

(b) $b = 400\,\mathrm{s/mm^2}$

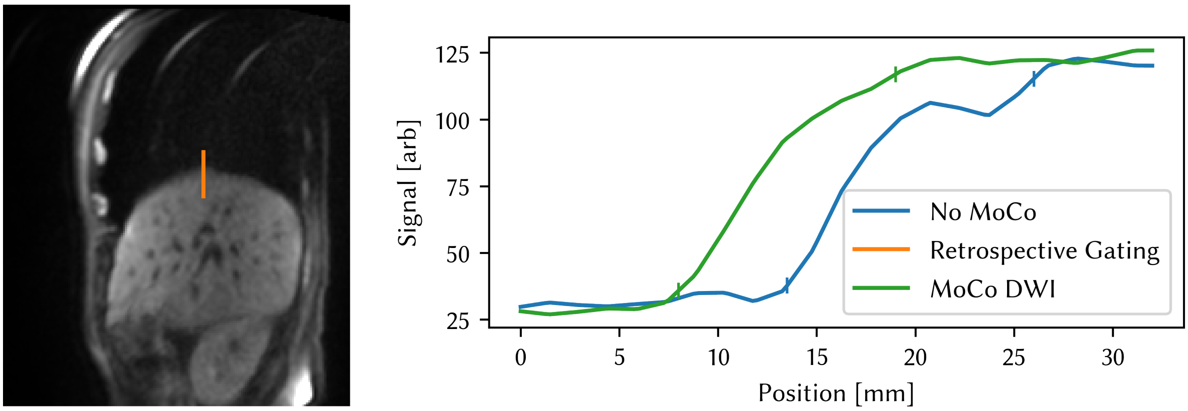

(c) $b = 800\,\mathrm{s/mm^2}$

Figure 4.8.: Representative line profiles of the liver-lung interface for different b-values and the post-processing algorithms. The images show the motion averaged slices which were used for positioning of the profiles. In all cases the MoCo DWI shows a sharper increase than the motion averaged (No MoCo) images, indicating an improved sharpness. The sharpest edge is observed in the retrospective gating (only in (a), due to gaps in the other retrospectively gated volumes).

(a) Liver-Lung Interface

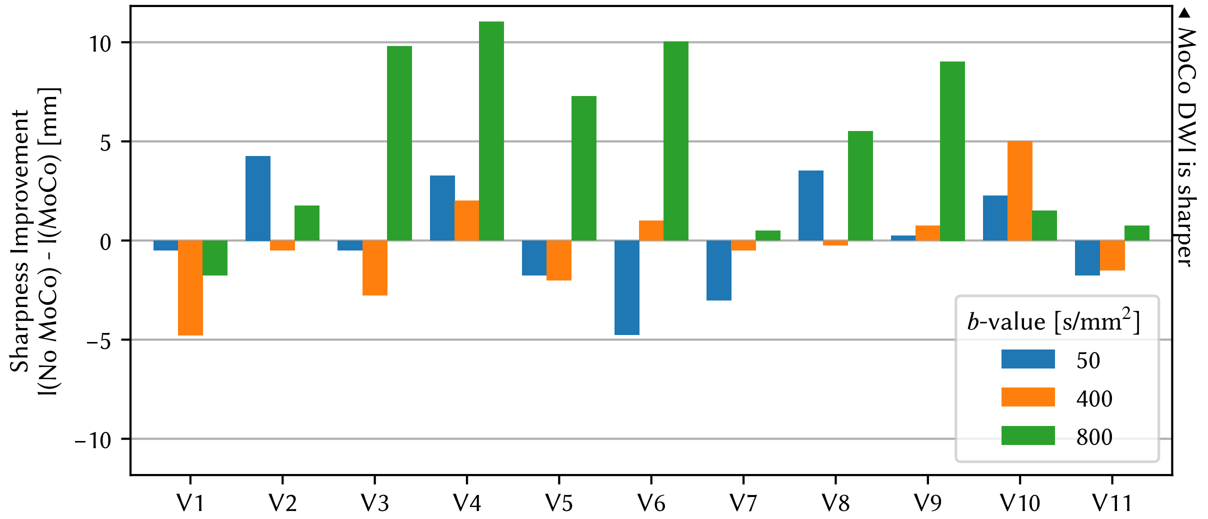

(b) Right Kidney's Tip

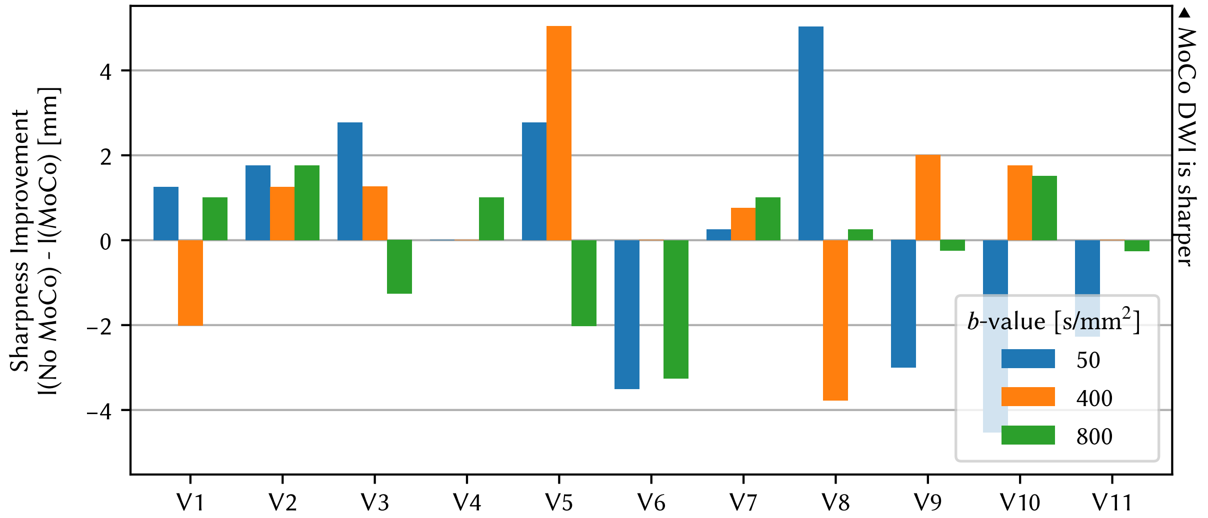

(c) Gallbladder-Liver Interface

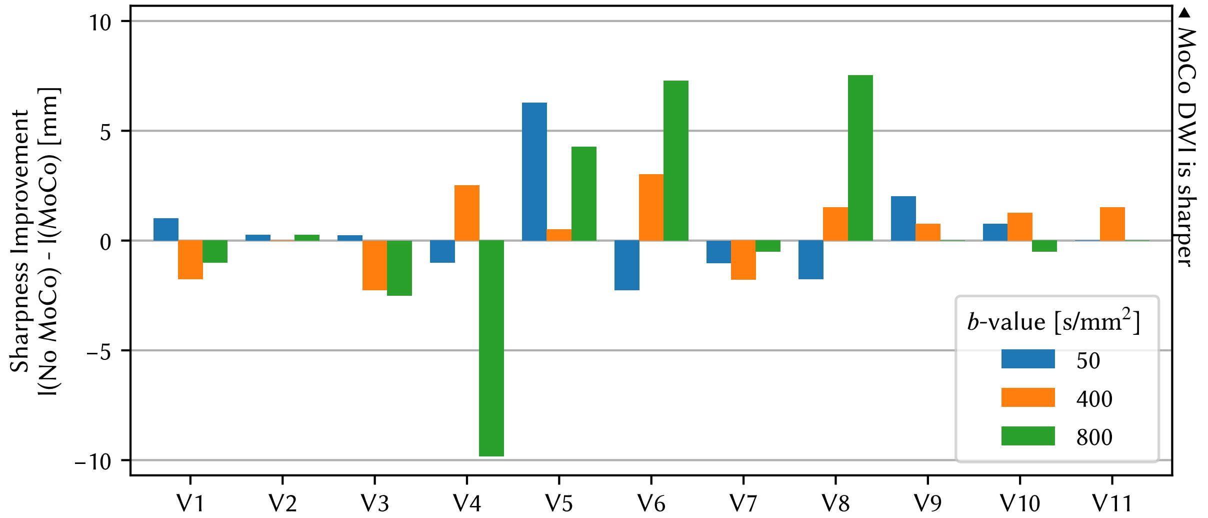

Figure 4.9.: Change of edge response (sharpness) by the use of motion-compensated diffusion-weighted imaging in different organs of 11 volunteers.

for No MoCo and MoCo DWI. The average in the retrospectively gated volumes was (15 493 ± 7359) voxels.

The median signal of the MoCo DWI was equal to the motion averaged DWI within the uncertainty. In 10 of 11 volunteers the noise measured as IQR as well as 1.5 × IQR was reduced by MoCo DWI (the outlier was volunteer 4). The retrospectively gated volumes showed increased noise in all used quantities, even though they could contain less voxels.

4.4.4. Sources of Errors

In the previous sections some volunteers have shown lower quality. This is analyzed in more detail in this section. The potential distortion between the GRE sequence for the motion estimation and DWI sequence was explained before and is thus not repeated here (Section 2.3.3).

Incorrect Gating

The decreased sharpness after the application of MoCo DWI in volunteer 1 can also be verified by the images themselves (Figure A.6a). Further investigations showed that the respiratory belt signal, which was used as basis for the gating, shows plateaus and only short breathing phases (Figure 4.11). Also several quick reflections were visible. Compared with the self-gating signal (where this was available) the breathing was also faster and remained in end-exhale and end-inhale phases longer (Figure A.6b). Correspondingly, the correlation coefficient between self-gating signal and cushion signal is as low as 0.68.

The retrospectively gated volume showed unexpected behavior (Figure 4.12). While between several motion phases nearly no motion of the liver or kidney was observable, another phase showed a deep inhaled motion state (Figure 4.12a). However, the same motion state was exhaled in the other b-values (Figure 4.12b).

Incorrect Motion Estimation

Another deterioration of sharpness was observed at the kidney’s tip in volunteer 10. In this case the joint-MoCo-HDTV showed a warping artifact in the kidney in the end-inhale respiratory motion phase (Figure 4.13). The classification as artifact was proofed by comparing with the previous motion phases and the retrospectively gated slice of the same phase. In these images the shape differed from the result presented by the joint-MoCo-HDTV. Furthermore was observed that the position of the artifact also the contrast in the retrospectively gated volume was low and impaired by streak artifacts, especially in motion phase 5.

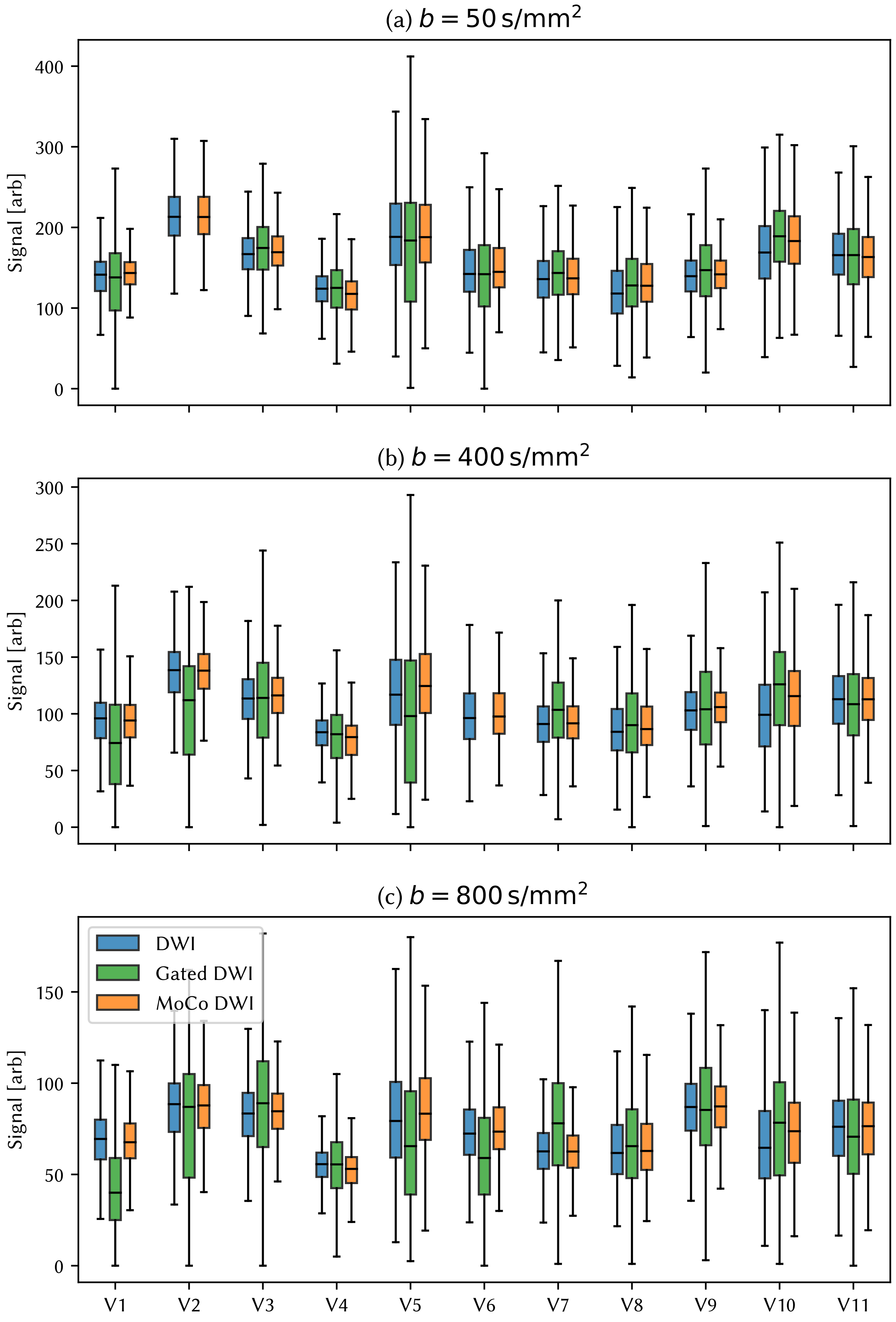

Figure 4.10.: Validation of signal and noise in the ROI of the upper liver. The median of DWI and MoCo DWI agree for all volunteers. The IQR and $1.5 \times$ IQR are lower in MoCo DWI in 10 of 11 volunteers.

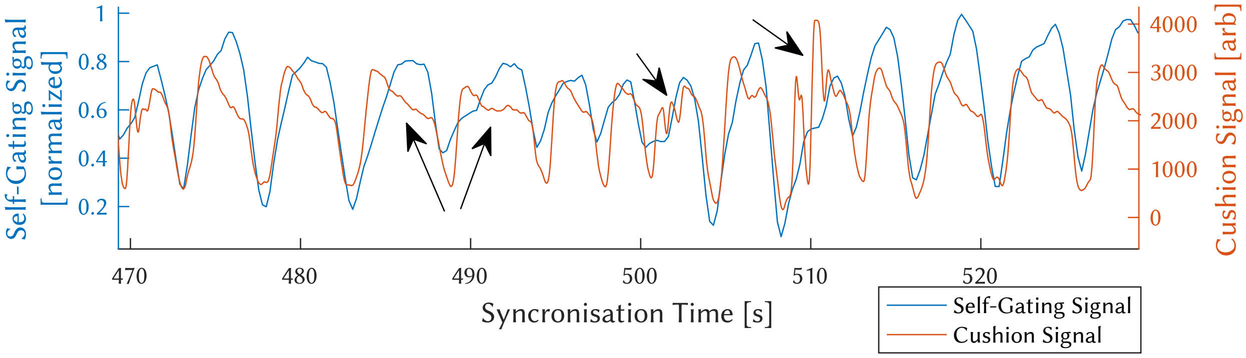

Figure 4.11.: Excerpt of the respiratory surrogate signals for V1. For comparison an interval was selected in which also the self-gating signal was available and can be used as ground truth. The cushion signal diverged from that self-gating signal, especially notable by the plateaus (left two arrows) and high frequency deviations (right two arrows). Both patterns repeated at different points in time.

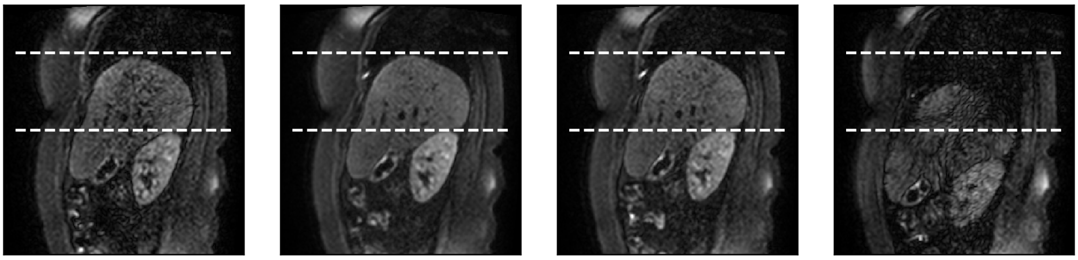

(a) $b = 400$ s/mm^2 for motion phases 1, 2, 3 and 9. The first three available motion phases for this slice show nearly no motion. However, the last one shows a significantly different, inhaled motion state.

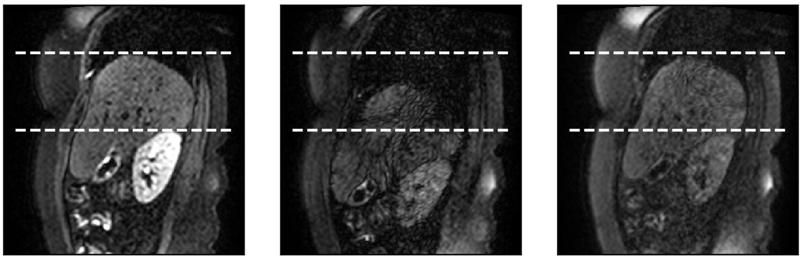

(b) Near end-exhale (Phase 9) for all b-values 50 s/mm^2, 400 s/mm^2 and 800 s/mm^2. Clearly visible is the different, inhaled, respiration state of the $b = 400$ s/mm^2 slice, even if the PMU suggest the same motion phase.

Figure 4.12.: Retrospectively gated volumes for V1 where MoCo DWI caused images with reduced sharpness.

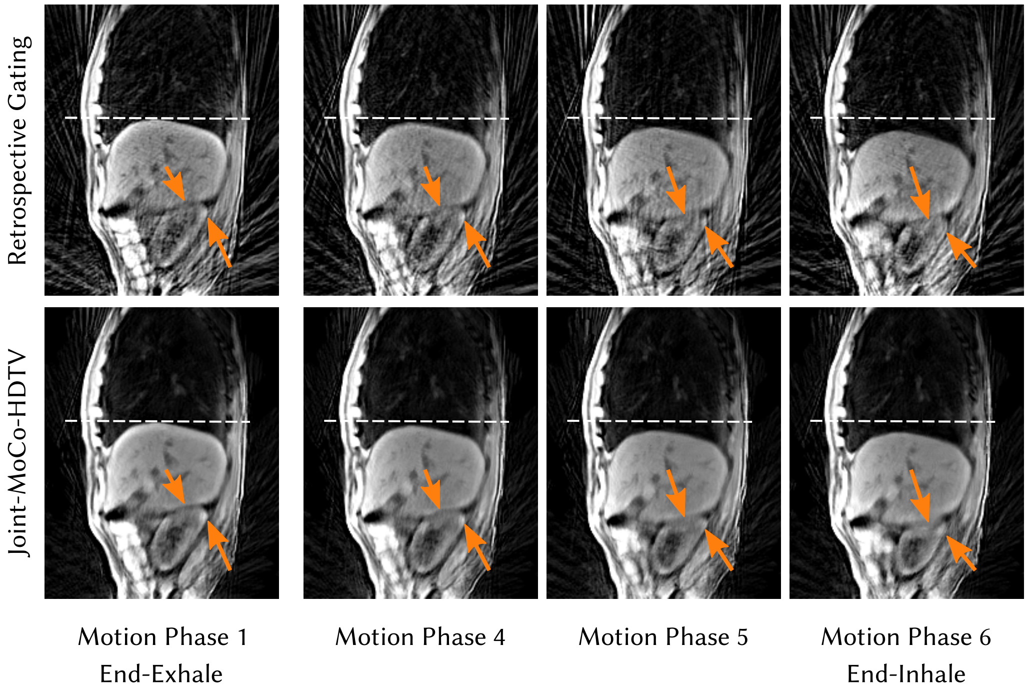

Figure 4.13.: Volunteer 10, joint-MoCo-HDTV reconstruction of the GRE sequence. In this case the right kidney was not plausibly deformed in the end-inhale phase (arrows). Also the shape does not fit to the retrospectively gated image. Most prominent is the blurring of the liver-kidney interface which is clearly visible in the motion phases 1 and 4. At the same position the retrospectively gated images (upper row) show low contrast and deterioration from (streak) artifacts. This indicates the streak artifacts may be the reason for the incorrect deformation.

4.4.5. Apparent Diffusion Coefficient (ADC)

The apparent diffusion coefficient (ADC) is an important tool for diagnostics and especially vulnerable to motion. In this study motion artifacts in the motion averaged ADC and Gaussian blurring ADC (Section 3.3.4) most prominently manifested as hypointense areas near edges (Figures 4.14a and 4.14b). It was possible to safely classify them as artifacts because the ADC in the liver and spleen are expected to be homogeneous in healthy volunteers. Also, the artifacts do not occur in all slices, especially not in neighboring slices. These artifacts are slightly reduced in Gaussian blurring ADC. With MoCo DWI, however, these artifacts are removed or clearly reduced.

The evaluation of the ADC in the ROI of the liver showed a reduction of noise, measured as decrease of IQR and 1.5×IQR (Figure 4.15). The median ADC values of Gaussian blurring ADC and MoCo DWI agree within the IQR of the ADC from the motion average reconstruction. A trend in a specific direction (increase or decrease) was not observed. In any case the ADC with prior Gaussian blurring showed less noise regarding both quantities and compared to both other post-processing algorithms.

In one volunteer (V9) negative values for ADC occurred. They were caused by insufficient coil normalization by the scanner causing high noise. This noise can lead to incorrectly low signal intensities in images of low b-values in some voxels.

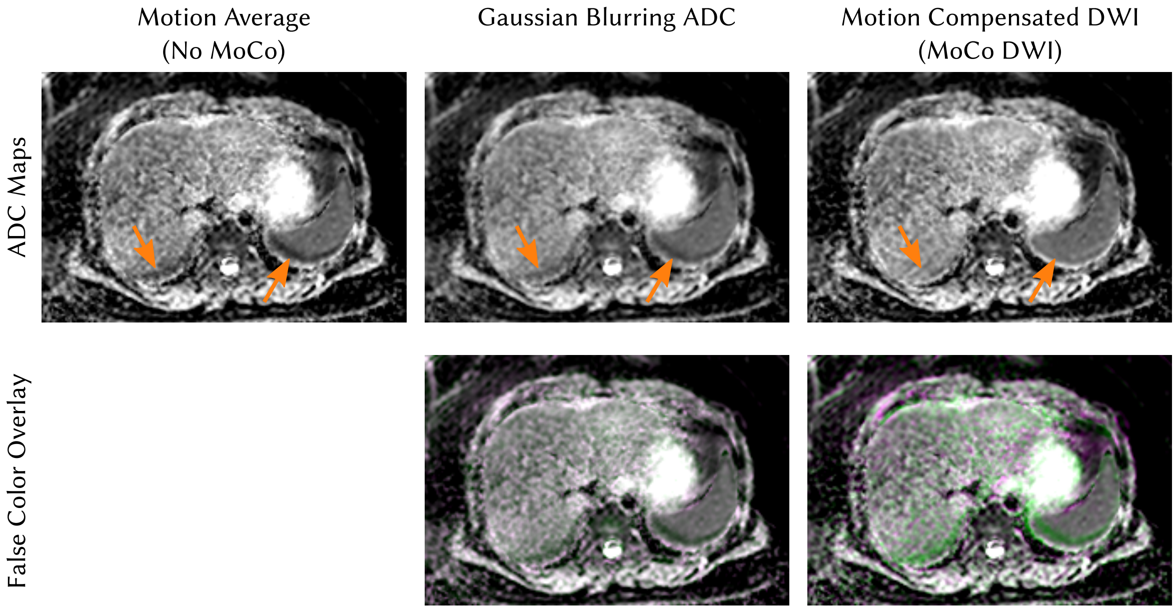

(a) Volunteer 8

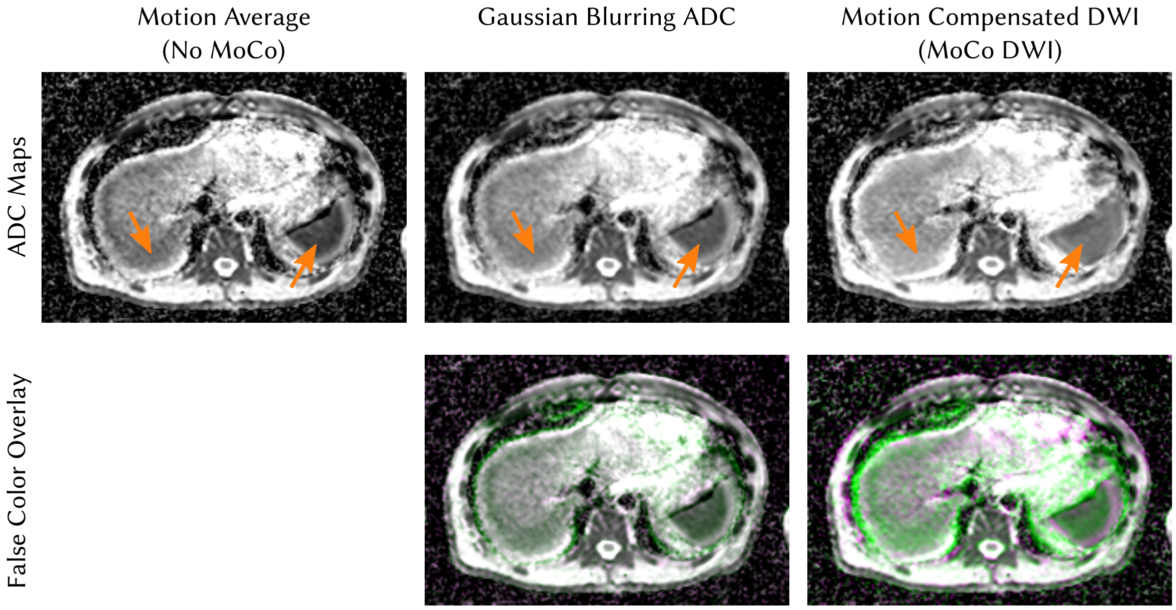

(b) Volunteer 10

Figure 4.14.: Comparison of the three algorithms motion average (No MoCo), Gaussian blurring ADC and MoCo DWI for the end-exhale phase in two volunteers, one slice each. The artifacts are visible as dark areas (arrows) in the No MoCo. These artifacts are also visible in the Gaussian blurring ADC to a smaller extend. Whereas they do not appear in the MoCo DWI images.

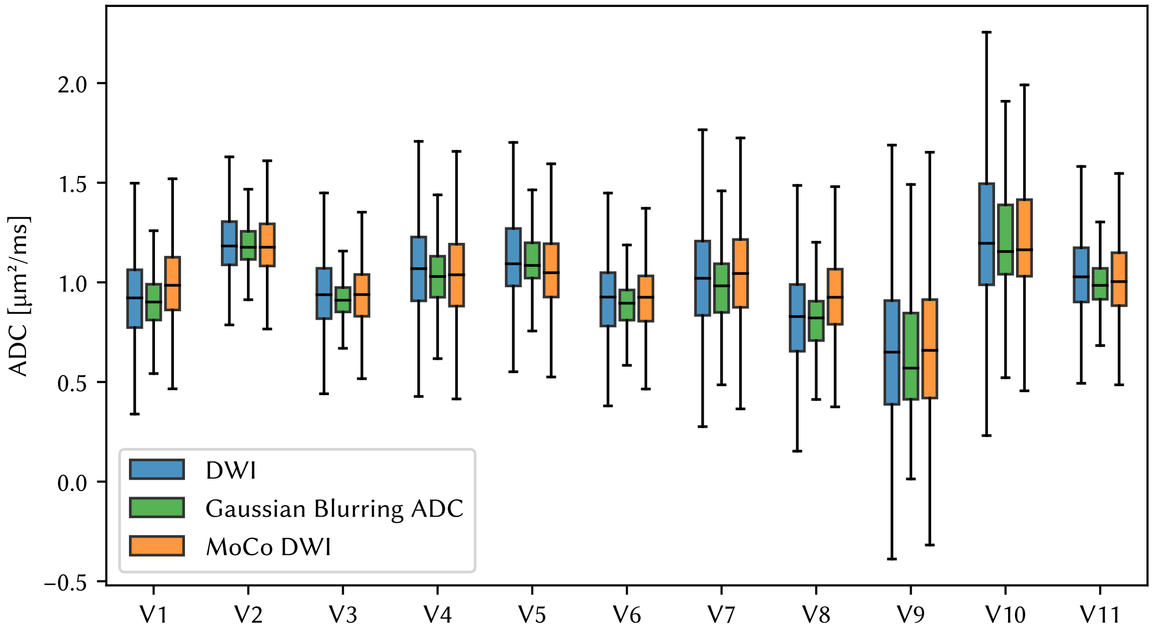

Figure 4.15.: Comparison of the ADC in the upper liver ROI for the three algorithms motion average (DWI), Gaussian blurring ADC and MoCo DWI. Within the errors, the ADC matches in all three post-processing algorithms. The noise (measured as IQR and 1.5×IQR) is lower in Gaussian blurring ADC and MoCo DWI compared to DWI. Notably the Gaussian blurring ADC shows even lower noise in the ROI than both other methods.

5. Discussion

In this chapter MoCo DWI is critically discussed. Not only to interpret the results but also to show potential limitations to improve the planning of potential, following clinical studies.

Therefore, this chapter is divided into five sections. The first two sections discuss the partially preexisting methods used for MoCo DWI. Section 5.3 discusses the results of the *in vivo* scans. This includes the discussion of the ADC-maps which is recommended as most important section in this chapter (Section 5.3.5). Section 5.4 puts MoCo DWI into the context of other DWI studies for respiratory motion control. Finally, this chapter ends with an outlook with recommendations for further development.

5.1. Joint-MoCo-HDTV as Source for Motion Vector Fields

The joint-MoCo-HDTV algorithm was used as source for the motion vector fields which were independent of the DWI measurement. As described, it was used in ten peer-reviewed publications before (Table 3.3). Thereof six used it for transferring motion information to other imaging techniques than MRI. This makes joint-MoCo-HDTV a recommendable choice to deliver the estimation of the respiratory motion in the form of motion vector fields for MoCo DWI.

Being a core part of MoCo DWI, joint-MoCo-HDTV is essential for the quality and accuracy of the motion-compensated diffusion-weighted-images. Thus, an additional discussion is required to asses potential errors and their influence on the reconstruction and post-processing. For a full discussion of this algorithm Rank (2016) and Appendix B are recommended.

A reduced motion in areas of low contrast was observed, while the same organ's upper and lower edges move more, especially in the liver. This was expected because the used Demons algorithm requires intensity changes for motion estimation. As a consequence it can be concluded that the motion estimation is not accurate in these areas.

Accordingly, it was observed that after applying the motion vector fields the motion was not fully removed. There are several reasons which can cause this underestimation. A potential cause are the application of the cyclic concatenated DVF, the cyclic constraint and the temporal total variation (HDTV). However, all are also used to reduce errors and hence cannot be eliminated.

The reconstruction duration of the joint-MoCo-HDTV, despite the significant improvements achieved in this work, are rather long with over 1 h. However, the used implementation is focused on research and thus not optimized.

Improving these concerns regarding the registration algorithm is beyond the scope of this work. The benefit of the joint-MoCo-HDTV — the use of the fully deformable (and thus non-rigid) Demons registration algorithm — persists. Also the GRE sequence could be acquired in optimal configuration for motion estimation (especially the high resolution in sagittal orientation and high temporal resolution). The described potential sources of errors anticipate a conservative estimation of motion. For this reason full compensation of motion is not expected. However, this full compensation is neither required nor possible, independent of the registration algorithm used. For this reason, the conclusion drawn from this study regarding MoCo DWI is not limited. Because the results of this work would be a lower border of possible improvements (assuming a better registration algorithm exists or will be developed).

5.2. Retrospective Gating for DWI

The retrospective gated DWI showed low SNR with increasing b-value and the volume is not fully sampled but contains gaps. Signal voids were frequently observed. Even though retrospective gating removed or reduced motion blurring compared to the motion averaged volumes, the low SNR (especially in acquisitions with b-values above 50 $\mathrm{s/mm^2}$) makes this method inconsiderable for diagnostic use. The SNR varied between (even neighboring) slices and motion phases is some cases. This SNR variation was caused by varying numbers of averages which were sorted into each motion phase. Even the volumes with low b-values — despite high SNR — are unsuitable for image registration due to the gaps.

This is even more considerable in the axial protocol, where the resolution in the main motion direction (cranial-caudal) is low compared with the respiratory motion amplitude. In this study the slice thickness was 5 mm with 1 mm spacing between them (inter-slice spacing). However, if the respiratory motion cannot be resolved, registration algorithms cannot detect that motion. An improvement by reducing the slice thickness is not expected because it would decrease the low SNR of the volumes furthermore.

The gaps themselves are inevitable because the slices with $b = 50\,\mathrm{s/mm^2}$ and $400\,\mathrm{s/mm^2}$

are acquired with 8 averages but gated into more, 10, motion phases. The numbers of motion phases could be reduced, but then an increase of motion blurring can be expected (Grimm et al. 2015). Also hysteresis effects were observed (in accordance with Deng et al. 2016). Thus, it is not simply possible to remove the distinction between inhaling and exhaling (halving the number of motion phases).

For this reason the drawbacks of retrospective gating are not solved yet (without extending the acquisition duration, cf. Section 5.4). Still, the retrospectively gated DWI is a good basis for further processing using MoCo DWI because all described problems do not influence the further processing.

5.3. Motion-Compensated Diffusion-Weighted Imaging (MoCo DWI)

5.3.1. General Remarks

Evaluating motion compensation algorithms is challenging, not only for DWI. Especially due to the lack of ground truth data. Therefore, this is an ongoing issue in the scientific community. Methods to gather a ground truth could be the use of phantoms. However, physical phantoms which offer ground truth data do not offer the same complexity of respiratory motion as *in vivo* studies. For instance phantoms are typically of low complexity, simulate unnatural motion and present sharp borders. This simplifies the situation for the registration algorithm artificially. The results gathered in this way do not allow to derive information for *in vivo* studies. Thus, natural, *in vivo* motion is preferable since the registration algorithm is a crucial part of MoCo DWI.

Alternatively, the ground truth could be generated by extending the measurement time until enough data is acquired to allow retrospective gating without reducing image quality. This time emerged to be unfeasible long. So, previous studies measured the same volunteer twice (with up to several days in between) to allow comparisons of ADC between the two examinations, assuming constant ADC over time. This assumption is of risk for neglecting other factors (e.g nutrition or natural variation) which may eclipse effects of the respiratory motion. For this reason, in this work, parts of the evaluation was done using a measurement with sagittal plane orientation.

The selection of volunteers is crucial for the results of *in vivo* studies. Admittedly, the cohort of healthy and experienced volunteers may show different abdominal motion than potential (nervous) patients. On the other hand the volunteers in this study were well spread in age and physique for a proof-of-concept study. Other studies with motion compensation were successfully performed with more homogeneous cohorts, smaller cohorts or did not contain information about the volunteer population (cf. Y. Liu et al. 2016; Nguyen et al. 2014; Ragheb et al. 2015; Sanz-Estébanez et al. 2018; van de Lindt et al. 2018).

5.3.2. Qualitative Observations, Sharpness and Noise

The sagittal plane orientation is not of interest in clinical use for abdominal imaging. However, they are well suited for quality control because the high resolution in the main motion direction (cranial-caudal) reduces partial volume effects. This is important because more precise analysis of the sharpness-improvement became possible. This, the sagittal acquisitions are used for quality control of MoCo DWI. For this purpose the volumes of each b-value are considered separately.

Qualitative observations show reduction of motion blurring compared to the motion averaged volumes. The upper edge of liver benefits most, because there the highest motion occurs. Changes in imaging of blood vessels caused by MoCo DWI are not easily evaluated. This is caused by the slice thickness of 5 mm, which is likely larger than typical vessels. So the vessels' orientation relative to the acquisition grid determine its sharpness — even if no motion occurs (Figure 5.1). Anyway, in some volunteers an improvement of small structures could be proofed. This is of high interest as they work as surrogates for structures of clinical relevance.

Many motion-averaged slices show low or even no motion blurring. In these cases MoCo DWI cannot provide a benefit if images of single b-values are accessed. This indicates that MoCo DWI is a technique to increase robustness of DWI measurements and prevent outliers.

This is also supported by the evaluation of the sharpness (measured via the edge response). An improvement for volunteers in general cannot be proofed with statistical significance. Nevertheless, this does not mean there is no effect (cf. Amrhein, Greenland, and McShane 2019). Quite the reverse is observable; the sharpness of the liver-lung interface and gall bladder-liver interface profit from MoCo DWI in some volunteers. Admittedly, in a clinical trail the number of test cases has to be increased for a reliable statistical analysis.

The mean values in the ROI did not show deviations between motion averaged volumes and MoCo DWI. Also, the noise (IQR and $1.5 \times \text{IQR}$) agrees in these two quantities with a small tendency for reduced noise in MoCo DWI. This demonstrates that MoCo DWI and its introduced weight factors (Equation (3.8)) fulfill their purpose. This is of special importance because these volumes are used to calculate the ADC-maps. A reduction of noise by MoCo DWI is expected because motion compensation algorithms have a tendency for intrinsic

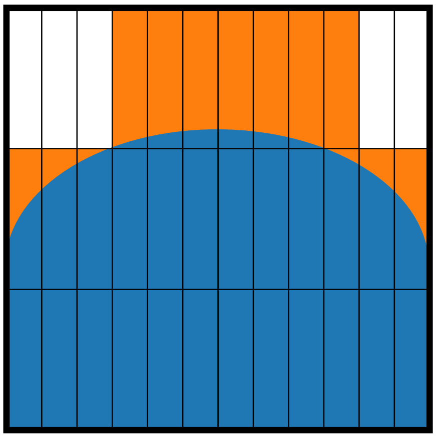

Figure 5.1.: Partial volume effects in volumes with anistotrop resolution. The exemplary object (blue) would be affected by partial volume effects in several voxels (orange). The low resolution in y-direction causes partial volume effects even in x-direction which has an higher resolution.

blurring which are caused by imperfect motion vector fields and the required interpolations during warping.

In this evaluation large ROIs with more than 11 000 voxels are used. The benefit is the reproducible and non-biased selection. The huge number of voxels ensures that small structures (e.g. blood vessels or lesions) do not influence the result inadequately. This robustness is furthermore supported by the use of IQR (or 1.5 × IQR) to compare noise. Other studies assume a specific noise distributions, typically a Rician distribution for the noise of magnitude images (Gudbjartsson and Patz 1995). Instead, these distributions are not applicable for MoCo DWI anymore because of the voxel and motion phase dependent weight factors used.

Transfer of DVF Between Modalities

MoCo DWI transfers the motion of one time frame — the GRE measurement — to another — the DWI measurement. Of course this requires an unchanged breathing pattern of the subject during this time period. This assumption is widely established and used in PET/MR (Section 2.7) and also in alternative methods to MoCo DWI (Section 5.4, cf. Chun et al. 2012; Dolde, Dávid, et al. 2019; Dolde et al. 2018; Grimm et al. 2015 and many others). The joint-MoCo-HDTV — which is used in this study — was successfully tested in a similar scenario by transferring the DVF to PET of the lung (Asif et al. 2013; Rank, Heußer, Wetscherek, et al. 2016).

As shown, the contrast in the T1-weighted GRE sequence which is used to generate the motion estimation, and the T2-weighted DWI sequence partially differ. Only the motion which is visible in the GRE can be well compensated[1]. As discussed before, the DWI measurement itself is not suitable for motion estimation due to several reasons. Moreover, the split allows to optimize the GRE sequence for motion estimation. For example shorter repetition time and the radial k-space readout are thus possible.

In any case perfect DVFs are not even required, because any estimation that is better than ignoring motion at all, will improve the images. In Section 5.5 methods to further improve the DVFs and the transfer to DWI are suggested.

5.3.3. Sources of Errors

This study revealed that not all images acquired with volunteers were improved by MoCo DWI. Here the respiratory cushion (PMU) presented itself as a possible point of failure. In Section 5.5 methods are presented to eliminate these errors. A benefit of the respiratory belt is its wide availability and it is well tolerated (even by childern, cf. Caldiroli and Minati 2007).

A major issues is that PMU signal did not represent the volunteers' respiratory motion in all cases. Logical the retrospectively gated volumes were corrupted and showed motion blurring. Unavoidably this blurring persists in the following processing steps of MoCo DWI and hence lead to deteriorated images. The reasons are diverse. Possible causes are non optimal positioning of the cushion, variation of the breathing pattern after positioning — e.g. due to relaxing or stress of the volunteer. This change may lead to over- or underflow of the measurement scale of the ADC for the PMU. Also displacement of the cushion, the belonging belt or the weighting receive coil can cause corruption of the belt signal.

Outliers which may be caused by coughing can only cause effects in isolated slices. The PMU signal would be deteriorated at these time points. Nevertheless, the signal should normalize quickly (if the cough did not cause a displacement of the cushion). The used normalization is designed to be robust against such outliers. Hence, they do not affect the signal in general.

Another potential issue is the already described distortion between EPI (used for DWI) and GRE sequences. In this study the generalized autocalibrating partially parallel acquisition factor was increased from the common value of 2 to 3. This allowed faster image acquisition which reduced the EPI distortion. Also, vendor-provided distortion correction was used. Despite these improvements, remaining distortion was proven in this study. Alternatively the use of a separate EPI sequence optimized for motion estimation could be considered to acquire the volume with similar distortion. This requires a different k-space acquisition (e.g.

---

[1] Due the algorithm used in this work, the motion has to be visible in the magnitude images of the GRE.

stack-of-stars as in the GRE) to prevent the discussed holes. This suggests different distortion as in the dw EPI.

The distortion due to the EPI sequence occurs in phase-encoding direction. But, for the clinical, axial protocol the respiratory motion (and the resolution of the DVF) in that direction is low. Thus, displacement by distortion is inherently reduced in this case.

5.3.4. MoCo DWI Algorithm

The used method of averaging in the retrospectively gated volumes and the recombination of the motion phases after motion compensation changes the weighting of the acquired voxel. For motion averaged images the weight of each acquired voxel influences the final voxel by $^{1}/_{\#\text{avg}}$ (#acq number of averages for the considered b-value). Thus, if one slice is impaired by artifacts — for example signal voids — its effect in the final image is lower than $^{1}/_{\#\text{avg}}$.

This is different in MoCo DWI. Due to the averaging in the retrospectively gated volumes several slices can be combined. Afterwards, MoCo DWI combines these motion phases again with a voxel and motion phase dependent weighting factor $\mathbf{w}$ (Equation (3.8)). This is necessary to ensure consistent intensity values which are essential for ADC calculation. However, this factor is independent of the number of slices averaged in the retrospectively gated volume. For this reason in MoCo DWI each measured voxel is weighted differently in the final volume. Instead, motion phases are weighted similarly. Deviations from equal weighting of motion phases are possible due to holes and warping. As a result an artifact occurring in one slice before recombination, may be (randomly) increased or weakened.

Nevertheless, this behavior of the algorithm is beneficially. Volunteers in supine position stay longer in end-exhale phase than other motion phases. Thus, end-exhale motion phases are weighted higher if all slices are weighted equally. As a result, motion blurring can apparently be reduced (this effect was also observed in context of Dávid, Behl, et al. 2019). This risks that not the motion compensation is evaluated but the breathing pattern. Therefore, this effect has to be reduced, to test if the motion compensation by transferring the DVF is the improving effect. Given the above, the used, equal weight of motion phases is beneficial for the evaluation of MoCo DWI. This is not required in clinical use where equal weighting of each slice is favorable to prevent over-weighted influence of artifacts (as signal voids).

5.3.5. Apparent Diffusion Coefficient (ADC)

Without motion compensation the ADC maps showed artifacts in several slices. They manifested most prominent in the form of areas with reduced ADC along edges in cranial-caudal direction. MoCo DWI, instead, could remove or reduce these artifacts.

Generally motion compensation can cause intrinsic blurring. To prove that the observed artifact reduction is caused by the motion compensation and not by this blurring, a test with the Gaussian blurred ADC was performed. In the results the artifacts were indeed reduced by Gaussian blurring ADC compared with motion average volumes. Nonetheless, they are not reduced/removed as clearly as in MoCo DWI. On the other hand, the noise was reduced significantly compared to the ADC gained from motion averaged DWI and MoCo DWI. This suggests that the blurring effect of the Gaussian blurring ADC is higher than any potential blurring caused by MoCo DWI. To summarize, Gaussian blurring ADC shows more artifacts and higher blurring at the same time. This suggests that the artifact reducing effect of MoCo DWI is caused by the motion compensation — and not any concomitant blurring effect.

The results also show that the respiratory motion causes artifacts especially in the derived quantity ADC, which is congruent with Ragheb et al. (2015). For this reason the main benefit of MoCo DWI is the increased reproducibility of the respiratory motion states between b-values. It is most likely that the desirable benefits of MoCo DWI can be transferred to other derived quantities like kurtosis or even diffusion tensor imaging.

5.4. Comparison to Existing Methods

Several methods to reduce respiratory-motion induced artifacts were suggested before (Section 3.2.5). In this chapter MoCo DWI is compared with these methods. Different features of the methods are briefly compared in Table 5.1.

5.4.1. Prospective Methods

Breath-hold, a clinical technique, offers less configuration options than MoCo DWI, making MoCo DWI beneficial. Also the patient comfort is increased in MoCo DWI because the breath-hold is completely omitted. The limited configuration options are caused by the length and number of repetitions of breath-holds per patient (if possible at all). Shenoy-Bhangle et al. (2017) recommend 40 s to 60 s with two breath-holds, Chandarana and Taouli (2010) recommend acquisitions quicker than 23 s with a single breath-hold (similarly Schmid-Tannwald et al. 2013). Also patients fatigue in their capability to hold their breath (Jahnke et al. 2006). This requires to reduce the measurement time, by using fewer slices, b-values or repetitions than possible in MoCo DWI (or some of the other methods described in this chapter).

Thus, the current gold-standard, including clinical diagnosis, to compare to are the motion average (No MoCo) and triggered sequences (Chandarana and Taouli 2010). In this work was shown that motion averaging can lead to motion induced artifacts. Therefore, MoCo DWI is superior because it reduces or removes these artifacts. The advantage of motion averaging on the other hand are its low complexity during measurement as well as reconstruction. Also, the additional GRE for motion estimation is not required. However, if the artifacts impair the diagnostic value of the images, a second scan might be required. In these cases MoCo DWI saves time despite the GRE sequence.

Beneficial is the possibility to combine motion averaged imaging with MoCo DWI. The measurement sequences are equal, only the reconstruction differs. Thus, a physician can use both reconstructions without additional measurements.

Similarly to motion averaging, triggered methods (including semi-triggered methods like Y. Liu et al. 2017) require only limited patient support; shallow breathing. An improvement of SNR and contrast-to-noise ratio compared to motion averaging was shown in previous studies (Kandpal et al. 2009). However, the measurement time increased at least 2.5-fold (Taouli et al. 2009), or more (Shenoy-Bhangle et al. 2017). MoCo DWI also increased the measurement time by adding the GRE sequence, but only by a factor of 2.

In the context of PET/MR measurements, the GRE sequence is even commonly used anyway. Thus, in this context, the required measurement time is comparable to motion averaging. Furthermore, the measurement time of less than 5 min is only used to be comparable to current clinical PET/MR protocols. Rank, Heußer, Wetscherek, et al. (2016) have shown that — at least in the lungs — even measurement times as short as 1 min are sufficient to estimate the motion vector fields. To summarize, the added measurement time for the GRE sequence is of minor concern in many cases.

5.4.2. Retrospective Methods

Several other retrospective methods for motion compensation in DWI were recently proposed (cf. Section 3.2.5). MoCo DWI is outstanding from them due to the used, fully-deformable registration — the demons algorithm. Additionally, the image registration is also independent from the image quality of the DWI.

Thus it is possible to use clinically accepted and wide spread dw EPI sequences. Also for that reason, low SNR and artifacts which occur often in DWI, or the underling EPI sequence, do not affect the motion estimation. Furthermore, the (cylic) image registration profits from spatial and temporal resolution of the GRE sequence which is high in the main motion direction compared to the DWI. The disadvantage of this two-sequence approach are the possible, differences in distortion and contrast as well as potentially longer measurement times (cf. Section 5.4.1).

Method	Free Breathing	Allows 4D DWI	Defined respiratory motion phase	Assumes cyclic motion	Registration algorithm	Utilizes whole measurement time
Motion average (No MoCo)	~	✗	✗	✗	✗	✓
Breath-hold	✗	✗	✓	✗	✗	✗
Prospective triggering	~	✗	✓	✗	✗	✗
Y. Liu et al. (2017)	✓	✓	~	✓	✗	✗
van de Lindt et al. (2018)	✓	✓	~	✓	✗	✗
Mazaheri et al. (2012)	✓	✗	✗	✓	r	✓
Ragheb et al. (2015)	✓	✗	✗	✓	r	~
Guyader et al. (2015)	✓	✗	~	✗	b	✓
Sanz-Estébanez et al. (2018)	✓	✗	✗	✗	b	✓
MoCo DWI	✓	✓	✓	✓	d	✓

Table 5.1.: Comparison of features offered by several motion compensation algorithms for DWI. (✓: yes, ✗: no, ~: limited, r: rigid motion, b: b-spline registration, d: demons algorithm)

MoCo DWI is the only motion compensation algorithm with non-rigid registration which allows to select a predefined target motion phase. Thus an extension to 4D DWI is possible, as done by Y. Liu et al. (2017). This is not possible with Guyader et al. (2015) due to the used groupwise registration and also not by Sanz-Estébanez et al. (2018) which has no possibility to select a meaningful target phase.

Alternative motion compensation algorithms use (semi-)rigid registration (Mazaheri et al. 2012; Ragheb et al. 2015) or a b-spline based MoCo with few control points in the main motion direction (Guyader et al. 2015; Sanz-Estébanez et al. 2018). However, it was shown that the liver is compressed by respiration (Blackall et al. 2001; Hu et al. 2017; Rohlfing et al. 2001, 2004). Thus, rigid registration is not able to compensate the motion correctly. It is also questionable if a b-spline interpolation with only three control points, as in the previous studies, is able to do so. On the other hand, the few control points ensure motion even in areas of low contrast. To answer this further studies are required which compare the algorithms using images which show (pathological) symptoms.

5.5. Outlook

Further development should target to reduce the sources of errors described before (Section 5.3.3), to enable MoCo DWI for a wider range of patients. Benefit could be achieved by more robust detection of respiratory motion phases during the DWI sequence. Several respiratory motion estimation methods for scientific purposes were suggested (cf. Fahmi, Simonis, and Abayazid 2018). Küstner et al. (2017) proposed the integration of the electrocardiogram signal for improved detection of respiratory motion. In van de Lindt et al. (2018) an image-based self-sorting signal was proposed. However, it is unclear to the author how this self-sorting signal should work in the presence of signal voids and high b-values.

Of special interest is the pilot ton (Vahle et al. 2020). This technique uses an additional radio frequency signal which is detected by the default receive coils during the measurement. By transversing the breathing patient, the originally constant radio frequency is altered. From these changes a respiratory signal similar to the self-gating signal (Section 2.5.2) can be deduced.

Another improvement of the retrospectively gated DWI could be achieved by the detection of outliers (e.g. ones caused by coughing). This would reduce SNR in favor of reduced motion blurring.

Distortion and signal voids are common and known issues in DWI. An advantage of MoCo DWI is that the motion estimation is independent from these artifacts. This allows to use previously developed correction methods for both artifact types. The detection of signal voids could be done before recombination (eg. Chang, Jones, and Pierpaoli 2005). For distortion detection, image based corrections are promising (Holland, Kuperman, and Dale 2010; Nketiah et al. 2018; Treiber et al. 2016).

Also in addition to using the estimated motion vector fields from the GRE-sequence, the gated DWI could be used for further improvements. Here previously presented methods are possible (e.g. Guyader et al. 2015; Sanz-Estébanez et al. 2018). This can also mitigate the distortion effect between dw EPI and the GRE sequences. At the same time the improved resolution of the GRE sequence is utilized.

In this work an improved image quality due to MoCo DWI was shown for several volunteers. However, from a clinical point of view the improvement of the diagnostic value is of interest. This means that the improved image quality also translates into more diagnostic insight. For this clinical studies with a significantly increased number of cases and with real pathological changes are required.

6. Conclusion

Respiratory motion was identified as a main source of artifacts for DWI before. This leads potentially to measurements with reduced or insufficient diagnostic value. Thus, even repetitions of patient measurements can be necessary.

In this proof-of-concept study a newly developed method to remove respiration-induced motion blurring in DWI was presented and successfully validated: MoCo DWI. MoCo DWI is the first method to allow fully deformable motion compensation for DWI. To achieve this, two MR sequences were used consecutively; a golden-angle, stack-of-stars GRE sequence for the motion estimation and the DWI. The GRE sequence was configured for optimal motion estimation regarding spatial and temporal resolution. The DWI on the other hand was used in a configuration of clinical interest — independently configured from motion compensation requirements or the GRE sequence. Thus, the DWI sequence can be used without MoCo DWI but with common reconstruction techniques instead.

The method was tested with eleven healthy volunteers, each with two different protocols (33 years to 79 years, body mass index 19 $\mathrm{kg/m^2}$ to 34 $\mathrm{kg/m^2}$, 5 female). In test measurements of high resolution in cranial-caudal direction (saggital protocol) MoCo DWI could successfully reduce motion blurring in 6 of 11 volunteers (liver-lung interface, 3 showed no significant changes). In the clinically-oriented, axial configurations, motion blurring was only significant in some cases, even without motion compensation. However, without motion compensation clear artifacts could be observed in several ADC-maps. With MoCo DWI is was possible to reduce or even remove these motion-induced artifacts. Here was also assured, that this desired effect was caused by the motion compensation and not by the unavoidable blurring accompanied by this motion compensation.

After all, this is the first proof-of-concept study. Regarding the volunteers where no improvement could be achieved, several sources of issues were identified; insufficient detection of respiration phases by the cushion-based PMU, distortion and limits in the estimation of motion vector fields. It was also observed that in many cases the (common) averaging and coarse resolution in the axial protocol reduced the perceptible respiration-induced motion blurring in many cases. Here MoCo DWI is beneficial because no change of the DWI sequence is required which allows to use both techniques without repeated measurements.

Thus, the reconstruction technique for diagnosis can be selected after the measurement. MoCo DWI allows flexible configuration of the DWI sequence. This potentially allows to combine MoCo DWI with other available correction methods to overcome these issues.

The expected advantage of MoCo DWI are more robust measurements in regards to respiration-induced blurring artifacts. At the same time patient comfort is high because no breath-holds are required. Also the measurement time is not increased as long as in triggered measurements. In PET/MR the GRE measurement for motion compensation is common anyway thus the measurement time is not even changed here.

These advantages are expected to reduce the number of measurements of insufficient diagnostic value and thus less repetitions of (costly) measurements. Especially the calculation of ADC-maps (and thus potentially further derived quantities, eg. kurtosis or IVIM) benefit from MoCo DWI.

A. Additional Images

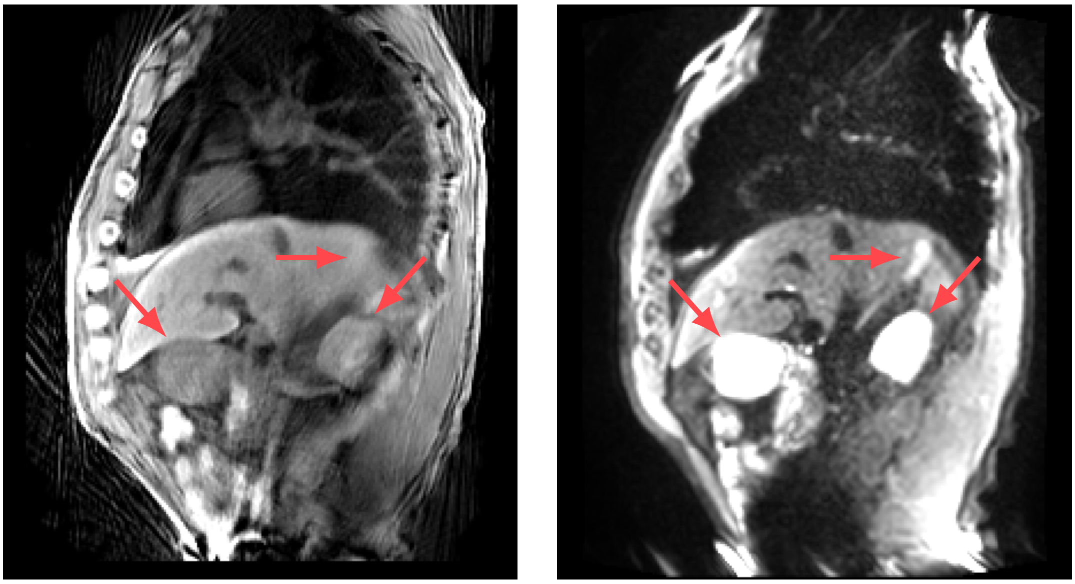

(a) T1-weighted gradient echo sequence (GRE)

(b) T2-weighted diffusion-weighted imaging (DWI) ($b = 50\ \mathrm{s/mm^2}$)

Figure A.1.: Example for contrast differences between (a) T_1 and (b) T_2 weighted images of a volunteer with comparable spatial resolution. The EPI-sequence used for DWI is inherently T_2-weighted, while the GRE sequence used in this study is T_1 weighted for fastest image acquisition. This leads to different contrasts. Most notable is that in T_1 images the kidneys have similar intensities as the liver while they appear hyperintense in the T_2 images (right arrow). Other structures may show improved contrast changes to surrounding tissue in one of the volumes (middle arrow). This is important while transferring the DVF as the motion detection works best at contrast changes.

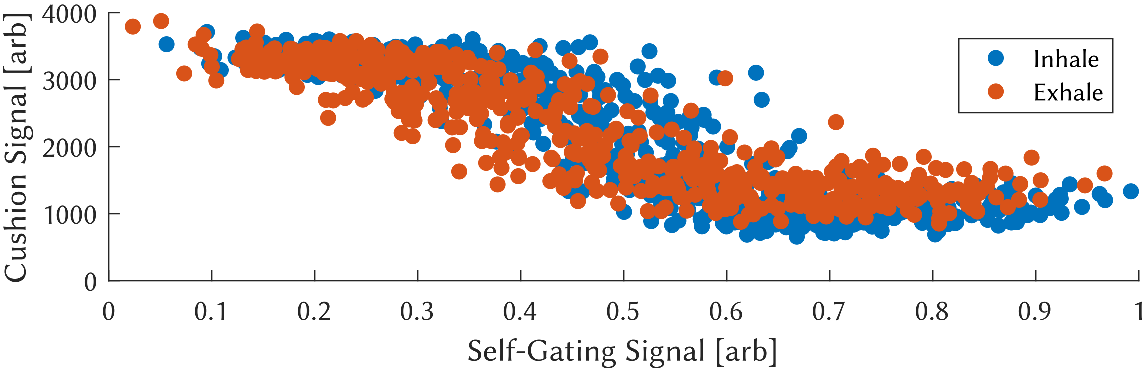

Figure A.2.: Example for hysteresis curve between the self-gating and cushion signal during the GRE sequence. Consequently the distinction between inhale and exhale is used for motion estimation.

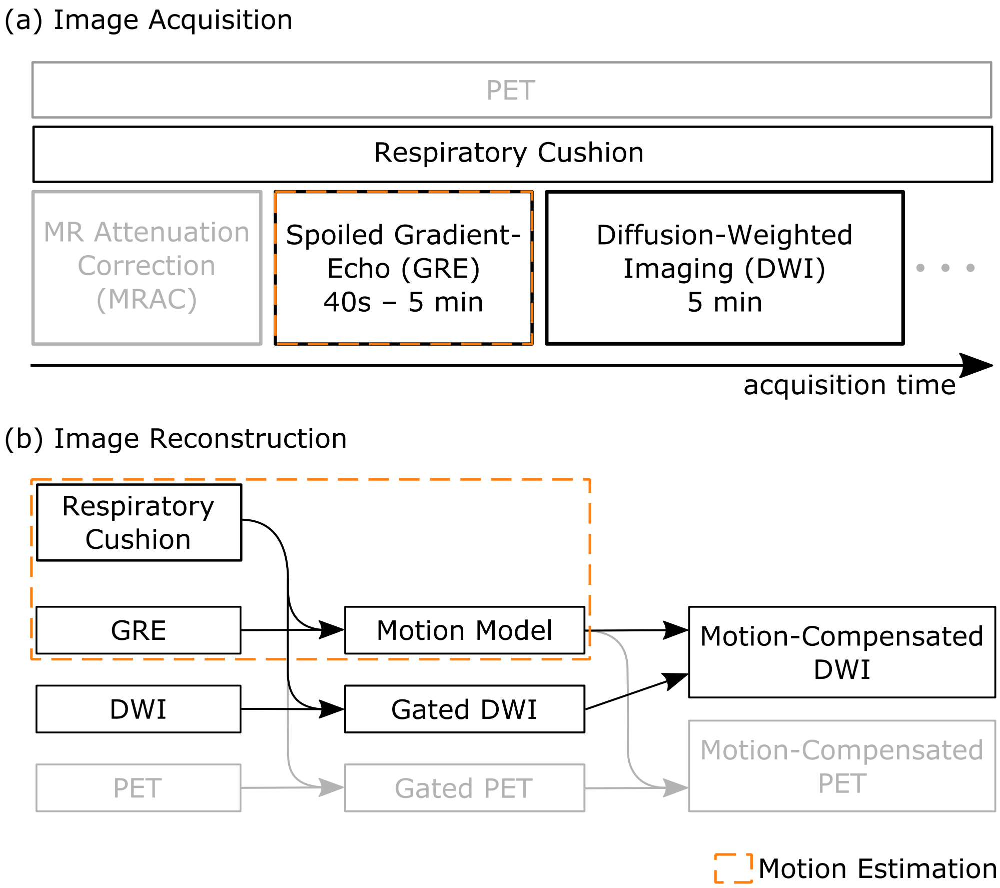

Figure A.3.: Scheme of the MoCo DWI workflow extended to PET/MR measurements with motion compensated PET imaging (grey). The motion estimation (dashed orange) is not only used for the motion-compensated DWI but also motion-compensated PET reconstructions. In both cases the GRE images with high quality are used to estimate the respiratory motion. This workflow is important because the GRE for motion estimation and DWI are common in PET/MR studies.

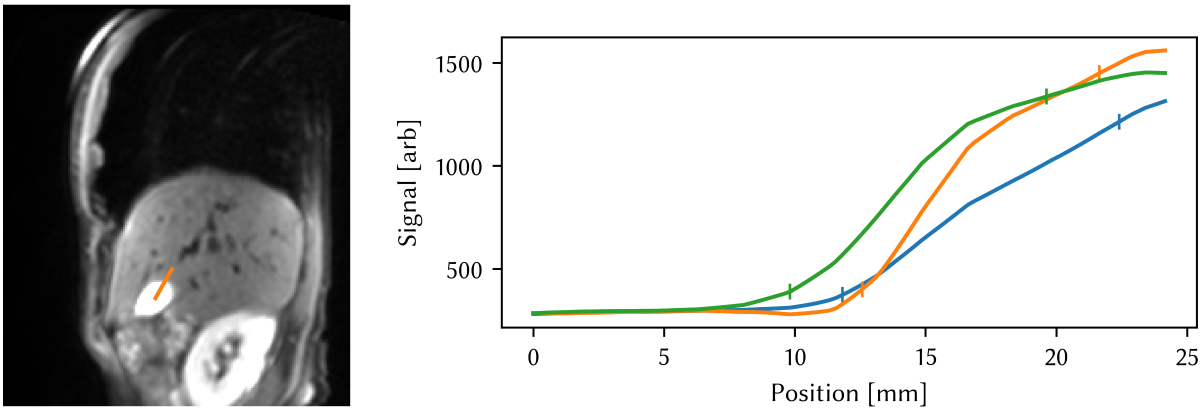

(a) $b = 50\,\mathrm{s/mm^2}$

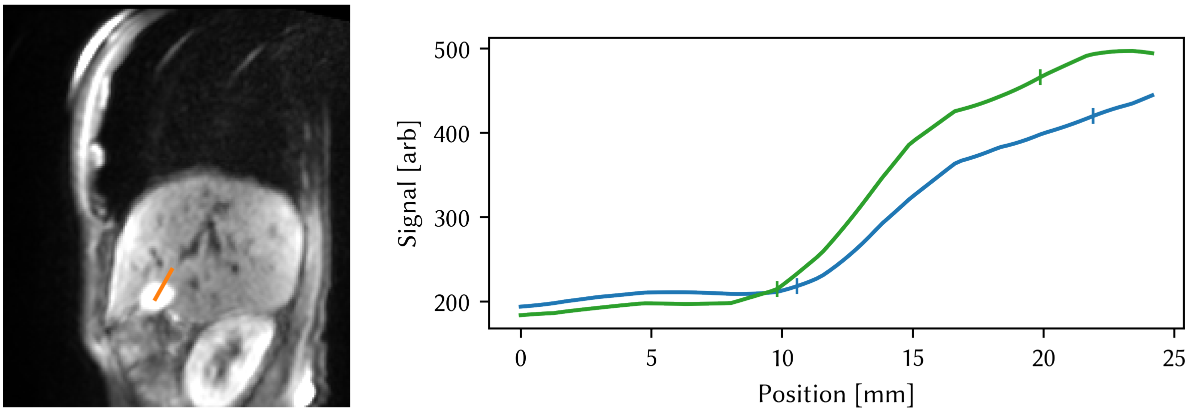

(b) $b = 400\,\mathrm{s/mm^2}$

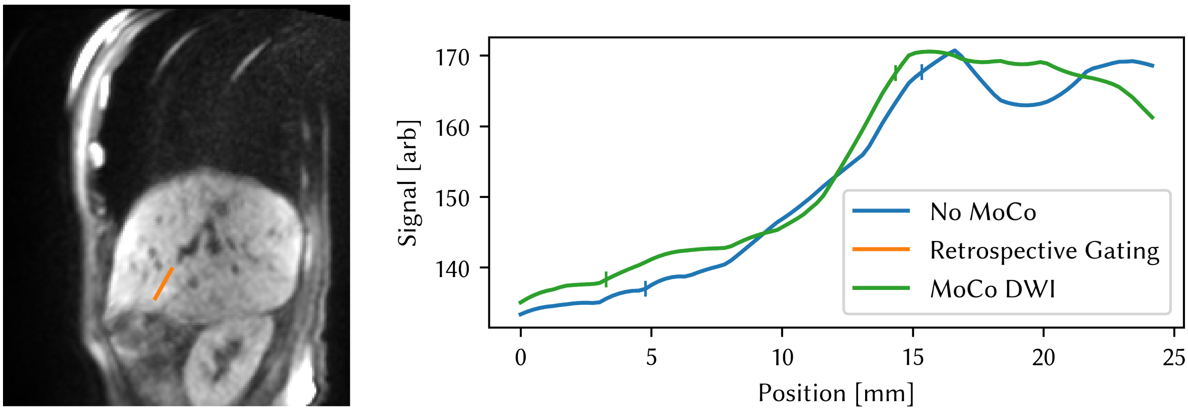

(c) $b = 800\,\mathrm{s/mm^2}$

Figure A.4.: Representative line profiles of the interface between gall bladder and liver in volunteer V10. The marker show the border used to determine the edge's length (10 % to 90 % of the intensity).

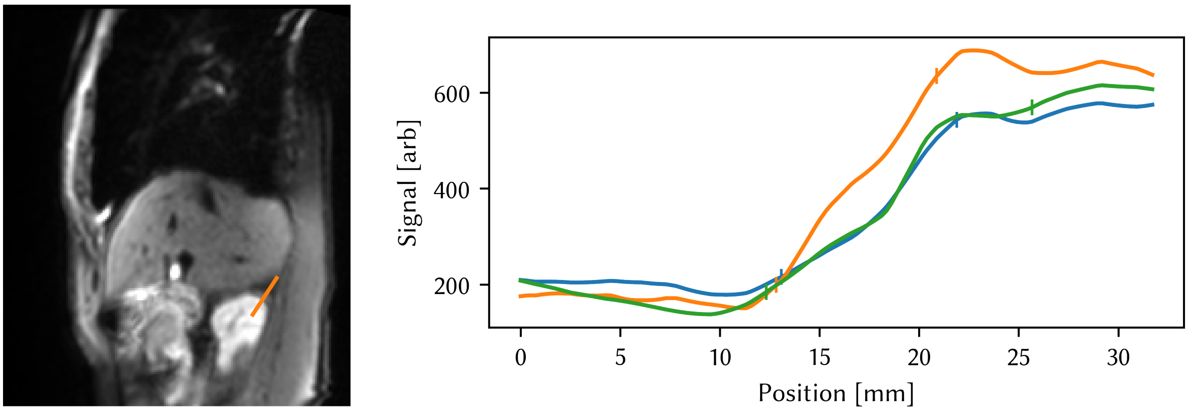

(a) $b = 50\ \mathrm{s/mm^2}$

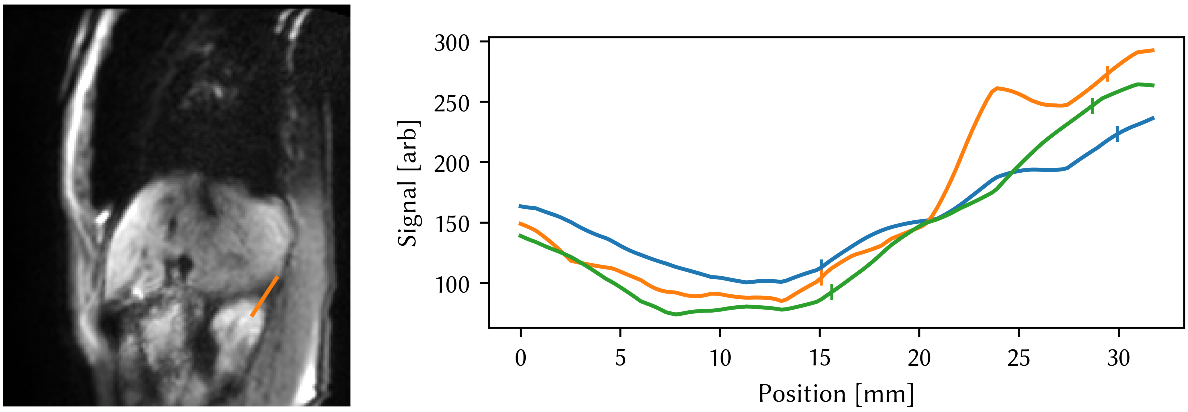

(b) $b = 400\ \mathrm{s/mm^2}$

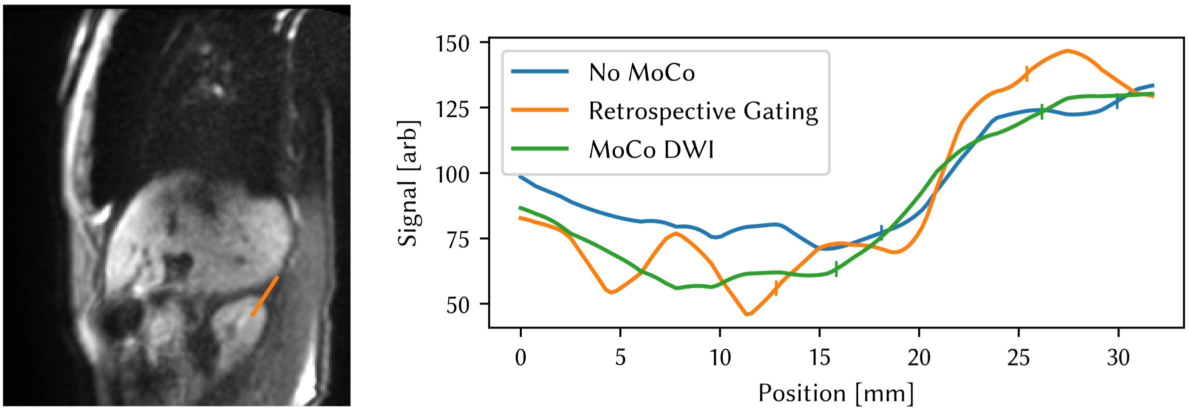

(c) $b = 800\ \mathrm{s/mm^2}$

Figure A.5.: Representative line profiles of the right kidney's tip in volunteer V10. The marker show the border used to determine the edge's length (10 % to 90 % of the intensity).

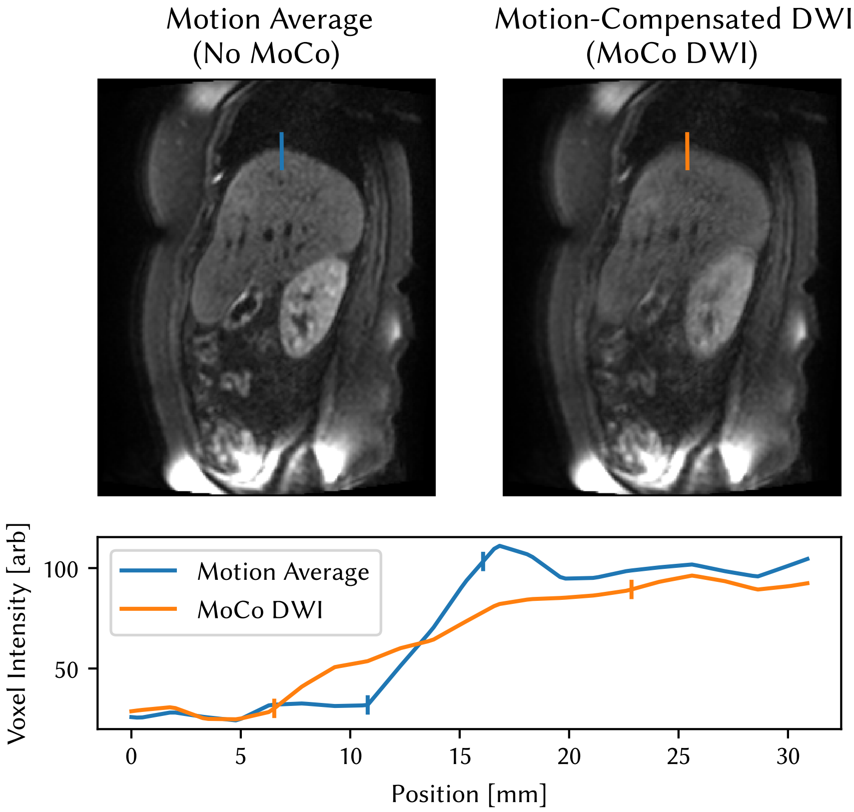

(a) Exemplary slice used to determine the line profile where MoCo DWI caused an deterioration of the image quality.

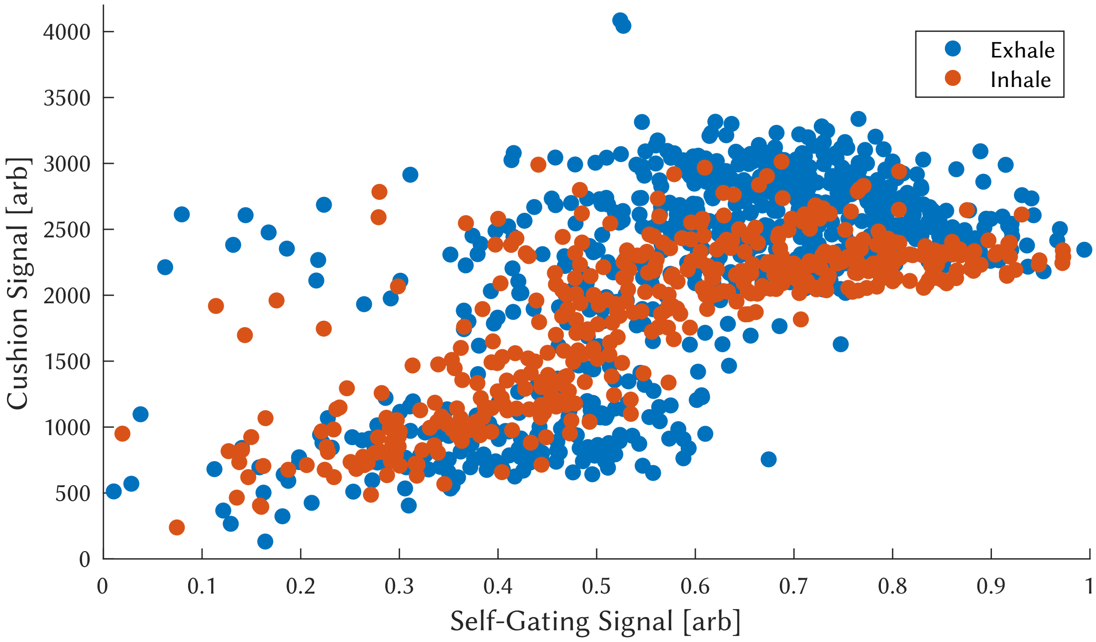

(b) Scatter plot of self-gating signal and the cushion signal during the GRE sequence. In an optimal signal a linar correlation between both signals is expected. In contrast to that, two flat plateaus connected by steep increase are present. Several outliers are observable.

Figure A.6.: Volunteer V1 in which the sharpness in MoCo DWI is reduced due to incorrect retrospective gating with the cushion signal.

B. Discussion of Joint-MoCo-HDTV

In this chapter several aspects of the joint-MoCo-HDTV algorithm are discussed. They are based on the experience gained during this work but not essential part of MoCo DWI. As described before the change of the registration algorithm to estimate the motion is beyond the scope of this work and also ineffective for evaluation of MoCo DWI.

The DVFs estimated using joint-MoCo-HDTV show reduced motion inside the organs, especially the liver (Section 5.1). Three reasons for this effect were observed during this study: the cylic registration, the cyclic constraint and the use of the HDTV regularization in phases of low resolution.

The cyclic registration is of benefit to prevent incorrect motion estimation. Because the registration algorithm has to estimate small displacements only, misinterpretation is less likely and promises improved robustness (small motion assumption, Brehm et al. 2012). However, the warping of motion phases which are not neighbors but further apart, require (multiple) concatenation of these estimations which accumulates errors. In the setting of motion which has a magnitude in the order of the image resolution it is questionable which of the two described effects has higher influence on the correctness of the DVF.

A benefit of the cyclic registration is the ability to use the cyclic constraint. This ensures that after concatenation of all DVFs from one motion phase to the same motion phase no displacement occurs. This repetitive and reproducible motion is a main assumption of many motion-compensation algorithms, including MoCo DWI. For this reason the cyclic constraint suggests itself to reduce inevitable errors. However, the realization of this constraint can lead to reduced magnitudes of the DVFs. However, the registration algorithm tends to underestimate motion already, so the cyclic constraint may increase this trend additionally.

The HDTV contains a voxel-dependent weight for the total variation constraint between adjacent motion phases ($(\bar{v}_{x,y,z})^{-1}$ see Eq. (2.21)). This weight factor depends on the velocity the registration algorithm determines at the specific voxel position x, y, z. If the velocity is low, this utilizes the opportunity for higher smoothing in temporal direction. If the velocity is high, this could lead to blurring and is thus omitted.

This introduces a chicken-and-egg situation where the image reconstruction requires the image registration which itself requires the image reconstruction in the first place. The joint-MoCo-HDTV solves this by using multiple resolution levels. In low resolution levels streak artifacts are of low concern and thus the regularization in temporal direction can be low by default. Then the registration algorithm is used and thus the estimated velocity is available in the next resolution level. However, here the risk is introduced that moving but small structures (e.g. blood vessels) are not visible in low resolution levels. This risk is increased because the HDTV regularization causes a spatial smoothing which can suppress these small intensity changes. In the next, higher resolution level the structures and its motion may become more prominent. Then the velocity depending, temporal weighting in the HDTV is increased and thus may suppress the motion but cause motion blurring instead.

To prevent the resulting holes the DVFs are smoothed. This is well suited to remove small areas of mediocre motion estimation. On the other hand to intensive smoothing causes incorrect estimation at tissue borders. Most prominent artifacts introduced are deformed bones, e.g. the spine, if they are close to actually moved organs.

Beneficial of joint-MoCo-HDTV is that is uses a multi-resolution approach for the motion estimation which utilizes the advantages of reconstruction from k-space. The multi-resolution approach is widely used for image registration. However, lower resolution levels are typically achieved by down sampling the volume from its final size. Instead, joint-MoCo-HDTV directly transforms the k-space into the desired (low) resolution level[1]. For this reason the images can show low streak artifacts. On the contrary the volume in its finals size — which is undersampled in k-space — shows severe streak artifacts. The down sampled volume would be impaired by them, too.

To summarize the positive effect of joint-MoCo-HDTV over other registration algorithms is not fully understood, yet. Several procedures, the cylic registration and constraint, HDTV, and smoothing of DVF and the combination of HDTV reconstruction and MoCo influence the final joint-MoCo-HDTV result. Future studies could evaluate which steps cause the improvement and foster these even more. The use of joint-MoCo-HDTV for MoCo DWI is justified because it was used for similar tasks before. Additionally, in the presented work the main goal was to evaluate MoCo DWI. If it works with joint-MoCo-HDTV, it will work with any better registration algorithm as well – if such an algorithm exists.

---

[1] The joint-MoCo-HDTV additionally uses a multi-resoulution motion estimation with down sampling in each here described resolution level.

List of Figures

List of Tables

Bibliography

Amrhein, Valentin, Sander Greenland, and Blake McShane (Mar. 2019). “Scientists Rise up against Statistical Significance”. In: *Nature* 567.7748, p. 305. DOI: `10.1038/d41586-019-00857-9`.

Anderson, Adam W. and John C. Gore (Nov. 18, 2005). “Analysis and Correction of Motion Artifacts in Diffusion Weighted Imaging”. In: *Magnetic Resonance in Medicine* 32.3, pp. 379–387. ISSN: 0740-3194. DOI: `10.1002/mrm.1910320313`.

Asif, M. Salman, Lei Hamilton, Marijn Brummer, and Justin Romberg (Sept. 1, 2013). “Motion-Adaptive Spatio-Temporal Regularization for Accelerated Dynamic MRI”. In: *Magn. Reson. Med.* 70.3, pp. 800–812. ISSN: 1522-2594. DOI: `10.1002/mrm.24524`.

Ayuso, Carmen, Jordi Rimola, Ramón Vilana, Marta Burrel, Anna Darnell, Ángeles García-Criado, Luis Bianchi, Ernest Belmonte, Carla Caparroz, Marta Barrufet, Jordi Bruix, and Concepción Brú (Apr. 1, 2018). “Diagnosis and Staging of Hepatocellular Carcinoma (HCC): Current Guidelines”. In: *European Journal of Radiology* 101, pp. 72–81. ISSN: 0720-048X. DOI: `10.1016/j.ejrad.2018.01.025`.

Bammer, Roland (Mar. 2003). “Basic Principles of Diffusion-Weighted Imaging”. In: *Eur. J. Radiol.* 45.3, pp. 169–184. ISSN: 0720048X. DOI: `10.1016/S0720-048X(02)00303-0`.

Blackall, J. M., A. P. King, G. P. Penney, A. Adam, and D. J. Hawkes (2001). “A Statistical Model of Respiratory Motion and Deformation of the Liver”. In: *Medical Image Computing and Computer-Assisted Intervention – MICCAI 2001.* Ed. by Wiro J. Niessen and Max A. Viergever. Red. by Gerhard Goos, Juris Hartmanis, and Jan van Leeuwen. Vol. 2208. Berlin, Heidelberg: Springer, pp. 1338–1340. ISBN: 978-3-540-42697-4 978-3-540-45468-7. DOI: `10.1007/3-540-45468-3_219`.

Bloch, F. (Oct. 1, 1946). “Nuclear Induction”. In: *Phys. Rev.* 70.7-8, pp. 460–474. DOI: `10.1103/PhysRev.70.460`.

Block, Kai Tobias, Hersh Chandarana, Sarah Milla, Mary Bruno, Tom Mulholland, Girish Fatterpekar, Mari Hagiwara, Robert Grimm, Christian Geppert, Berthold Kiefer, and Daniel K. Sodickson (June 1, 2014). “Towards Routine Clinical Use of Radial Stack-of-Stars 3D Gradient-Echo Sequences for Reducing Motion Sensitivity”. In: *J. Korean Soc. Magn. Reson. Med.* 18.2, pp. 87–106. ISSN: 1226-9751. DOI: `10.13104/jksmrm.2014.18.2.87`.

Block, Walter and Oliver Wieben (2012). “Non-Cartesian MR Angiography”. In: *Magnetic Resonance Angiography: Principles and Applications*. Ed. by James C. Carr and Timothy J. Carroll. New York, NY: Springer New York, pp. 169–183. ISBN: 978-1-4419-1686-0. DOI: `10.1007/978-1-4419-1686-0_13`.

Bonekamp, David, Susanne Bonekamp, Hsin-You Ou, Michael S. Torbenson, Celia Pamela Corona-Villalobos, Esteban Mezey, and Ihab R. Kamel (2014). “Assessing Liver Fibrosis: Comparison of Arterial Enhancement Fraction and Diffusion-Weighted Imaging”. In: *J. Magn. Reson. Imaging* 40.5, pp. 1137–1146. ISSN: 1522-2586. DOI: `10.1002/jmri.24472`.

Boyd, Stephen, Neal Parikh, Eric Chu, Borja Peleato, and Jonathan Eckstein (July 26, 2011). “Distributed Optimization and Statistical Learning via the Alternating Direction Method of Multipliers”. In: *MAL* 3.1, pp. 1–122. ISSN: 1935-8237, 1935-8245. DOI: `10.1561/2200000016`.

Brehm, Marcus, Pascal Paysan, Markus Oelhafen, Patrik Kunz, and Marc Kachelrieß (Dec. 1, 2012). “Self-Adapting Cyclic Registration for Motion-Compensated Cone-Beam CT in Image-Guided Radiation Therapy”. In: *Med. Phys.* 39.12, pp. 7603–7618. ISSN: 0094-2405. DOI: `10.1118/1.4766435`.

Brown, Robert (Sept. 1, 1828). “XXVII. A Brief Account of Microscopical Observations Made in the Months of June, July and August 1827, on the Particles Contained in the Pollen of Plants; and on the General Existence of Active Molecules in Organic and Inorganic Bodies”. In: *Philos. Mag.* 4.21, pp. 161–173. ISSN: 1941-5850. DOI: `10.1080/14786442808674769`.

Brown, Robert W., Yu-Chung N. Cheng, E. Mark Haacke, Michael R. Thompson, and Ramesh Venkatesan (2014a). “Introductory Signal Acquisition Methods”. In: *Magnetic Resonance Imaging*. John Wiley & Sons, Ltd, pp. 113–139. ISBN: 978-1-118-63395-3. DOI: `10.1002/9781118633953.ch8`.

Brown, Robert W., Yu-Chung N. Cheng, E. Mark Haacke, Michael R. Thompson, and Ramesh Venkatesan (May 16, 2014b). “Magnetization, Relaxation, and the Bloch Equation”. In: *Magnetic Resonance Imaging*. Hoboken, NJ, USA: John Wiley & Sons, Inc., pp. 53–66. ISBN: 978-1-118-63395-3 978-0-471-72085-0. DOI: `10.1002/9781118633953.ch4`.

Brown, Robert W., Yu-Chung N. Cheng, E. Mark Haacke, Michael R. Thompson, and Ramesh Venkatesan (2014c). “Multi-Dimensional Fourier Imaging and Slice Excitation”. In: *Magnetic Resonance Imaging*. John Wiley & Sons, Ltd, pp. 165–206. ISBN: 978-1-118-63395-3. DOI: `10.1002/9781118633953.ch10`.

Brown, Robert W., Yu-Chung N. Cheng, E. Mark Haacke, Michael R. Thompson, and Ramesh Venkatesan (May 16, 2014d). “One-Dimensional Fourier Imaging, κ-Space, and Gradient Echoes”. In: *Magnetic Resonance Imaging*. Hoboken, NJ, USA: John Wiley & Sons, Inc., pp. 141–164. ISBN: 978-1-118-63395-3 978-0-471-72085-0. DOI: `10.1002/9781118633953.ch9`.

Caldiroli, D. and L. Minati (Sept. 1, 2007). "Early Experience with Remote Pressure Sensor Respiratory Plethysmography Monitoring Sedation in the MR Scanner". In: *Eur. J. Anaesthesiol.* 24.9, pp. 761–769. ISSN: 0265-0215. DOI: `10.1017/S0265021507000312`. pmid: `17517150`.

Candes, E. J., J. Romberg, and T. Tao (Feb. 2006). "Robust Uncertainty Principles: Exact Signal Reconstruction from Highly Incomplete Frequency Information". In: *IEEE Trans. Inf. Theory* 52.2, pp. 489–509. ISSN: 0018-9448. DOI: `10.1109/TIT.2005.862083`.

Carr, H. Y. and E. M. Purcell (May 1, 1954). "Effects of Diffusion on Free Precession in Nuclear Magnetic Resonance Experiments". In: *Phys. Rev.* 94, pp. 630–638. DOI: `10.1103/physrev.94.630`.

Catana, Ciprian (2018). "PET/MRI: Motion Correction". In: *PET/MRI in Oncology: Current Clinical Applications.* Ed. by Andrei Iagaru, Thomas Hope, and Patrick Veit-Haibach. Cham: Springer International Publishing, pp. 77–96. ISBN: 978-3-319-68517-5. DOI: `10.1007/978-3-319-68517-5_5`.

Chandarana, Hersh and Bachir Taouli (Dec. 2010). "Diffusion and Perfusion Imaging of the Liver". In: *Eur. J. Radiol.* 76.3, pp. 348–358. ISSN: 0720048X. DOI: `10.1016/j.ejrad.2010.03.016`.

Chang, Lin-Ching, Derek K. Jones, and Carlo Pierpaoli (May 2005). "RESTORE: Robust Estimation of Tensors by Outlier Rejection". In: *Magn. Reson. Med.* 53.5, pp. 1088–1095. ISSN: 0740-3194, 1522-2594. DOI: `10.1002/mrm.20426`.

Chun, Se Young, Timothy G. Reese, Jinsong Ouyang, Bastien Guerin, Ciprian Catana, Xuping Zhu, Nathaniel M. Alpert, and Georges El Fakhri (Aug. 1, 2012). "MRI-Based Nonrigid Motion Correction in Simultaneous PET/MRI". In: *J Nucl Med* 53.8, pp. 1284–1291. ISSN: 0161-5505, 2159-662X. DOI: `10.2967/jnumed.111.092353`. pmid: 22743250.

CODATA (2018). *CODATA Value: Proton Gyromagnetic Ratio in MHz/T.* URL: `https://physics.nist.gov/cgi-bin/cuu/Value?gammapbar` (visited on 10/09/2019).

Damadian, Raymond (Mar. 19, 1971). "Tumor Detection by Nuclear Magnetic Resonance". In: *Science* 171.3976, pp. 1151–1153. ISSN: 0036-8075, 1095-9203. DOI: `10.1126/science.171.3976.1151`. pmid: 5544870.

Dávid, Christian, Nicolas GR Behl, Johanna Lott, Armin M Nagel, Reiner Umathum, Peter Bachert, Marc Kachelrieß, Mark E Ladd, and Tanja Platt (Mar. 2019). "In Vivo Motion-Compensated Abdominal Sodium (^{23}Na) Imaging at Ultrahigh Field (MoCASIm)". In: ISMRM Workshop on Ultrahigh Field Magnetic Resonance. Dubrovnik, Croatia.

Dávid, Christian, Thomas Vahle, Robert Grimm, Peter Bachert, and Marc Kachelrieß (Feb. 2019a). “Free-Breathing Motion-Compensated Diffusion-Weighted (MoCo DWI) Imaging”. In: European Congress of Radiology 2019. Vienna, Austria. DOI: `10.26044/ecr2019/C-2959`.

Dávid, Christian, Thomas Vahle, Robert Grimm, Peter Bachert, and Marc Kachelrieß (May 15, 2019b). “Motion Compensation for Free-Breathing Diffusion-Weighted Imaging (MoCo DWI)”. In: Proc. Intl. Soc. Mag. Reson. Med. (2019). Montreal, Canada.

Dávid, Christian, Thomas Vahle, Robert Grimm, Berthold Kiefer, Peter Bachert, and Marc Kachelrieß (Nov. 2018). “Motion Compensation for Free-Breathing Diffusion-Weighted Imaging (MoCo DWI) in Whole Body Integrated PET-MRI”. In: 2018 IEEE Nuclear Science Symposium and Medical Imaging Conference (NSS/MIC). #1773. Syndey, Australia: IEEE. ISBN: 978-1-5386-8494-8. DOI: `10.1109/NSSMIC.2018.8824522`.

Demberg, Kerstin, Frederik Bernd Laun, Marco Bertleff, Peter Bachert, and Tristan Anselm Kuder (May 25, 2018). “Experimental Determination of Pore Shapes Using Phase Retrieval from Q-Space NMR Diffraction”. In: *Phys. Rev. E* 97.5, p. 052412. DOI: `10.1103/PhysRevE.97.052412`.

Deng, Zixin, Jianing Pang, Wensha Yang, Yong Yue, Behzad Sharif, Richard Tuli, Debiao Li, Benedick Fraass, and Zhaoyang Fan (Apr. 1, 2016). “Four-Dimensional MRI Using Three-Dimensional Radial Sampling with Respiratory Self-Gating to Characterize Temporal Phase-Resolved Respiratory Motion in the Abdomen”. In: *Magnetic Resonance in Medicine* 75.4, pp. 1574–1585. ISSN: 0740-3194. DOI: `10.1002/mrm.25753`.

Deufelhard, Peter and Andreas Hohmann (2008). *Numerische Mathematik*. 4., überarb. und erw. Aufl. De Gruyter Lehrbuch. Berlin [u.a.]: de Gruyter. ISBN: 978-3-11-020354-7.

Dolde, Kai, Christian Dávid, Gernot Echner, Ralf Floca, Clemens Hentschke, Florian Maier, Nina Niebuhr, Kai Ohmstedt, Nami Saito, Merkur Alimusaj, Beate Fluegel, Patrick Naumann, Constantin Dreher, Martin Freitag, and Asja Pfaffenberger (Jan. 2019). “4DMRI-Based Analysis of Inter— and Intrafractional Pancreas Motion and Deformation with Different Immobilization Devices”. In: *Biomed. Phys. Eng. Express* 5.2, p. 025012. ISSN: 2057-1976. DOI: `10.1088/2057-1976/aaf9ae`.

Dolde, Kai, Patrick Naumann, Christian Dávid, Regula Gnirs, Marc Kachelrieß, Antony John Lomax, Nami Saito, Damien Charles Weber, Asja Pfaffenberger, and Ye Zhang (2018). “4D Dose Calculation for Pencil Beam Scanning Proton Therapy of Pancreatic Cancer Using Repeated 4DMRI Datasets”. In: *Phys. Med. Biol.* 63.16. Awarded “Highlights 2018” of Physics in Medicine and Biology, p. 165005. ISSN: 0031-9155. DOI: `10.1088/1361-6560/aad43f`.

Dolde, Kai, Patrick Naumann, Christian Dávid, Marc Kachelrieß, Antony John Lomax, Damien Charles Weber, Nami Saito, Lucas Norberto Burigo, Asja Pfaffenberger, and Ye Zhang (Mar.

2019). “Comparing the Effectiveness and Efficiency of Various Gating Approaches for PBS Proton Therapy of Pancreatic Cancer Using 4D-MRI Datasets”. In: *Phys. Med. Biol.* ISSN: 0031-9155. DOI: `10.1088/1361-6560/ab1175`.

Dolde, Kai, Sergej Schneider, Sarah Stefanowicz, Merkur Alimusaj, Beate Flügel, Nami Saito, Esther G. C. Troost, Asja Pfaffenberger, and Aswin L. Hoffmann (June 2019). “Comparison of Pancreatic Respiratory Motion Management with Three Abdominal Corsets for Particle Radiation Therapy: Case Study”. In: *J Appl Clin Med Phys* 20.6, pp. 111–119. ISSN: 1526-9914. DOI: `10.1002/acm2.12613`. pmid: `31120639`.

Dolde, Kai, Ye Zhang, Naved Chaudhri, Christian Dávid, Marc Kachelrieß, Antony John Lomax, Patrick Naumann, Nami Saito, Damien Charles Weber, and Asja Pfaffenberger (Feb. 7, 2019). “4DMRI-Based Investigation on the Interplay Effect for Pencil Beam Scanning Proton Therapy of Pancreatic Cancer Patients”. In: *Radiation Oncology* 14.1, p. 30. ISSN: 1748-717X. DOI: `10.1186/s13014-019-1231-2`.

Earls, James P., Vincent B. Ho, Thomas K. Foo, Ernesto Castillo, and Scott D. Flamm (Aug. 1, 2002). “Cardiac MRI: Recent Progress and Continued Challenges”. In: *J. Magn. Reson. Imaging* 16.2, pp. 111–127. ISSN: 1522-2586. DOI: `10.1002/jmri.10154`.

Fahmi, Shamel, Frank F.J. Simonis, and Momen Abayazid (Dec. 2018). “Respiratory Motion Estimation of the Liver with Abdominal Motion as a Surrogate”. In: *Int. J. Med. Robot.* 14.6. Ed. by Loughlin Clive, e1940. ISSN: 14785951. DOI: `10.1002/rcs.1940`.

Feng, Li, Leon Axel, Hersh Chandarana, Kai Tobias Block, Daniel K. Sodickson, and Ricardo Otazo (Feb. 1, 2016). “XD-GRASP: Golden-Angle Radial MRI with Reconstruction of Extra Motion-State Dimensions Using Compressed Sensing”. In: *Magn. Reson. Med.* 75.2, pp. 775–788. ISSN: 1522-2594. DOI: `10.1002/mrm.25665`.

Fontana, Giulia, Marco Riboldi, Chiara Gianoli, Cezarina I. Chirvase, Gaetano Villa, Chiara Paganelli, Paul E. Summers, Barbara Tagaste, Andrea Pella, Piero Fossati, Mario Ciocca, Guido Baroni, Francesca Valvo, and Roberto Orecchia (2016). “MRI Quantification of Pancreas Motion as a Function of Patient Setup for Particle Therapy —a Preliminary Study”. In: *J. Appl. Clin. Med. Phys.* 17.5, pp. 60–75. ISSN: 1526-9914. DOI: `10.1120/jacmp.v17i5.6236`.

Fourier, Jean Baptiste Joseph (1822). *Théorie analytique de la chaleur.* Paris, France: Firmin Didot, père et fils. 639 pp. URL: `http://archive.org/details/thorieanalytiqu00fourgoog` (visited on 04/05/2019).

Freedman, Joshua N., David J. Collins, Hannah Bainbridge, Christopher M. Rank, Simeon Nill, Marc Kachelrieß, Uwe Oelfke, Martin O. Leach, and Andreas Wetscherek (Oct. 2017). “T2-Weighted 4D Magnetic Resonance Imaging for Application in Magnetic Resonance–Guided

Radiotherapy Treatment Planning". In: *Invest. Radiol.* 52.10, p. 563. ISSN: 0020-9996. DOI: `10.1097/RLI.0000000000000381`.

Fürst, Sebastian, Robert Grimm, Inki Hong, Michael Souvatzoglou, Michael E. Casey, Markus Schwaiger, Stephan G. Nekolla, and Sibylle I. Ziegler (Feb. 1, 2015). "Motion Correction Strategies for Integrated PET/MR". In: *J Nucl Med* 56.2, pp. 261–269. ISSN: 0161-5505, 2159-662X. DOI: `10.2967/jnumed.114.146787`. pmid: 25572092.

Gerlach, Walther and Otto Stern (Dec. 1922). "Der Experimentelle Nachweis Der Richtungsquantelung Im Magnetfeld". In: *Z. Für Phys.* 9.1, pp. 349–352. ISSN: 1434-6001, 1434-601X. DOI: `10.1007/BF01326983`.

Gottumukkala, Ravi V., Michael S. Gee, Perry J. Hampilos, and Mary-Louise C. Greer (Jan. 25, 2019). "Current and Emerging Roles of Whole-Body MRI in Evaluation of Pediatric Cancer Patients". In: *RadioGraphics*, p. 180130. ISSN: 0271-5333. DOI: `10.1148/rg.2019180130`.

Grimm, Robert, Sebastian Fürst, Michael Souvatzoglou, Christoph Forman, Jana Hutter, Isabel Dregely, Sibylle I. Ziegler, Berthold Kiefer, Joachim Hornegger, Kai Tobias Block, and Stephan G. Nekolla (Jan. 2015). "Self-Gated MRI Motion Modeling for Respiratory Motion Compensation in Integrated PET/MRI". In: *Medical Image Analysis* 19.1, pp. 110–120. ISSN: 1361-8415. DOI: `10.1016/j.media.2014.08.003`.

Gudbjartsson, HáKon and Samuel Patz (Dec. 1995). "The Rician Distribution of Noisy Mri Data". In: *Magn. Reson. Med.* 34.6, pp. 910–914. ISSN: 07403194, 15222594. DOI: `10.1002/mrm.1910340618`.

Guyader, Jean-Marie, Livia Bernardin, Naomi H. M. Douglas, Dirk H. J. Poot, Wiro J. Niessen, and Stefan Klein (Aug. 1, 2015). "Influence of Image Registration on Apparent Diffusion Coefficient Images Computed from Free-Breathing Diffusion MR Images of the Abdomen". In: *J. Magn. Reson. Imaging* 42.2, pp. 315–330. ISSN: 1522-2586. DOI: `10.1002/jmri.24792`.

Hahn, E. L. (Nov. 15, 1950). "Spin Echoes". In: *Phys. Rev.* 80.4, pp. 580–594. ISSN: 0031-899X. DOI: `10.1103/PhysRev.80.580`.

Hankey, Graeme J (Feb. 11, 2017). "Stroke". In: *The Lancet* 389.10069, pp. 641–654. ISSN: 0140-6736. DOI: `10.1016/S0140-6736(16)30962-X`.

Holland, Dominic, Joshua M. Kuperman, and Anders M. Dale (Mar. 2010). "Efficient Correction of Inhomogeneous Static Magnetic Field-Induced Distortion in Echo Planar Imaging". In: *NeuroImage* 50.1, pp. 175–183. ISSN: 10538119. DOI: `10.1016/j.neuroimage.2009.11.044`.

Hu, Yong, Yong-Kang Zhou, Yi-Xing Chen, and Zhao-Chong Zeng (Dec. 2017). "Magnitude and Influencing Factors of Respiration-Induced Liver Motion during Abdominal Compression in Patients with Intrahepatic Tumors". In: *Radiat. Oncol.* 12.1. ISSN: 1748-717X. DOI: `10.1186/s13014-016-0762-z`.

Ishii, Shirou, Takamitsu Hara, Takeyuki Nanbu, Hiroki Suenaga, Shigeyasu Sugawara, Daichi Kuroiwa, Hirofumi Sekino, Masayuki Miyajima, Hitoshi Kubo, Noboru Oriuchi, and Hiroshi Ito (Nov. 1, 2016). "Optimized Workflow and Imaging Protocols for Whole-Body Oncologic PET/MRI". In: *Jpn J Radiol* 34.11, pp. 754–762. ISSN: 1867-108X. DOI: `10.1007/s11604-016-0584-9`.

Jahnke, Cosima, Ingo Paetsch, Stephan Achenbach, Bernhard Schnackenburg, Rolf Gebker, Eckart Fleck, and Eike Nagel (Apr. 1, 2006). "Coronary MR Imaging: Breath-Hold Capability and Patterns, Coronary Artery Rest Periods, and β-Blocker Use". In: *Radiology* 239.1, pp. 71–78. ISSN: 0033-8419. DOI: `10.1148/radiol.2383042019`.

Jaimes, Camilo and Michael S. Gee (May 1, 2016). "Strategies to Minimize Sedation in Pediatric Body Magnetic Resonance Imaging". In: *Pediatr Radiol* 46.6, pp. 916–927. ISSN: 1432-1998. DOI: `10.1007/s00247-016-3613-z`.

Johansson, Adam, James M. Balter, and Yue Cao (Oct. 1, 2018). "Abdominal DCE-MRI Reconstruction with Deformable Motion Correction for Liver Perfusion Quantification". In: *Medical Physics* 45.10, pp. 4529–4540. ISSN: 0094-2405. DOI: `10.1002/mp.13118`.

Kandpal, Harsh, Raju Sharma, K. S. Madhusudhan, and Kulwant Singh Kapoor (Apr. 1, 2009). "Respiratory-Triggered Versus Breath-Hold Diffusion-Weighted MRI of Liver Lesions: Comparison of Image Quality and Apparent Diffusion Coefficient Values". In: *American Journal of Roentgenology* 192.4, pp. 915–922. ISSN: 0361-803X. DOI: `10.2214/AJR.08.1260`.

Kanematsu, Masayuki, Satoshi Goshima, Haruo Watanabe, Hiroshi Kondo, Hiroshi Kawada, Yoshifumi Noda, Akinori Aomatsu, and Noriyuki Moriyama (Apr. 2013). "Detection and Characterization of Focal Hepatic Lesions with Diffusion-Weighted MR Imaging: A Pictorial Review". In: *Abdom. Imaging* 38.2, pp. 297–308. ISSN: 0942-8925, 1432-0509. DOI: `10.1007/s00261-012-9940-0`.

Klein, S., M. Staring, K. Murphy, M. A. Viergever, and J. P. W. Pluim (Jan. 2010). "Elastix: A Toolbox for Intensity-Based Medical Image Registration". In: *IEEE Trans. Med. Imaging* 29.1, pp. 196–205. ISSN: 0278-0062. DOI: `10.1109/TMI.2009.2035616`.

Koh, D. M., G. Brown, A. M. Riddell, E. Scurr, D. J. Collins, S. D. Allen, I. Chau, D. Cunningham, N. M. deSouza, M. O. Leach, and J. E. Husband (Jan. 12, 2008). "Detection of Colorectal Hepatic Metastases Using MnDPDP MR Imaging and Diffusion-Weighted Imaging (DWI) Alone and in Combination". In: *Eur Radiol* 18.5, p. 903. ISSN: 1432-1084. DOI: `10.1007/s00330-007-0847-z`.

Kohler, T. (Oct. 2004). "A Projection Access Scheme for Iterative Reconstruction Based on the Golden Section". In: *IEEE Symposium Conference Record Nuclear Science 2004.* IEEE Symposium Conference Record Nuclear Science 2004. Vol. 6, 3961–3965 Vol. 6. DOI: `10.1109/NSSMIC.2004.1466745`.

Kolb, Christoph, Andreas Wetscherek, Maria Teodora Buzan, Rene Werner, Christopher M. Rank, Marc Kachelrieß, Michael Kreuter, Julien Dinkel, Claus Peter Heuel, and Klaus Maier-Hein (Apr. 2, 2016). "Regional lung ventilation analysis using temporally resolved magnetic resonance imaging". In: *J. Comput. Assist. Tomogr.* 40, pp. 899–906. ISSN: 0363-8715. DOI: `10.1097/RCT.0000000000000450`.

Korzowski, Andreas and Peter Bachert (2018). "High-Resolution 31P Echo-Planar Spectroscopic Imaging in Vivo at 7T". In: *Magn. Reson. Med.* 79.3, pp. 1251–1259. ISSN: 1522-2594. DOI: `10.1002/mrm.26785`.

Kostelec, Peter J., John B. Weaver, and Dennis M. Healy (1998). "Multiresolution Elastic Image Registration". In: *Med. Phys.* 25.9, pp. 1593–1604. ISSN: 2473-4209. DOI: `10.1118/1.598403`.

Kuder, Tristan Anselm and Frederik Bernd Laun (Aug. 13, 2015). "Effects of Pore-Size and Shape Distributions on Diffusion Pore Imaging by Nuclear Magnetic Resonance". In: *Phys. Rev. E* 92.2, p. 022706. DOI: `10.1103/PhysRevE.92.022706`.

Küstner, Thomas, Martin Schwartz, Petros Martirosian, Sergios Gatidis, Ferdinand Seith, Christopher Gilliam, Thierry Blu, Hadi Fayad, Dimitris Visvikis, F. Schick, B. Yang, H. Schmidt, and N. F. Schwenzer (Dec. 1, 2017). "MR-Based Respiratory and Cardiac Motion Correction for PET Imaging". In: *Medical Image Analysis* 42, pp. 129–144. ISSN: 1361-8415. DOI: `10.1016/j.media.2017.08.002`.

Laun, F.B., K.H. Fritzsche, T.A. Kuder, and B. Stieltjes (Mar. 2011). "Einführung in die Grundlagen und Techniken der Diffusionsbildgebung". In: *Radiol.* 51.3, pp. 170–179. ISSN: 0033-832X, 1432-2102. DOI: `10.1007/s00117-010-2057-y`.

Lauterbur, Paul C. (Mar. 16, 1973). "Image Formation by Induced Local Interactions: Examples Employing Nuclear Magnetic Resonance". In: *Nature* 242, pp. 190–191. URL: `http://www.nature.com/physics/looking-back/lauterbur/index.html`.

Le Bihan, Denis (Feb. 15, 2019). "What Can We See with IVIM MRI?" In: *NeuroImage*. Physiological and Quantitative MRI 187, pp. 56–67. ISSN: 1053-8119. DOI: `10.1016/j.neuroimage.2017.12.062`.

Liu, Jing, Pascal Spincemaille, Noel C. F. Codella, Thanh D. Nguyen, Martin R. Prince, and Yi Wang (2010). "Respiratory and Cardiac Self-Gated Free-Breathing Cardiac CINE Imaging with Multiecho 3D Hybrid Radial SSFP Acquisition". In: *Magn. Reson. Med.* 63.5, pp. 1230–1237. ISSN: 1522-2594. DOI: `10.1002/mrm.22306`.

Liu, Yilin, Fang-Fang Yin, Brian Gary Czito, Mustafa R. Bashir, Manisha Palta, Xiaodong Zhong, Brian M. Dale, and Jing Cai (2016). "Potential Improvement in Apparent Diffusion Coefficient (ADC) Measurement by Respiratory Correlated Four Dimensional Diffusion-Weighted MRI (4D-DWI): Initial Investigation on Digital Phantoms and Human Subjects".

In: Proc. Intl. Soc. Mag. Reson. Med. 24 (2016). URL: `http://cds.ismrm.org/protected/16MPresentations/abstracts/0624.html`.

Liu, Yilin, Xiaodong Zhong, Brian G. Czito, Manisha Palta, Mustafa R. Bashir, Dale Brian M., Yin Fang-Fang, and Cai Jing (Feb. 16, 2017). "Four-dimensional Diffusion-weighted MR Imaging (4D-DWI): A Feasibility Study". In: *Medical Physics* 44.2, pp. 397–406. ISSN: 0094-2405. DOI: `10.1002/mp.12037`. pmid: 28121369.

Lustig, M., D.L. Donoho, J.M. Santos, and J.M. Pauly (Mar. 2008). "Compressed Sensing MRI". In: *IEEE Signal Process. Mag.* 25.2, pp. 72–82. ISSN: 1053-5888. DOI: `10.1109/MSP.2007.914728`.

Mannelli, Lorenzo, Puneet Bhargava, Sherif F. Osman, Eytan Raz, Mariam Moshiri, Giacomo Laffi, Gregory J. Wilson, and Jeffrey H. Maki (May 2013). "Diffusion-Weighted Imaging of the Liver: A Comprehensive Review". In: *Curr. Probl. Diagn. Radiol.* 42.3, pp. 77–83. ISSN: 03630188. DOI: `10.1067/j.cpradiol.2012.07.001`.

Markl, Michael and Jochen Leupold (2012). "Gradient Echo Imaging". In: *J. Magn. Reson. Imaging* 35.6, pp. 1274–1289. ISSN: 1522-2586. DOI: `10.1002/jmri.23638`.

Martinez-Möller, Axel, Matthias Eiber, Stephan G. Nekolla, Michael Souvatzoglou, Alexander Drzezga, Sibylle Ziegler, Ernst J. Rummeny, Markus Schwaiger, and Ambros J. Beer (Sept. 1, 2012). "Workflow and Scan Protocol Considerations for Integrated Whole-Body PET/MRI in Oncology". In: *J Nucl Med* 53.9, pp. 1415–1426. ISSN: 0161-5505, 2159-662X. DOI: `10.2967/jnumed.112.109348`. pmid: 22879079.

Mazaheri, Yousef, Richard K. G. Do, Amita Shukla-Dave, Joseph O. Deasy, Yonggang Lu, and Oguz Akin (Dec. 1, 2012). "Motion Correction of Multi-b-Value Diffusion-Weighted Imaging in the Liver". In: *Academic Radiology* 19.12, pp. 1573–1580. ISSN: 1076-6332, 1878-4046. DOI: `10.1016/j.acra.2012.07.005`. pmid: 22963726.

McClelland, J. R., D. J. Hawkes, T. Schaeffter, and A. P. King (Jan. 2013). "Respiratory Motion Models: A Review". In: *Medical Image Analysis* 17.1, pp. 19–42. ISSN: 1361-8415. DOI: `10.1016/j.media.2012.09.005`.

Menten, Martin J., Martin F. Fast, Andreas Wetscherek, Christopher M. Rank, Marc Kachelrieß, David J. Collins, Simeon Nill, and Uwe Oelfke (Nov. 2018). "The Impact of 2D Cine MR Imaging Parameters on Automated Tumor and Organ Localization for MR-Guided Real-Time Adaptive Radiotherapy". In: *Phys. Med. Biol.* 63.23, p. 16. ISSN: 0031-9155. DOI: `10.1088/1361-6560/aae74d`.

Mickevicius, Nikolai J. and Eric S. Paulson (2017). "Investigation of Undersampling and Reconstruction Algorithm Dependence on Respiratory Correlated 4D-MRI for Online MR-Guided Radiation Therapy". In: *Phys. Med. Biol.* 62.8, p. 2910. ISSN: 0031-9155. DOI: `10.1088/1361-6560/aa54f2`.

Nguyen, Christopher, Zhaoyang Fan, Behzad Sharif, Yi He, Rohan Dharmakumar, Daniel S. Berman, and Debiao Li (Nov. 2014). "In Vivo Three-Dimensional High Resolution Cardiac Diffusion-Weighted MRI: A Motion Compensated Diffusion-Prepared Balanced Steady-State Free Precession Approach: 3D High Resolution Cardiac DW-MRI via Diffusion-Prepared bSSFP". In: *Magn. Reson. Med.* 72.5, pp. 1257–1267. ISSN: 07403194. DOI: `10.1002/mrm.25038`.

Nketiah, Gabriel, Kirsten M. Selnæs, Elise Sandsmark, Jose R. Teruel, Brage Krüger-Stokke, Helena Bertilsson, Tone F. Bathen, and Mattijs Elschot (May 1, 2018). "Geometric Distortion Correction in Prostate Diffusion-Weighted MRI and Its Effect on Quantitative Apparent Diffusion Coefficient Analysis". In: *Magn. Reson. Med.* 79.5, pp. 2524–2532. ISSN: 1522-2594. DOI: `10.1002/mrm.26899`.

Nyquist, H. (Jan. 1924). "Certain Factors Affecting Telegraph Speed". In: *Am. Inst. Electr. Eng. Trans. Of* XLIII, pp. 412–422. ISSN: 0096-3860. DOI: `10.1109/T-AIEE.1924.5060996`.

OECD (2019). *Magnetic Resonance Imaging (MRI) Exams (Idicator)*. URL: `https://doi.org/10.1787/1d89353f-en`.

Pathak, Ryan, Hossein Ragheb, Neil A. Thacker, David M. Morris, Houshang Amiri, Joost Kuijer, Nandita M. deSouza, Arend Heerschap, and Alan Jackson (Oct. 26, 2017). "A Data-Driven Statistical Model That Estimates Measurement Uncertainty Improves Interpretation of ADC Reproducibility: A Multi-Site Study of Liver Metastases". In: *Sci. Rep.* 7.1, p. 14084. ISSN: 2045-2322. DOI: `10.1038/s41598-017-14625-0`.

Paul, Jan, Evica Divkovic, Stefan Wundrak, Peter Bernhardt, Wolfgang Rottbauer, Heiko Neumann, and Volker Rasche (Jan. 29, 2014). "High-resolution Respiratory Self-gated Golden Angle Cardiac MRI: Comparison of Self-gating Methods in Combination with K-t SPARSE SENSE". In: *Magnetic Resonance in Medicine* 73.1, pp. 292–298. ISSN: 0740-3194. DOI: `10.1002/mrm.25102`.

Platt, Tanja, Reiner Umathum, Thomas M. Fiedler, Armin M. Nagel, Andreas K. Bitz, Florian Maier, Peter Bachert, Mark E. Ladd, Mark O. Wielpütz, Hans-Ulrich Kauczor, and Nicolas G. R. Behl (Sept. 1, 2018). "In Vivo Self-Gated 23Na MRI at 7 T Using an Oval-Shaped Body Resonator". In: *Magn. Reson. Med.* 80.3, pp. 1005–1019. ISSN: 1522-2594. DOI: `10.1002/mrm.27103`.

Porter, David A. and Robin M. Heidemann (Aug. 1, 2009). "High Resolution Diffusion-Weighted Imaging Using Readout-Segmented Echo-Planar Imaging, Parallel Imaging and a Two-Dimensional Navigator-Based Reacquisition". In: *Magn. Reson. Med.* 62.2, pp. 468–475. ISSN: 1522-2594. DOI: `10.1002/mrm.22024`.

Purcell, E. M., H. C. Torrey, and R. V. Pound (Jan. 1, 1946). “Resonance Absorption by Nuclear Magnetic Moments in a Solid”. In: *Phys. Rev.* 69.1-2, pp. 37–38. DOI: `10.1103/PhysRev.69.37`.

Quick, Harald H., Ralf Ladebeck, and Jens-Christoph Georgi (Jan. 2011). “Whole-Body MR/PET Hybrid Imaging: Technical Considerations, Clinical Workfl Ow, and Initial Results”. In: *MReadings*. Reprinted from MAGNETOM Flash 1/2011, pp. 14–26. URL: `https://static.healthcare.siemens.com/siemens_hwem-hwem_ssxa_websites-context-root/wcm/idc/groups/public/@global/@imaging/@mri/documents/download/mdaw/mje0/~edisp/mri-biograph-mmr-mreading-molecular-mri-00206637.pdf` (visited on 04/15/2019).

Ragheb, Hossein, Neil A. Thacker, Jean-Marie Guyader, Stefan Klein, Nandita M. deSouza, and Alan Jackson (July 23, 2015). “The Accuracy of ADC Measurements in Liver Is Improved by a Tailored and Computationally Efficient Local-Rigid Registration Algorithm”. In: *PLOS ONE* 10.7. Ed. by Jie Tian, e0132554. ISSN: 1932-6203. DOI: `10.1371/journal.pone.0132554`.

Rank, Christopher M. (Dec. 13, 2016). “Motion-Compensated Image Reconstruction for Magnetic Resonance (MR) Imaging and for Simultaneous Positron Emission Tomography/MR Imaging”. Dissertation. Heidelberg, Germany: Universität Heidelberg. 136 pp.

Rank, Christopher M., Thorsten Heußer, Maria T. A. Buzan, Andreas Wetscherek, Martin T. Freitag, Julien Dinkel, and Marc Kachelrieß (Mar. 1, 2016). “4D Respiratory Motion-Compensated Image Reconstruction of Free-Breathing Radial MR Data with Very High Undersampling”. In: *Magn. Reson. Med.* ISSN: 1522-2594. DOI: `10.1002/mrm.26206`.

Rank, Christopher M., Thorsten Heußer, Andreas Wetscherek, Martin T. Freitag, Oliver Sedlaczek, Heinz-Peter Schlemmer, and Marc Kachelrieß (Dec. 1, 2016). “Respiratory Motion Compensation for Simultaneous PET/MR Based on Highly Undersampled MR Data”. In: *Med. Phys.* 43.12, pp. 6234–6245. ISSN: 0094-2405. DOI: `10.1118/1.4966128`.

Ritschl, Ludwig, Frank Bergner, Christof Fleischmann, and Marc Kachelrieß (2011). “Improved Total Variation-Based CT Image Reconstruction Applied to Clinical Data”. In: *Phys. Med. Biol.* 56.6, p. 1545. ISSN: 0031-9155. DOI: `10.1088/0031-9155/56/6/003`.

Ritschl, Ludwig, Stefan Sawall, Michael Knaup, Andreas Hess, and Marc Kachelrieß (Mar. 21, 2012). “Iterative 4D Cardiac Micro-CT Image Reconstruction Using an Adaptive Spatio-Temporal Sparsity Prior”. In: *Phys. Med. Biol.* 57.6. WOS:000301358000004, pp. 1517–1525. ISSN: 0031-9155. DOI: `10.1088/0031-9155/57/6/1517`.

Rohlfing, Torsten, Calvin R. Maurer Jr., Walter G. O’Dell, and Jianhui Zhong (May 28, 2001). “Modeling Liver Motion and Deformation during the Respiratory Cycle Using Intensity-Based Free-Form Registration of Gated MR Images”. In: Medical Imaging 2001. Ed. by Seong K. Mun. San Diego, CA, pp. 337–348. DOI: `10.1117/12.428073`.

Rohlfing, Torsten, Calvin R. Maurer, Walter G. O'Dell, and Jianhui Zhong (2004). "Modeling Liver Motion and Deformation during the Respiratory Cycle Using Intensity-Based Non-rigid Registration of Gated MR Images". In: *Med. Phys.* 31.3, pp. 427–432. ISSN: 2473-4209. DOI: `10.1118/1.1644513`.

Rosenkrantz, Andrew B., Anwar R. Padhani, Thomas L. Chenevert, Dow-Mu Koh, Frederik De Keyzer, Bachir Taouli, and Denis Le Bihan (2015). "Body Diffusion Kurtosis Imaging: Basic Principles, Applications, and Considerations for Clinical Practice". In: *J. Magn. Reson. Imaging* 42.5, pp. 1190–1202. ISSN: 1522-2586. DOI: `10.1002/jmri.24985`.

Sanz-Estébanez, Santiago, Iñaki Rabanillo-Viloria, Javier Royuela-del-Val, Santiago Aja-Fernández, and Carlos Alberola-López (Feb. 1, 2018). "Joint Groupwise Registration and ADC Estimation in the Liver Using a B-Value Weighted Metric". In: *Magnetic Resonance Imaging* 46, pp. 1–9. ISSN: 0730-725X. DOI: `10.1016/j.mri.2017.10.002`.

Schmid-Tannwald, Christine, Aytekin Oto, Maximilian F. Reiser, and Christoph J. Zech (2013). "Diffusion-Weighted MRI of the Abdomen: Current Value in Clinical Routine". In: *J. Magn. Reson. Imaging* 37.1, pp. 35–47. ISSN: 1522-2586. DOI: `10.1002/jmri.23643`.

Shenoy-Bhangle, Anuradha, Vinit Baliyan, Hamed Kordbacheh, Alexander R Guimaraes, and Avinash Kambadakone (Sept. 18, 2017). "Diffusion Weighted Magnetic Resonance Imaging of Liver: Principles, Clinical Applications and Recent Updates". In: *World J Hepatol* 9.26, pp. 1081–1091. ISSN: 1948-5182. DOI: `10.4254/wjh.v9.i26.1081`. pmid: 28989564.

Smith, Steven W. (1997). *The Scientist and Engineer's Guide to Digital Signal Processing*. San Diego, Calif.: California Technical Pub. XIV, 626 S. ISBN: 978-0-9660176-3-2. URL: `http://www.dspguide.com/` (visited on 01/29/2019).

Som, P., H. L. Atkins, D. Bandoypadhyay, J. S. Fowler, R. R. MacGregor, K. Matsui, Z. H. Oster, D. F. Sacker, C. Y. Shiue, H. Turner, C.-N. Wan, A. P. Wolf, and S. V. Zabinski (Jan. 7, 1980). "A Fluorinated Glucose Analog, 2-Fluoro-2-Deoxy-D-Glucose (F-18): Nontoxic Tracer for Rapid Tumor Detection". In: *J Nucl Med* 21.7, pp. 670–675. ISSN: 0161-5505, 2159-662X. pmid: 7391842. URL: `http://jnm.snmjournals.org/content/21/7/670` (visited on 04/25/2019).

Sotiras, A., C. Davatzikos, and N. Paragios (July 2013). "Deformable Medical Image Registration: A Survey". In: *IEEE Trans. Med. Imaging* 32.7, pp. 1153–1190. ISSN: 0278-0062. DOI: `10.1109/TMI.2013.2265603`.

Taouli, Bachir, Ambros J. Beer, Thomas Chenevert, David Collins, Constance Lehman, Celso Matos, Anwar R. Padhani, Andrew B. Rosenkrantz, Amita Shukla-Dave, Eric Sigmund, Lawrence Tanenbaum, Harriet Thoeny, Isabelle Thomassin-Naggara, Sebastiano Barbieri, Idoia Corcuera-Solano, Matthew Orton, Savannah C. Partridge, and Dow-Mu Koh (2016). "Diffusion-Weighted Imaging Outside the Brain: Consensus Statement from an ISMRM-

Sponsored Workshop". In: *J. Magn. Reson. Imaging* 44.3, pp. 521–540. ISSN: 1522-2586. DOI: `10.1002/jmri.25196`.

Taouli, Bachir, Alison Sandberg, Alto Stemmer, Tejas Parikh, Samson Wong, Jian Xu, and Vivian S. Lee (2009). "Diffusion-Weighted Imaging of the Liver: Comparison of Navigator Triggered and Breathhold Acquisitions". In: *J. Magn. Reson. Imaging* 30.3, pp. 561–568. ISSN: 1522-2586. DOI: `10.1002/jmri.21876`.

Thirion, J. -P. (Sept. 1, 1998). "Image Matching as a Diffusion Process: An Analogy with Maxwell's Demons". In: *Medical Image Analysis* 2.3, pp. 243–260. ISSN: 1361-8415. DOI: `10.1016/S1361-8415(98)80022-4`.

Treiber, Jeffrey Mark, Nathan S. White, Tyler Christian Steed, Hauke Bartsch, Dominic Holland, Nikdokht Farid, Carrie R. McDonald, Bob S. Carter, Anders Martin Dale, and Clark C. Chen (Mar. 30, 2016). "Characterization and Correction of Geometric Distortions in 814 Diffusion Weighted Images". In: *PLoS ONE* 11.3. Ed. by Joseph Najbauer, e0152472. ISSN: 1932-6203. DOI: `10.1371/journal.pone.0152472`.

Vahle, Thomas, Mario Bacher, David Rigie, Matthias Fenchel, Peter Speier, Jan Bollenbeck, Klaus P Schäfers, Berthold Kiefer, and Fernando E Boada (2020). "Respiratory Motion Detection and Correction for MR Using the Pilot Tone: Applications for MR and Simultaneous PET/MR Exams". In: 55. in press.

Van de Lindt, Tessa N., Martin F. Fast, Uulke A. van der Heide, and Jan-Jakob Sonke (June 1, 2018). "Retrospective Self-Sorted 4D-MRI for the Liver". In: *Radiotherapy and Oncology* 127.3, pp. 474–480. ISSN: 0167-8140. DOI: `10.1016/j.radonc.2018.05.006`.

Vercauteren, Tom, Xavier Pennec, Aymeric Perchant, and Nicholas Ayache (Mar. 1, 2009). "Diffeomorphic Demons: Efficient Non-Parametric Image Registration". In: *NeuroImage*. Mathematics in Brain Imaging 45 (1, Supplement 1), S61–S72. ISSN: 1053-8119. DOI: `10.1016/j.neuroimage.2008.10.040`.

Weishaupt, Dominik, Victor D. Köchli, and Borut Marincek (2014). *Wie funktioniert MRI?* 7th ed. Springer Berlin Heidelberg. 180 pp. ISBN: 978-3-642-41615-6 978-3-642-41616-3. DOI: `10.1007/978-3-642-41616-3`.

WHO (Jan. 10, 2004). "Appropriate Body-Mass Index for Asian Populations and Its Implications for Policy and Intervention Strategies". In: *The Lancet* 363.9403, pp. 157–163. ISSN: 0140-6736. DOI: `10.1016/S0140-6736(03)15268-3`.

Winkelmann, S., T. Schaeffter, T. Koehler, H. Eggers, and O. Doessel (Jan. 2007). "An Optimal Radial Profile Order Based on the Golden Ratio for Time-Resolved MRI". In: *IEEE Trans. Med. Imaging* 26.1, pp. 68–76. ISSN: 0278-0062. DOI: `10.1109/TMI.2006.885337`.

Wolff, S D and R S Balaban (1990). "Regulation of the Predominant Renal Medullary Organic Solutes in VIVO". In: *Annu. Rev. Physiol.* 52.1, pp. 727–746. DOI: `10.1146/annurev.ph.52.030190.003455`.

Würslin, Christian, Holger Schmidt, Petros Martirosian, Cornelia Brendle, Andreas Boss, Nina F. Schwenzer, and Lars Stegger (Mar. 1, 2013). "Respiratory Motion Correction in Oncologic PET Using T1-Weighted MR Imaging on a Simultaneous Whole-Body PET/MR System". In: *J Nucl Med* 54.3, pp. 464–471. ISSN: 0161-5505, 2159-662X. DOI: `10.2967/jnumed.112.105296`. pmid: 23287577.

Publications

During the work for this doctorate these articles were published.

Peer-Reviewed Journal Articles

Dolde, K., **Dávid, C.**, Echner, G., Floca, R., Hentschke, C., Maier, F., Niebuhr, N., Ohmstedt, K., Saito, N., Alimusaj, M., Fluegel, B., Naumann, P., Dreher, C., Freitag, M., Pfaffenberger, A., (Jan. 2019). “4DMRI-Based Analysis of Inter— and Intrafractional Pancreas Motion and Deformation with Different Immobilization Devices”. In: *Biomed. Phys. Eng. Express* 5.2, p. 025012. ISSN: 2057-1976. DOI: 10.1088/2057-1976/aaf9ae.

Dolde, K., Naumann, P., **Dávid, C.**, Gnirs, R., Kachelrieß, M., Lomax, A. J., Nami Saito, Weber, D. C., Pfaffenberger, A., Zhang, Y., (2018). “4D Dose Calculation for Pencil Beam Scanning Proton Therapy of Pancreatic Cancer Using Repeated 4DMRI Datasets”. In: *Phys. Med. Biol.* 63.16. Awarded “Highlights 2018” of Physics in Medicine and Biology, p. 165005. ISSN: 0031-9155. DOI: 10.1088/1361-6560/aad43f.

Dolde, K., Naumann, P., **Dávid, C.**, Kachelrieß, M., Lomax, A. J., Weber, D. C., Saito, N., Burigo, L. N., Pfaffenberger, A., Zhang, Y., (Mar. 2019). “Comparing the Effectiveness and Efficiency of Various Gating Approaches for PBS Proton Therapy of Pancreatic Cancer Using 4D-MRI Datasets”. In: *Phys. Med. Biol.* ISSN: 0031-9155. DOI: 10.1088/1361-6560/ab1175.

Dolde, K., Zhang, Y., Chaudhri, N., **Dávid, C.**, Kachelrieß, M., Lomax, A. J., Naumann, P., Saito, N., Weber, D. C., Pfaffenberger, A., (Feb. 7, 2019). “4DMRI-Based Investigation on the Interplay Effect for Pencil Beam Scanning Proton Therapy of Pancreatic Cancer Patients”. In: *Radiation Oncology* 14.1, p. 30. ISSN: 1748-717X. DOI: 10.1186/s13014-019-1231-2.

Oral Presentations

Dávid, C., Behl, N. G., Lott, J., Nagel, A. M., Umathum, R., Bachert, P., Kachelrieß, M., Ladd, M. E., Platt, T., (Mar. 2019). “In Vivo Motion-Compensated Abdominal Sodium (^{23}Na) Imaging at Ultrahigh Field (MoCASIm)”. In: ISMRM Workshop on Ultrahigh Field Magnetic Resonance. Dubrovnik, Croatia.

Dolde, K., Zhang, Y., Chaudhri, N., **Dávid, C.**, Kachelrieß, M., Lomax, A. J., Naumann, P., Saito, N., Weber, D. C., Pfaffenberger, A., (Apr. 29, 2019). “Dependency of the Interplay Effect on the Fractionation for Proton Therapy of Pancreatic Cancer”. In: ESTRO 38. Milan, Italy.

Poster Presentations

Dávid, C., Vahle, T., Grimm, R., Bachert, P., Kachelrieß, M., (Feb. 2019a). “Free-Breathing Motion-Compensated Diffusion-Weighted (MoCo DWI) Imaging”. In: European Congress of Radiology 2019. Vienna, Austria. DOI: `10.26044/ecr2019/C-2959`.

Dávid, C., Vahle, T., Grimm, R., Bachert, P., Kachelrieß, M., (May 15, 2019b). “Motion Compensation for Free-Breathing Diffusion-Weighted Imaging (MoCo DWI)”. In: Proc. Intl. Soc. Mag. Reson. Med. (2019). Montreal, Canada.

Dávid, C., Vahle, T., Grimm, R., Kiefer, B., Bachert, P., Kachelrieß, M., (Nov. 2018). “Motion Compensation for Free-Breathing Diffusion-Weighted Imaging (MoCo DWI) in Whole Body Integrated PET-MRI”. In: 2018 IEEE Nuclear Science Symposium and Medical Imaging Conference (NSS/MIC). #1773. Syndey, Australia: IEEE. ISBN: 978-1-5386-8494-8. DOI: `10.1109/NSSMIC.2018.8824522`.

Dolde, K., **Dávid, C.**, Echner, G., Floca, R., Hentschke, C., Niebuhr, N., Ohmstedt, K., Saito, N., Alimusaj, M., Flügel, B., Pfaffenberger, A., (May 14, 2019). “4DMRI-Based Abdominal Corset Study for Radiotherapy Purposes”. In: Proc. Intl. Soc. Mag. Reson. Med. (2019). Montreal, Canada.

Dolde, K., Naumann, P., **Dávid, C.**, Kachelrieß, M., Lomax, A. J., Weber, D. C., Saito, N., Burigo, L. N., Pfaffenberger, A., Zhan, W., (June 2019). “4DMRI-Based Investigation of Different Gating Approaches for Pencil-Beam Scanning Proton Therapy of Pancreatic Cancer”. In: PTCOG58. Manchester, United Kingdom.

Schuenke, P., Floca, R. O., Goch, C. J., Nolden, M., Zaiss, M., Windschuh, J., Dang, H. N., **David, C.**, Roeloffs, V., Bachert, P., Ladd, M. E., (June 27, 2018). “Towards a Routine Clinical Application of Chemical Exchange Sensitive MRI”. In: Proc. Intl. Soc. Mag. Reson. Med. (2018). Paris, France, p. 3.

Parts of this work were published in Dávid, Vahle, Grimm, Bachert, et al. (2019a,b) and Dávid et al. (2018) before.

Awards

Roland-Ernst-Preis (5000 EUR) Kai Dolde, **Christian Dávid**, Regula Gnirs and Dr. med Patrick Naumann *Auf dem Weg zur MR-geführten Protonentherapie: Auswirkung abdomineller Bewegung auf die Dosisdeposition bei der Protonentherapie des Pankreaskarzinoms, analysiert basierend auf wiederholten 4D-MRT Datensätzen.* (german *Towards MR-guided proton therapy: Consequences of abdominal motion on dosis-distribution for proton therapy of pancreatic cancer using repeated 4D-MRI datasets.*), 19th December 2018.

ISMRM Trainee (Educational) Stipend (value 625 USD) **Christian Dávid** *Motion Compensation for Free-Breathing Diffusion-Weighted Imaging (MoCo DWI)*, 25th Februrary 2019

Thank You

Marc Kachelrieß & Peter Bachert
Thomas Vahle & Robert Grimm & Matthias Fenchel

Siemens Healthineers
Deutsches Krebsforschungszentrum (DKFZ)
Fakultät für Physik und Astronomie, Universität Heidelberg

PI ONCO Alto & Bernd & Berthold & Dominick & Elisabeth & Felix & Manuel & Matthias & Robert & Stefan & Thomas & Thomas

E025 Akriti & Andreas & Carlo & Carsten & Carsten & Carsten & Christopher & Francesco & Irem & Jan & Joscha & Julian & Juliane & Julien & Laura & Mahmut & Manuel & Markus & Michael & Nadine & Nick & Philip & Sabrina & Sedat & Sergej & Shaohua & Stefan & Tim & Yannick

DKFZ Anna & Johanna & Kai & Lindsay & Nico & Regula & Tanja & Tristan & Vanessa

SIEMENS HEALTHINEERS
Anonymous Volunteers

Roland Ernst-Stiftung
Helmholtz-Gemeinschaft
International Society for Magnetic Resonance in Medicine
Helmholtz International Graduate School for Cancer Research

Andreas & Anita & Stephan & Lea